EFFECTS OF HYDRODYNAMIC VARIABLES ON CORROSION: STUDY OF 90/10 CU-NI IN A FLOW CHANNEL WITH NATURAL SEA WATER

Robert Paul Schack

NAVAL POSTGRADUATE SCHOOL
Monterey, California

THESIS

Effects of Hydrodynamic Variables on Corrosion: Study of 90/10 Cu-Ni in a Flow Channel with Natural Sea Water

by

Robert Paul Schack

March 1978

Thesis Advisor: J. Perkins

SECURITY CLASSIFICATION OF THIS PAGE (When Data Entered)

REPORT DOCUMENTATION PAGE

READ INSTRUCTIONS BEFORE COMPLETING FORM

1. REPORT NUMBER

2. GOVT ACCESSION NO.

3. RECIPIENT'S CATALOG NUMBER

4. TITLE (and Subtitle)

Effects of Hydrodynamic Variables on Corrosion: Study of 90/10 Cu-Ni in a Flow Channel with Natural Sea Water

5. TYPE OF REPORT & PERIOD COVERED

Master Thesis; MAR 78

6. PERFORMING ORG. REPORT NUMBER

7. AUTHOR(s)

Robert Paul Schack

8. CONTRACT OR GRANT NUMBER(s)

9. PERFORMING ORGANIZATION NAME AND ADDRESS

Naval Postgraduate School
Monterey, California 93940

10. PROGRAM ELEMENT, PROJECT, TASK AREA & WORK UNIT NUMBERS

11. CONTROLLING OFFICE NAME AND ADDRESS

Naval Postgraduate School
Monterey, California 93940

12. REPORT DATE

March 1978

13. NUMBER OF PAGES

133

14. MONITORING AGENCY NAME & ADDRESS(if different from Controlling Office)

Naval Postgraduate School
Monterey, California 93940

15. SECURITY CLASS. (of this report)

Unclassified

15a. DECLASSIFICATION/DOWNGRADING SCHEDULE

16. DISTRIBUTION STATEMENT (of this Report)

Approved for public release; distribution unlimited.

17. DISTRIBUTION STATEMENT (of the abstract entered in Block 20, if different from Report)

18. SUPPLEMENTARY NOTES

19. KEY WORDS (Continue on reverse side if necessary and identify by block number)

20. ABSTRACT (Continue on reverse side if necessary and identify by block number)

The effects of hydrodynamic variables on the corrosion rate of 90/10 Cu-Ni were studied in sea water pumped from Monterey Bay. A one centimeter square flow channel was built providing a maximum flow velocity of 7.8 m/sec. The flow field was examined using hot film anemometry in an attempt to correlate variables such as turbulence intensity to corrosion rate. General concepts of turbulence that may affect corrosion are discussed

DD FORM 1 JAN 73 1473 (Page 1)

EDITION OF 1 NOV 65 IS OBSOLETE
S/N 0102-014-6601

SECURITY CLASSIFICATION OF THIS PAGE (When Data Entered)

with a view toward resolving the disparities in reported corrosion data taken under different flow situations. Possible leading edge effects due to the establishment of the mass transfer boundary layer were investigated and found to be negligible in 48 hour tests, provided care was taken to avoid crevices or mismatches in the channel wall.

Approved for public release; distribution unlimited

Effects of Hydrodynamic Variables on Corrosion: Study of 90/10 Cu-Ni in a Flow Channel with Natural Sea Water

by

Robert Paul Schack
Lieutenant, United States Navy
B.S., University of Wisconsin, 1970

Submitted in partial fulfillment of the
requirements for the degree of

MASTER OF SCIENCE IN MECHANICAL ENGINEERING

from the

NAVAL POSTGRADUATE SCHOOL
March 1978

ABSTRACT

The effects of hydrodynamic variables on the corrosion rate of 90/10 Cu-Ni were studied in sea water pumped from Monterey Bay. A one centimeter square flow channel was built providing a maximum flow velocity of 7.8 m/sec. The flow field was examined using hot film anemometry in an attempt to correlate variables such as turbulence intensity to corrosion rate. General concepts of turbulence that may affect corrosion are discussed with a view toward resolving the disparities in reported corrosion data taken under different flow situations. Possible leading edge effects due to the establishment of the mass transfer boundary layer were investigated and found to be negligible in 48 hour tests, provided care was taken to avoid crevices or mismatches in the channel wall.

TABLE OF CONTENTS

LIST OF TABLES

LIST OF FIGURES

LIST OF SYMBOLS AND ABBREVIATIONS

Ag/AgCl	silver/silver chloride reference electrode
C	oxygen concentration
CDA	Copper Development Association
CO_2	carbon dioxide
cm	centimeter
cm^2	square centimeter
cm^3	cubic centimeter
Cu-Ni	copper nickel alloy
D_{O_2}	diffusivity of oxygen
E	potential
E_{corr}	corrosion potential of single metal
e	D.C. bridge voltage
e_o	D.C. bridge voltage at zero flow
e^-	electrons
e'	rms voltage
ft	feet
ft/sec	feet per second
g	grams
g/cm^3	grams per cubic centimeter
gal	gallons
gal/min	gallons per minute
hr	hour
H_2O	water
I	current
I_{corr}	corrosion current

i_{corr}	corrosion current density
in	inch
in^2	square inch
km	kilometers
ksi	thousands of pounds force per square inch
l	liters
l/min	liters per minute
L	characteristic length
m	meter
$\bar{M}$	composition averaged atomic weight
m/sec	meters per second
mil	one thousandth of an inch
mho/cm	mho per centimeter
mg	milligrams
ml	milliliter
mm	millimeter
ml/cm^3	milliliters per cubic centimeter
MN/m^2	mega-newton per square meter
mpy	mils per year
mV/sec	millivolts per second
$\bar{n}$	composition-averaged change in oxidation state
NACE	National Association of Corrosion Engineers
Nu	Nusselt number
O_2	oxygen
OH^-	hydroxide ion
ppb	parts per billion
ppm	parts per million

ppt	parts per thousand
Pr	Prandtl number
p'_w	wall pressure fluctuation
PVC	polyvinyl chloride
r	differentiated anemometer output, radius
R	corrosion rate
Re	Reynolds number
Re_d	Reynolds number based on hydraulic diameter
Re_x	Reynolds number based on distance from leading edge of a flat plate
Re_λ	Reynolds number of turbulence
rms	root mean square
R_p	polarization resistance
Sc	Schmidt number
SCE	saturated calumel electrode
SEM	scanning electron microscope
Sh	Sherwood number
t	time
u_l	fluid velocity in the axial direction
u^+	normalized velocity
u_f	friction velocity
u'_l	streamwise fluctuation in fluid velocity
$\bar{u}$	average fluid velocity
V	volts
X	times (multiplication)
X	power (magnification), distance from the leading edge
X_{Cu}	mole fraction of copper

X_{Ni}	mole fraction of nickel
y	distance from wall
y+	non-dimensionalized distance
y_2^+	spanwise non-dimensionalized distance
y_3^+	non-dimensionalized distance perpendicular to wall
β_a	anodic Tafel slope
β_b	cathodic Tafel slope
δ_h	hydrodynamic boundary layer thickness
δ_m	diffusion boundary layer thickness
ΔE	change in potential
ΔI	change in corrosion current
Δi	change in corrosion current density
ϵ	energy flux
ρ	fluid density
ν	kinematic viscosity
λ	microscale of turbulence
μA	microamps
$\mu A/cm^2$	microamps per square centimeter
μm	micrometer
τ	time constant
τ_w	wall shear stress
^oC	degrees Centigrade

I. INTRODUCTION

The oceans of the world are an aggressive environment, both towards man and the equipment he operates within them. Prediction of the deleterious effect of sea water on metals is but one facet of man's attempt to adapt to that environment. The practice of over-designing must end; we must design to legitimate specifications, not over-design to mask areas of ignorance. Corrosion is one area where much information is yet needed. Determining corrosion rates is a complex problem indeed. They are the product of a myriad of parameters, some controllable by man and some not; the velocity of the sea water past the metal surface is one parameter that may be either.

The effect of increased velocity on the corrosion rate of metals has been studied for over 25 years [1]. In all that time the most serious shortcoming of such studies, whether with rotating specimens, revolving electrodes or flowing electrolyte systems has been their inability to be correlated, and the inability to apply data from experiments to service situations. Table 1 and Figure 1 show the results of work by several investigators to determine the relationship between velocity and corrosion rate. While the trend is obvious, so too is the disparity between reported values.

Some of the scatter may be due to the use of small samples where non-uniform corrosion (crevice corrosion, leading edge attack or pitting) could yield skewed results.

TABLE 1

Symbol	Type of Test	Velocity (m/sec)	Test Duration (days)	Average Corrosion Rate (mpy)	Reference
l	Rotating Disk	4.0	60	7.5	Lee [2]
		8.2	60	18.0	Lee
n	Tube Flow	6.1	120	9.0	Niederberger [3]
s	Rotating Disk	4.6	55	3.2-4.0	Stewart and LaQue [4]
		9.1	55	9.1-15.3	Stewart and LaQue
d	Rotating Rectangular Bars	7.6	60	11.6	Danek [5]
a	Parallel Flow	2.1	60	0.2	Anderson and Efird [6]
f	Rotating Disk	8.2	60	14.0	Ferrara and Gudas [7]
g	Rotating Spindle	7.6	60	6.0	Ferrara and Gudas

Corrosion rates reported for 90/10 Cu-Ni in flowing sea water.

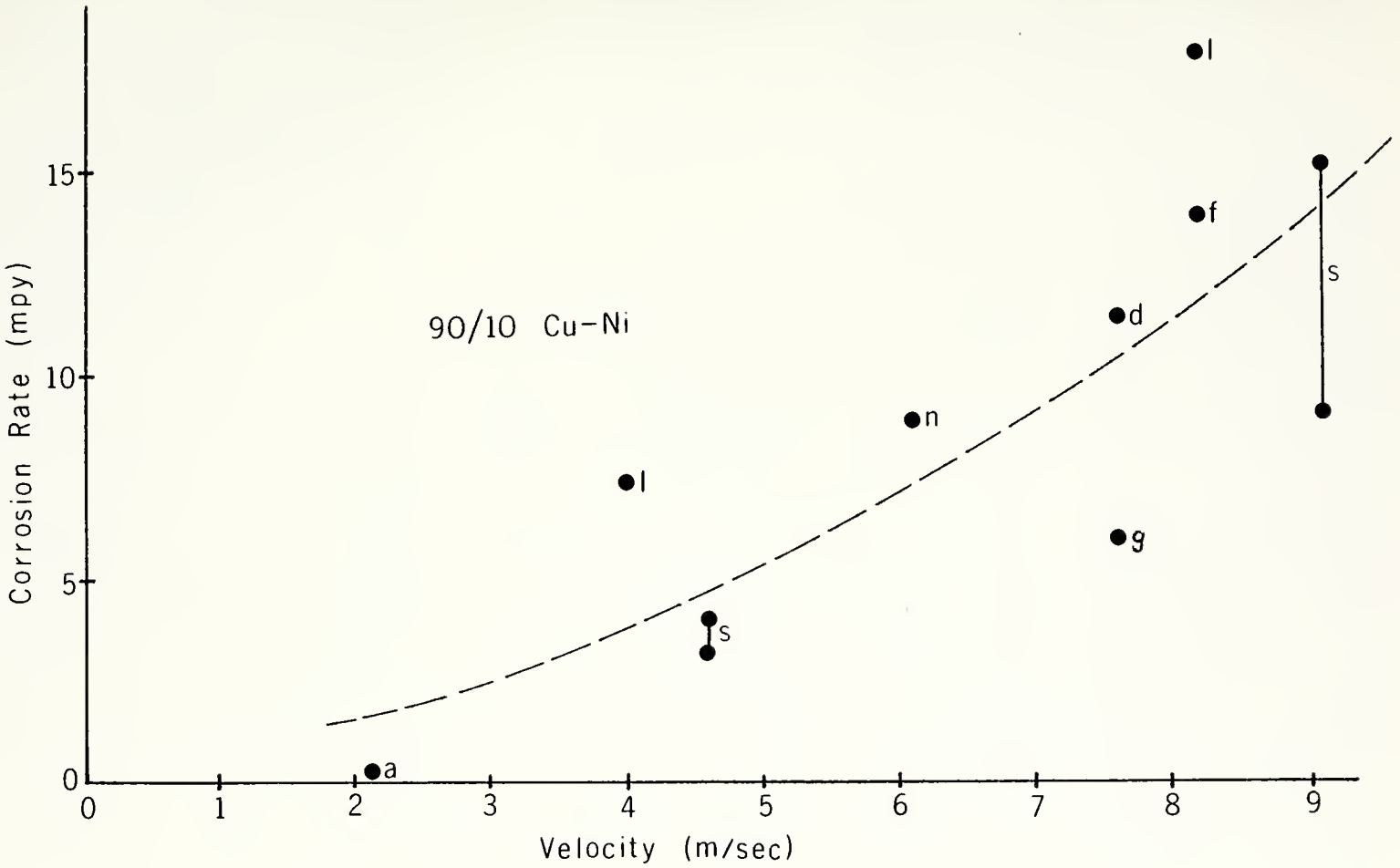

Figure 1. Variation of corrosion rate with sea water velocity as found by several investigators.

But the problem of correlating corrosion rates in different flow situations involves other factors, particularly those associated with characterization of the flow itself, and in some cases these (flow) effects may dominate the corrosion behavior, rather than other factors associated with the environment.

The character of flow near the metal surface is of prime importance because it represents the major difference between various test setups or service situations; for example, the difference between flow past a small water wheel sample and that past a high speed hydrofoil craft [8]. Historically, the corrosion rate (R) has been plotted simply against average fluid velocity ($\bar{u}$). Porte, for example, related the two by the equation:

$$R = k_1 C^{5/4} + k_2 C \bar{u}^n$$

where C is the oxygen concentration, k_1 and k_2 experimentally determined constants, and the exponent n, in the range 1/3 to 1, depending on the type of flow and surface geometry. The first term is the natural convection contribution which is insignificant at high velocities [9].

To date, attempts at relating flow characterization to corrosion with non-dimensional groupings of parameters have stopped with the Reynolds number

$$Re = \frac{\bar{u}L}{\nu}$$

where $\bar{u}$ is the average velocity, L is some characteristic dimension (distance in the line of flow for a flat plate and inside diameter for tube flow) and ν is the kinematic viscosity. Conjecture on the use of other groups, both dimensional and non-dimensional, have included wall shear stress τ_w [10], Nusselt number Nu and Schmidt number Sc [11]. None have been used to correlate flow patterns with corrosion rate, and none have been tested for varying flow situations.

In fact, turbulence is not characterized solely by the use of the Reynolds number. Reference to Figure 2 will quickly and vividly point out the possible differences in structure that can readily be imagined to have a varied effect on corrosion including corrosion produce buildup and film removal. Both pictures were obtained by Prandtl in an open channel with aluminum powder sprinkled on the water surface [12]. In both pictures the fluid velocity is the same; the only difference is the speed of the camera moving downstream parallel to the flow. Figure 2(a) was taken with the camera moving at a slow velocity. The aluminum particles near the wall appear as points. In Figure 2(b), the velocity of the camera is about equal to that of the mid-channel flow, making the wall turbulence appear "streaky." The term "streaky" also applies to the surfaces of the corroded specimens from the present experiment.

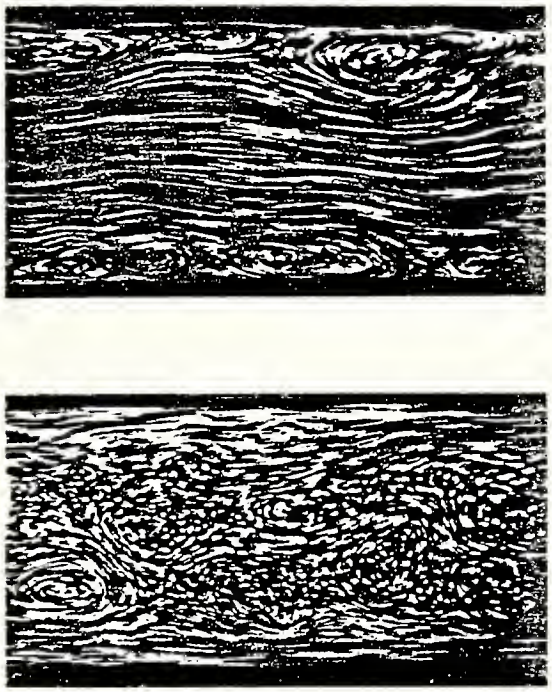

Figure 2. Visualization of turbulent flow in an open channel. (a) Camera speed slow. (b) Camera speed approximately that of the centerline fluid. From Prandtl [12].

The implication is that pure dissolution by diffusion is being supplemented by convective transport of reaction components toward and away from the metal surface.

The purpose of the present investigation was two-fold. First, it was a goal to construct a corrosion test facility with features that would fulfill the requirements for "smooth" hydrodynamics, electrochemical monitoring and visual observation of the flow. Second, it was intended to experimentally characterize the flow and pursue possible correlations with corrosion rate.

II. DESIGN OF CORROSION APPARATUS

A. SYSTEM CAPABILITIES

A photograph of the corrosion test facility used in this study is shown in Figure 3, with a schematic shown in Figure 4. Sea water was pumped from Monterey Bay into a 19,000 liter (5000 gallon) redwood tank. From there, it was drawn off as needed to fill a 204 liter (54 gallon) reservoir drum made from 15 inch PVC pipe. The system was designed for use with either natural or artificial sea water, with various possibilities for pumping and/or gravity flow. Specifically, capabilities were provided to:

(1) Fill the drum from the tank by gravity.

(2) Fill the drum with artificial sea water or fresh water.

(3) Recirculate through a bypass valve.

(4) Recirculate through the test cell.

(5) Flow through the test cell by gravity, directly from the tank and out the drain line.

(6) Drain the drum by gravity or pump.

The redwood tank was located 70 m away from and 5 m above the test apparatus. This tank was pumped full through a sand and gravel filter 1 m in diameter by 4 m high, buried in the high tidal zone. A Monel base, fitted with vertical tubes, excluded most sand and plankton. This tank was half emptied and refilled once or twice every 24 hours, depending on tidal times and heights and flow requirements. The water was filtered again through a fine mesh paper cartridge

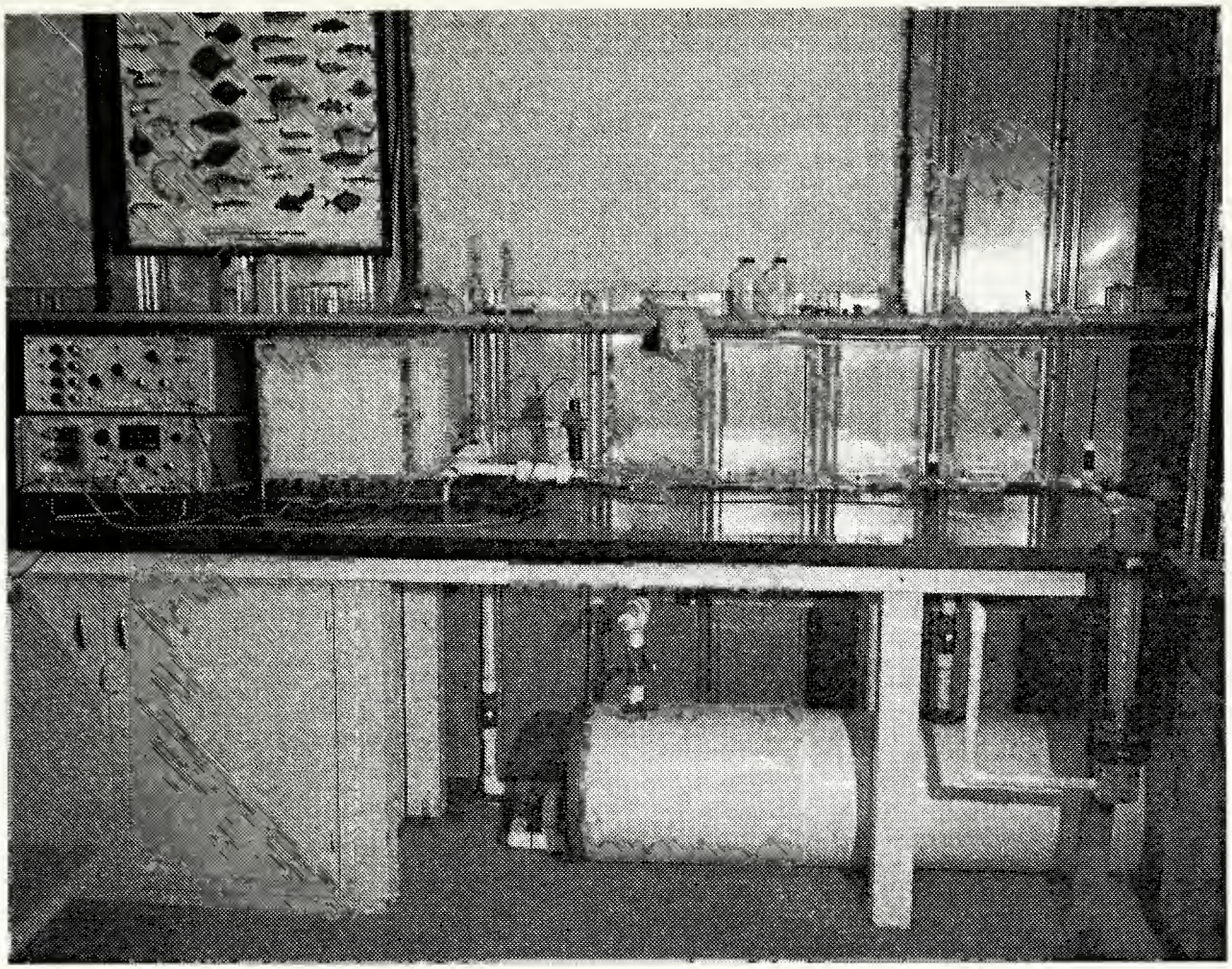

Figure 3. Portion of the corrosion test facility.

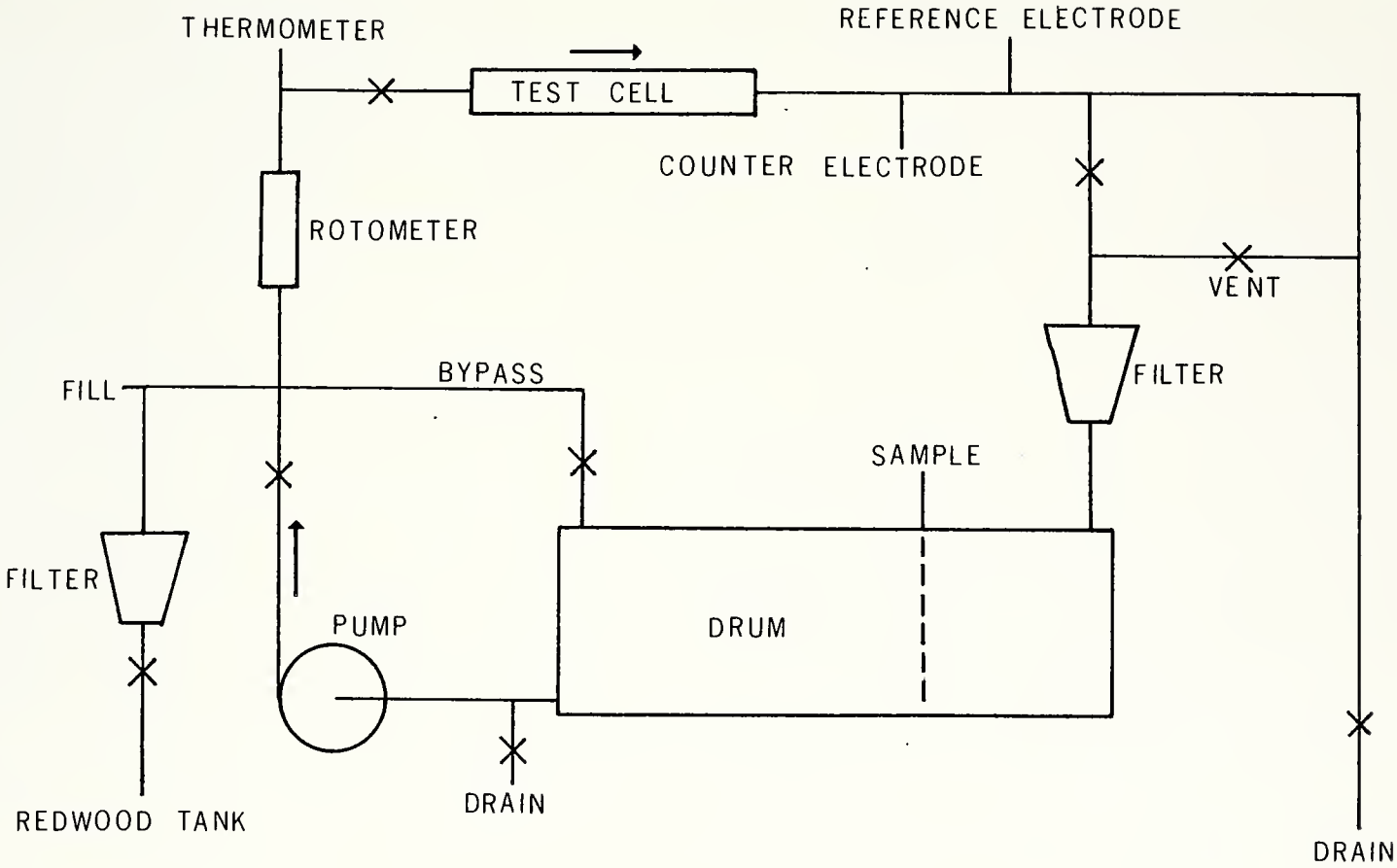

Figure 4. Schematic of the corrosion test facility.

located between the tank and the drum, and a similar filter was also included in the recirculation loop itself. This aided in preventing the accumulation of foreign matter on the anemometer probe that was used for turbulence measurements. It also removed particulates, organisms, corrosion products and other substances, such as colloidal sulphur, which might be present, and which must be removed in order that they do not alter the corrosion rate and/or mechanism.

NACE Standard TM-01-69 gives a preferred minimum volume-to-area ratio of 40 milliliters of solution per square centimeter of exposed surface. In these tests, a reservoir of 204 liters (54 gallons) was used, giving a ratio of 13,600 ml/cm^2. This larger volume:

(1) Reduced the effect of evaporation or leakage on solution properties.

(2) Reduced the effect of buildup of corrosion products/metal ions.

(3) Allowed settling of the electrolyte to release any dispersed bubbles.

Metal in the system was kept to an absolute minimum, the only exception being the stainless steel rotometer float. On tests at 2.4 m/sec (8 ft/sec) with 90/10 Cu-Ni, Ross found that additions of up to 130 ppb of copper ions (maximum tested) had no significant effect on corrosion rate [13]. Cornet has shown that even a copper ion concentration of 7 milligram per liter (700 ppb) has no measurable effect

[14]. To even reach this level of contamination, with a corrosion rate of 6 mpy, would require a total weight loss of 1.43 grams and would take 6130 hours (255 days).

The NACE standard goes on to suggest a test duration for moderate or low corrosion rate studies determined by the expression:

$$\text{Test duration (hours)} = \frac{2000}{\text{corrosion rate (mpy)}}$$

For 90/10 Cu-Ni, with a corrosion rate of roughly 6 mpy, this gives 14 days, but to obtain a larger supply of data, 48 hours was chosen instead. This shorter duration must be kept in mind when comparing these corrosion rates with others in the literature. As Efird found with tests on 90/10 at a low velocity of 0.6 m/sec (2 ft/sec), the corrosion rate continued to drop for 14 years and had not yet stabilized. It decreased from 0.5 mpy after 1 year to 0.05 after 14 years, a ten-fold decrease [15].

B. FLOW LOOP

The flow loop shown in Figure 4 was constructed from polyvinyl chloride (PVC) pipe, fittings and valves. A centrifugal pump made of glass filled epoxy was used, with no metal parts coming in contact with the sea water. With a one horsepower motor, it provided a maximum flow rate through the test cell of 12 gpm at 19 pounds force per square inch discharge pressure. This corresponded to a maximum velocity of 7.8 m/sec (25.6 ft/sec). This flow

capability covers the range of velocities normally encountered in sea water piping systems. Condensors, for example, in both shore based power plants and ships at sea, run from 1 to 3 m/sec, a compromise between pumping power, heat transfer requirements, and biofouling costs. The maximum flow capability of the present system corresponds to a speed of 15.6 knots, making higher velocities desirable in the future.

Flow rate was controlled by the pump discharge valve, a bypass valve and a valve at the inlet to the test cell. The bypass valve permitted recirculation from the drum through the pump and back to the drum. This allowed for stabilization of temperature and oxygen content prior to the start of a test run, as well as a bypass for water discharged by the pump that did not flow through the test cell. Velocity determinations were based on a Fisher Porter rotometer with maximum flow capacity of 74.2 l/min (19.6 gal/min). Calibrations with both fresh water (specific gravity 1.000) and natural sea water (specific gravity 1.028 at 33 ppt salinity) showed an accuracy of plus or minus 0.5 percent (0.06 m/sec). Temperature of the sea water was periodically monitored with a thermometer mounted at a 90 degree bend in the piping immediately upstream from the test cell.

A stable reference electrode was required from which all potentials could be measured. Saturated calumel has been used by most researchers, but is quite fragile. The type chosen was that most common in shipboard cathodic protection

systems -- silver/silver chloride. When a mixture of silver and silver chloride interacts with sea water chloride ions, a stable reference potential is generated [16]. Unlike the SCE, the Ag/AgCl billet type electrode could be easily mounted in the piping system itself as shown in Figure 5. The electrode was screwed into a horizontal "dead leg" at a 90 degree bend in the piping. Being horizontal, the well area was well circulated but not disturbed by turbulence fluctuations or air pockets that could give false readings.

Ag/AgCl electrodes have a standard reduction potential of 0.2223 volts, referenced to hydrogen. Saturated calumel electrodes (SCE) by comparison are 0.2415. Therefore, values reported in this paper could be easily compared to others in the literature by the factor 0.0192 volts. Ag/AgCl has the additional benefit of relative insensitivity to the distance between it and the center of the sample, in this system 47.6 cm (18.75 in). These electrodes can be periodically rejuvenated with a 1.5 volt dry cell battery and saturated potassium chloride. A brownish coating of silver chloride is deposited on the silver billet, and if not rubbed off produces consistent results for several weeks, perhaps longer.

C. PORTABLE TEST CELL

The test cell itself was partly modeled after that used by the Francis LaQue Corrosion Laboratory in Wrightsville Beach, N.C. and by Ross [17]. Since construction, it has

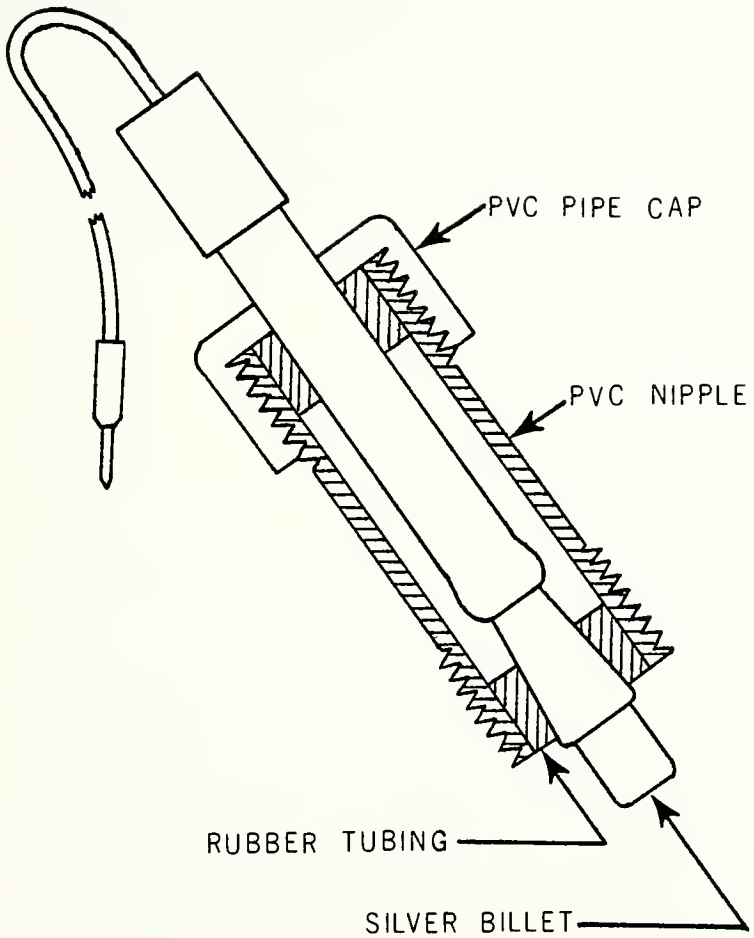

Figure 5. Ag/AgCl reference electrode with cross section of holder.

also been found that Smith used a similar setup in the late sixties [18]. The flow channel had an internal cross section 1 cm by 1 cm (0.394 in square), accurate to plus or minus 0.0002 cm. It was made of Plexiglas to prevent metallic contamination and to allow viewing of the flow during tests. Slip couplings on each end permitted easy removal. As Figures 6 and 7 show, it is of laminated construction to allow disassembly for cleaning, as well as substitution of different Plexiglas spacers to change the channel width.

An entrance length of 51 hydraulic diameters (four times the cross sectional area divided by the perimeter) was used. Hinze states that 40 should be considered a minimum to ensure a fully developed velocity profile, with less entrance length required for disturbed entry flow and high Reynolds numbers, both of which are present here [19]. Using the empirical formula for the hydrodynamic boundary layer across a flat plate, at 4 m/sec, a layer thickness of 0.5 cm, (half the channel width) is obtained at an inlet distance of 33 hydraulic diameters, so the layers from opposite walls have merged and we have fully developed flow over the specimen positions. The square test cell inlet (1.414 cm diagonal) was tapered from the round cross-section of the inlet pipe (1.58 cm diameter) to prevent skewing of the velocity profile, and an exit length of 10 hydraulic diameters was used to prevent disturbance of this profile along the

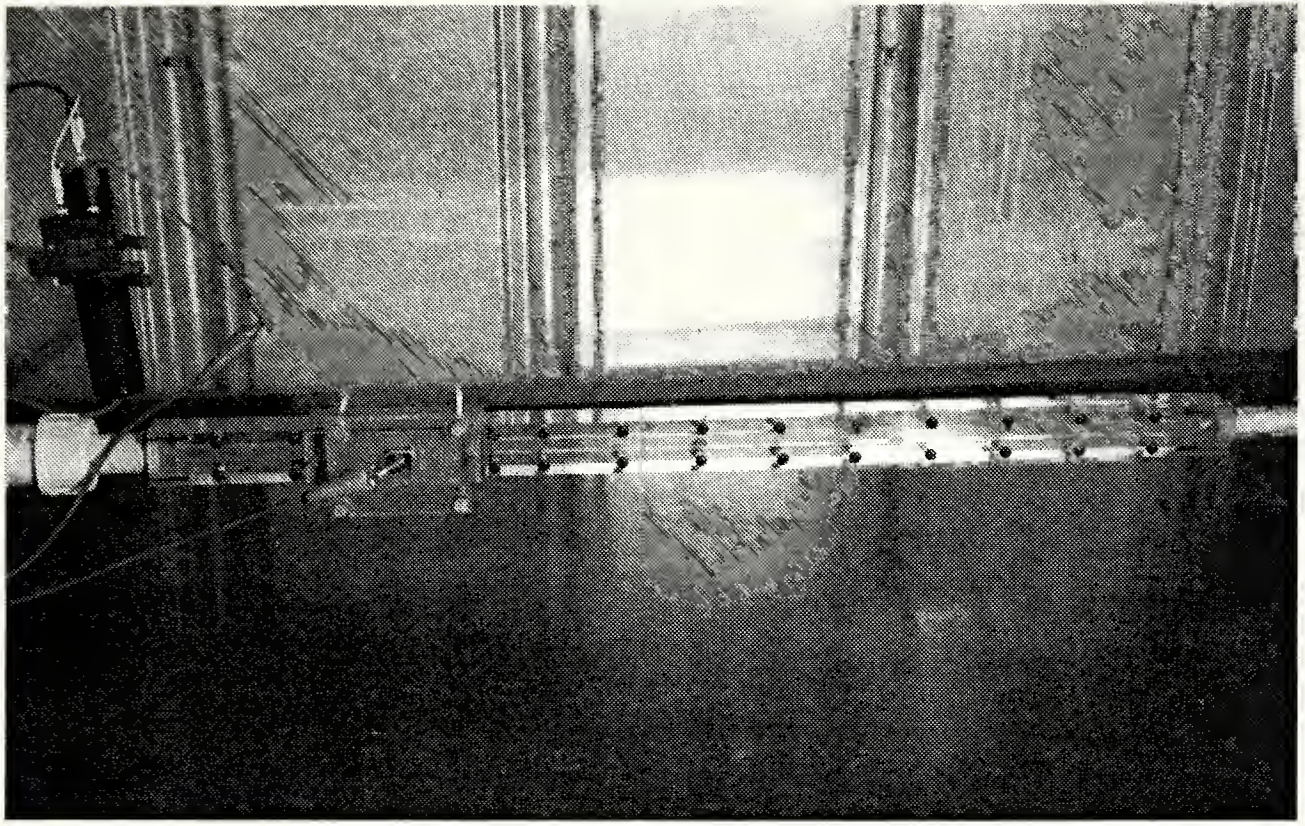

Figure 6. Plexiglas test cell.

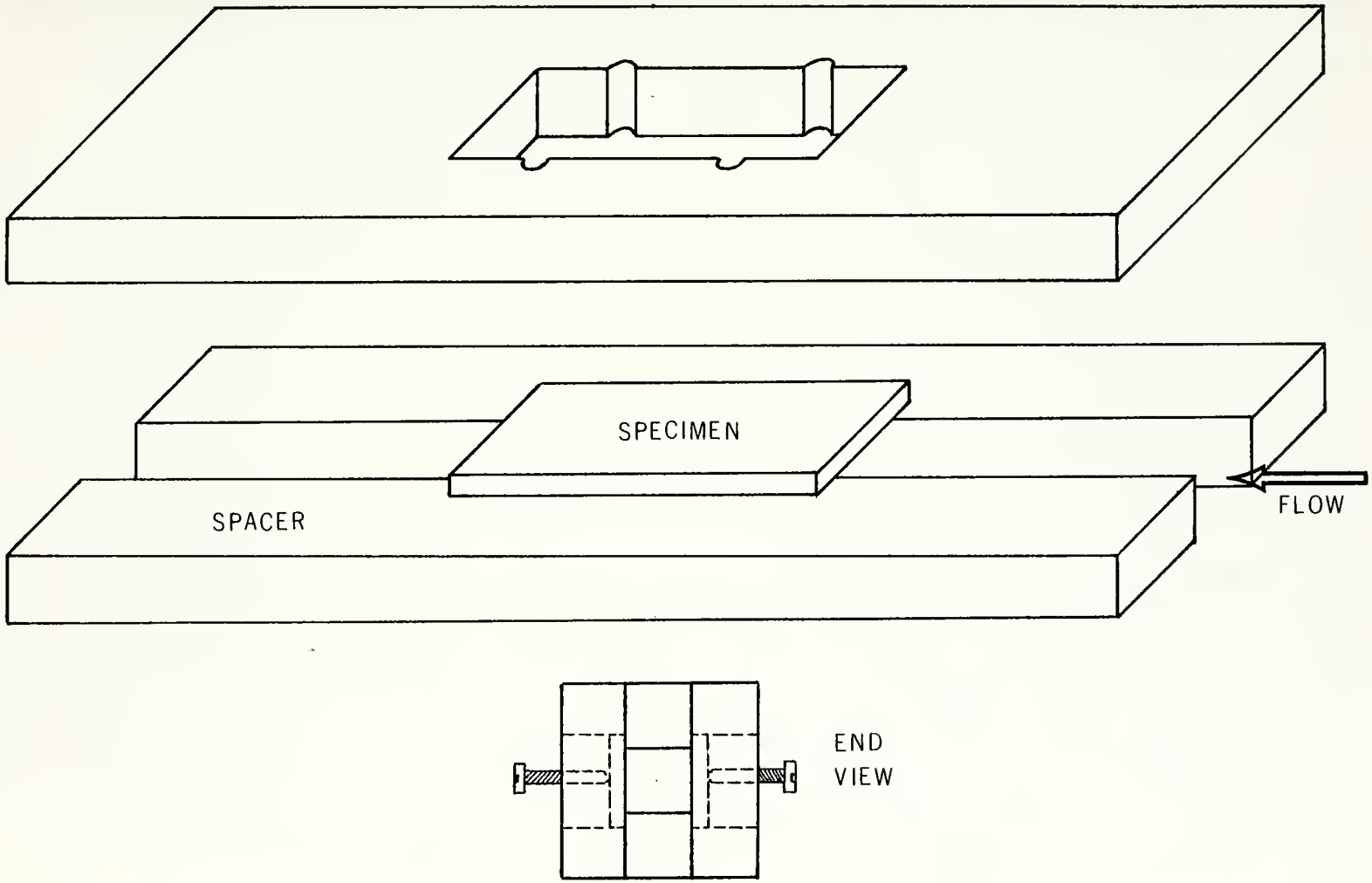

Figure 7. Layout of the Plexiglas test cell showing the laminated construction and specimen cavity.

specimens. A large discharge pipe of 2.093 cm (0.824 in) inside diameter prevented back pressure disturbances, but throttling on this side was often needed to prevent cavitation across the sample caused by the sudden pressure drop.

The samples were set into cavities on one or both sides of the flow channel, flush with the Plexiglas spacers. Sample size was 7.50 cm by 1.40 cm (2.95 by 0.55 in), and approximately 0.318 cm (0.125 in) thick. Thinner samples would bow in the channel when clamped, while excessively large ones would waste material and go beyond the range of the available analytical balance (100 grams). It is considered that a large enough exposed area was used to reduce the impact of any edge effects on weight loss. Specimens were held in place against the spacers by a series of Plexiglas backing blocks and rubber gaskets, as shown in Figure 8. Electrical connection to the specimens, when needed, was provided by brass screws tapered to a dull point and threaded into the backing blocks. Semicircular cavities along the side of one specimen cavity allowed easy removal of even a tight specimen with a special pair of pliers. The specimen on the other side could then by pushed out, ensuring no metal removal that might invalidate weight loss measurements.

Flow through the test cell was turbulent (Reynolds number based on diameter was greater than 2300). For the three velocities used in the present experiment, the corresponding Reynolds numbers were:

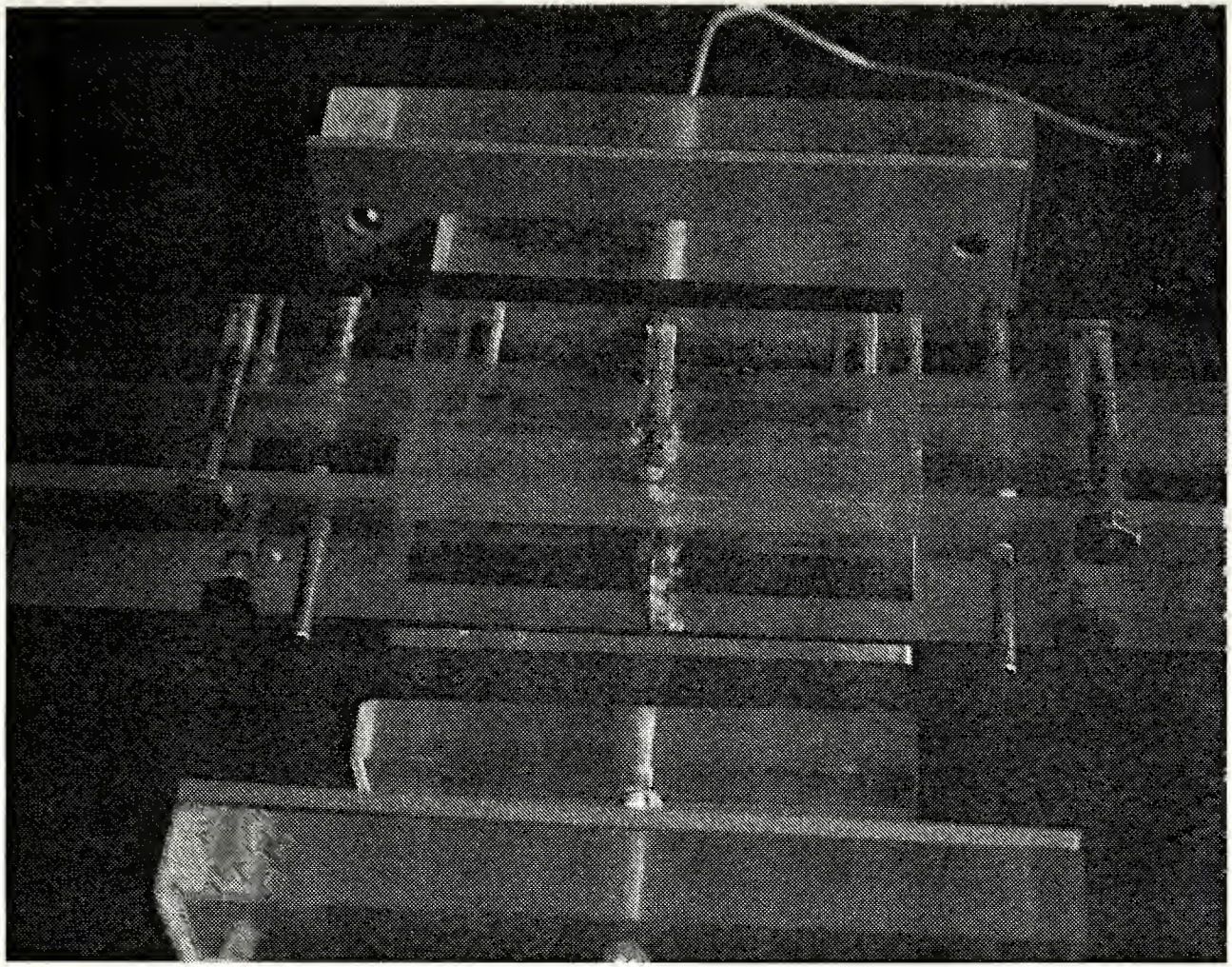

Figure 8. Arrangement for mounting specimens in test cell showing parts used for polarization plots.

Velocity (m/sec)	Velocity (ft/sec)	Re_d
2.0	6.6	1.7×10^4
4.0	13.1	3.4×10^4
6.0	25.6	6.6×10^4

In an attempt to change the character of the turbulence, i.e. eddy size, energy distribution and turbulence intensity, at a given average velocity, a variable-mesh grid network arrangement, shown in Figure 9, was placed upstream of the specimen positions in the flow. The mesh was made with 0.015 cm (0.006 in)diameter three pound test fishing line strung in a Plexiglas frame, with four different size meshes.

D. CHOICE OF ELECTROLYTE

1. Synthetic Versus Natural Sea Water

Both synthetic (artificial) and natural (fresh) have been used in corrosion studies. On the one hand, artificial sea water is reproducibly formulated [20], with pH and conductivity constant. When synthetic sea water is used, correlation of results is often simplified. Studies using synthetic sea water can be particularly effective in investigating differences between various metals or the effect of a single isolated parameter on corrosion. On the other hand, some effects that take place in a natural environment are tremendously altered or obliterated when using synthetic sea water in a laboratory situation. The use of natural sea

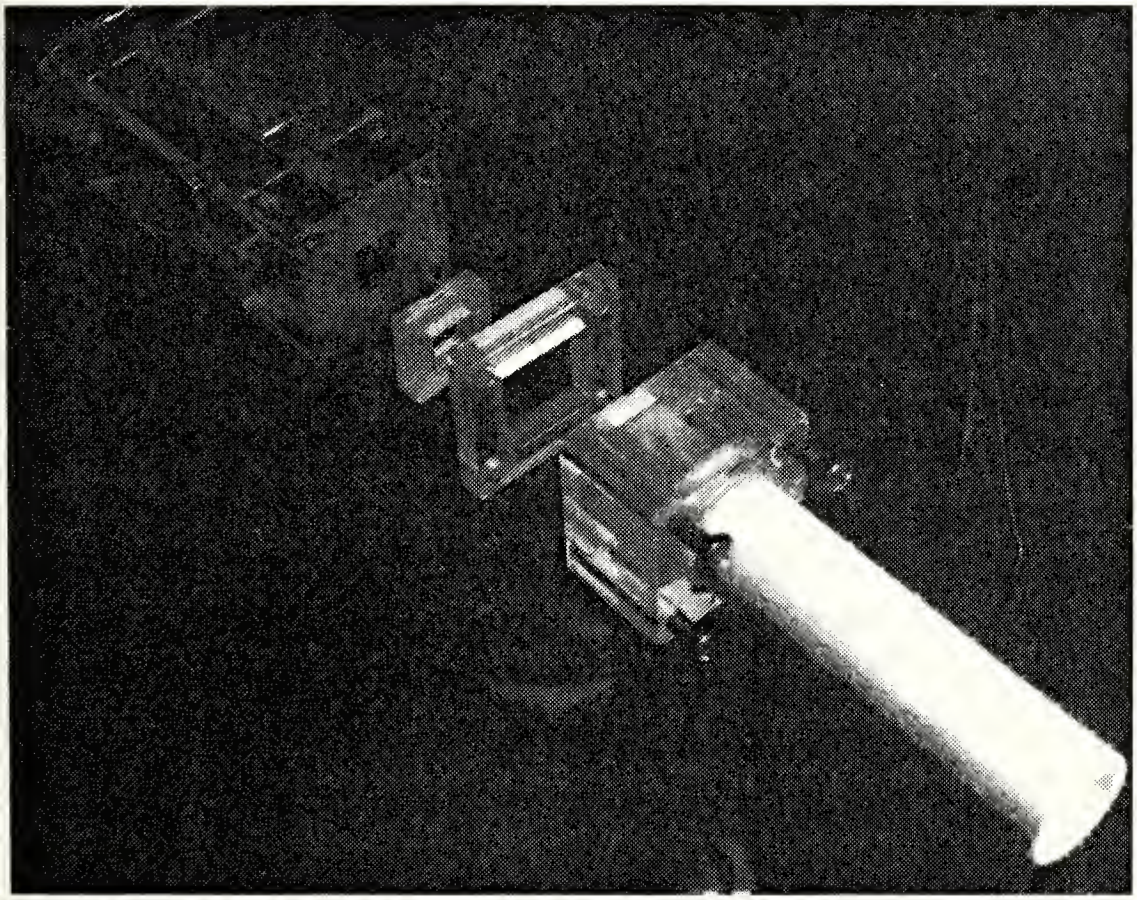

Figure 9. Arrangement of Plexiglas mesh-strung block placed in entry section of test cell.

water are often several times greater than in synthetic sea water. Admittedly, natural sea water is an extremely complex mixture. While it varies in content and properties around the world, well circulated supplies that are well aerated and free of pollution can be expected to produce similar results in different locations.

2. Supply of Natural Sea Water

a. Description of Monterey Bay, California

As shown in Figure 10, Monterey Bay is an open embayment located on the central California coast. Rich in flora and fauna, the mouth of the bay is 37 km (20 nautical miles) wide. Bisecting the bay almost symmetrically is the Monterey Submarine Canyon, one of the world's largest. Its head comes within 0.3 km (0.16 miles) of the shoreline, with depths of 200 m (656 ft) only one mile from shore, and increases in depth seaward to 865 m (2840 ft), over half a mile.

Good circulation of the bay is assured by the current system. The California Current flows slowly southward, transporting low temperature, low salinity, highly oxygenated, nutrient rich Subarctic water. The California Countercurrent flows nearer the surface, proceeding northward, transporting warm, high salinity, oxygen poor, nutrient rich Equatorial Pacific water [21].

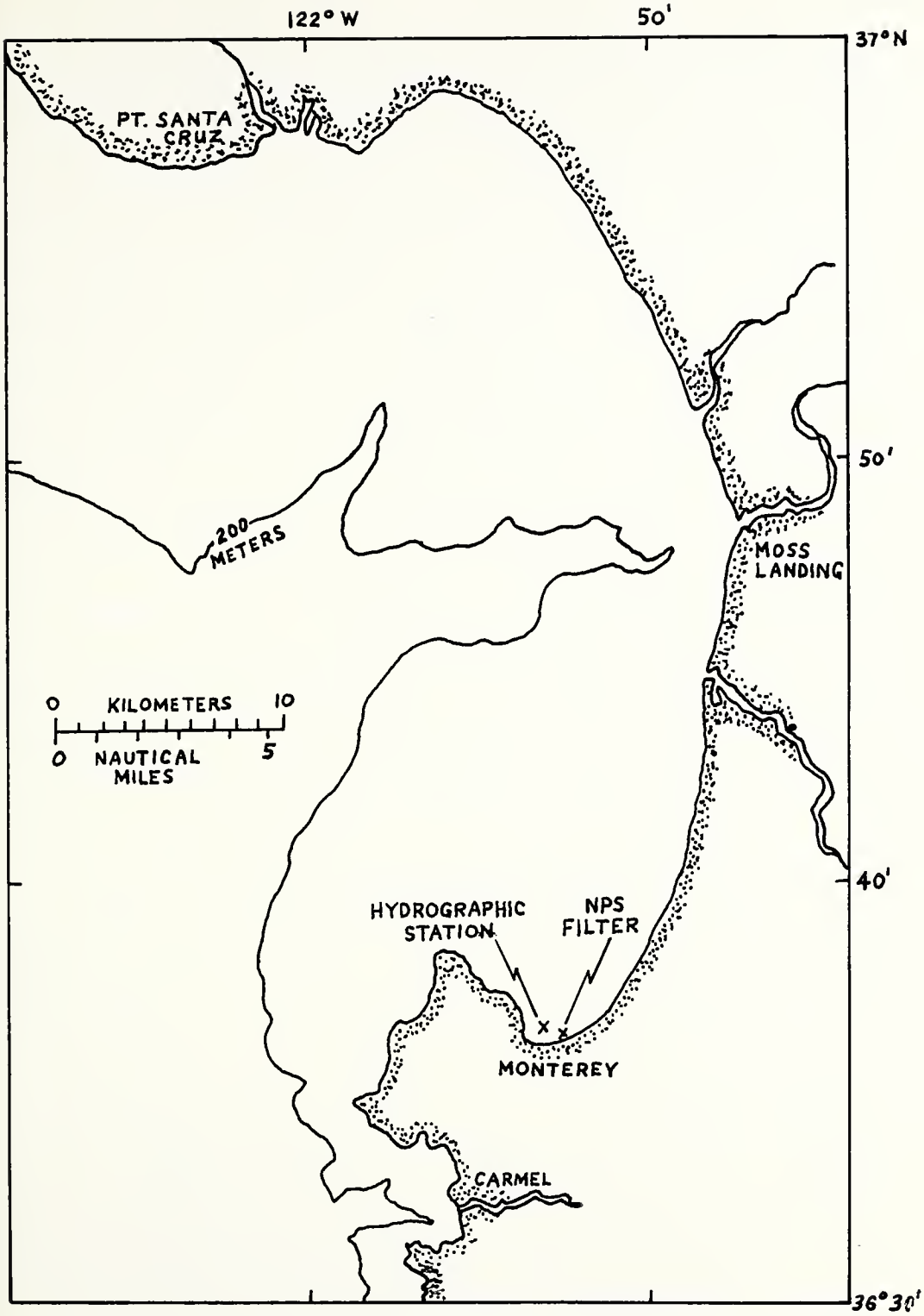

Figure 10. Map of Monterey Bay showing location of sea water supply to corrosion test facility.

From February to September, strong winds push the surface water offshore, allowing subsurface water to replace it; this is a process known as upwelling. This makes coastal water low in temperature and oxygen content and high in salinity and nutrient content. During the oceanic period, from September to November, the dense, previously upwelled water sinks, and offshore surface water flows on shore. Surface temperatures reach an annual maximum, salinity levels off, and nutrient concentrations rise. To complete the cycle, during the Davidson Current period, a local surfacing of the California Countercurrent, from November to February, water from the south converges against the coast and sinks. Surface temperature decreases abruptly, but subsurface temperature increases. Salinity is low due to surface runoff and rain (in a normal season).

General circulation within the bay appears to be that of onshore movement in the central region and counter-clockwise and clockwise flow in the northern and southern areas respectively. The residence time of water between the central bay and the northern and southern ends varies from 3 to 8 days, depending on time of year. The coastline is moderately polluted, subject to agricutural as well as industrial runoff, but with good circulation [22].

Sea water for this experiment was obtained through a sand and gravel filter buried in the high tidal zone at a location 36° 36.5' north latitude and 121° 53.0' west

longitude. The nearest extensive hydrographic data [23] is available from a sampling site approximately 0.1 miles away, where the water depth is 16 m (52 ft). For the period from January 1972 to April 1973, Figure 11 shows the variation in surface temperature. Figure 12 shows the salinity, which was computed from the conductivity [24]. Figure 13 shows the observed dissolved oxygen concentration (measured by the Winkler method of titration). All three figures are for samples taken from the surface of the bay. The limited variation of all three variables is significant. In particular, an annual variation in temperature of only $5^{\circ}C$ makes it possible to perform experiments year around, whereas those done in some other parts of the world might yield results strongly dependent upon, but inseparable from, the temperature change. As examples, the Francis LaQue Corrosion Laboratory has reported seasonal variations in temperature and salinity of $40\text{-}81^{\circ}F$ and 32-37 ppt [25], while the Ocean City Research Corporation has reported variations of $32\text{-}80^{\circ}F$ and 29-36 ppt [8].

3. Sea Water Variables

a. Marine Fouling

In terms of corrosion, the differences between artificial and natural sea water may become more pronounced if marine organisms influence results. During low velocity tests, some metals are prone to fouling by marine life, including slime film, barnacle cyprids (which cannot attach

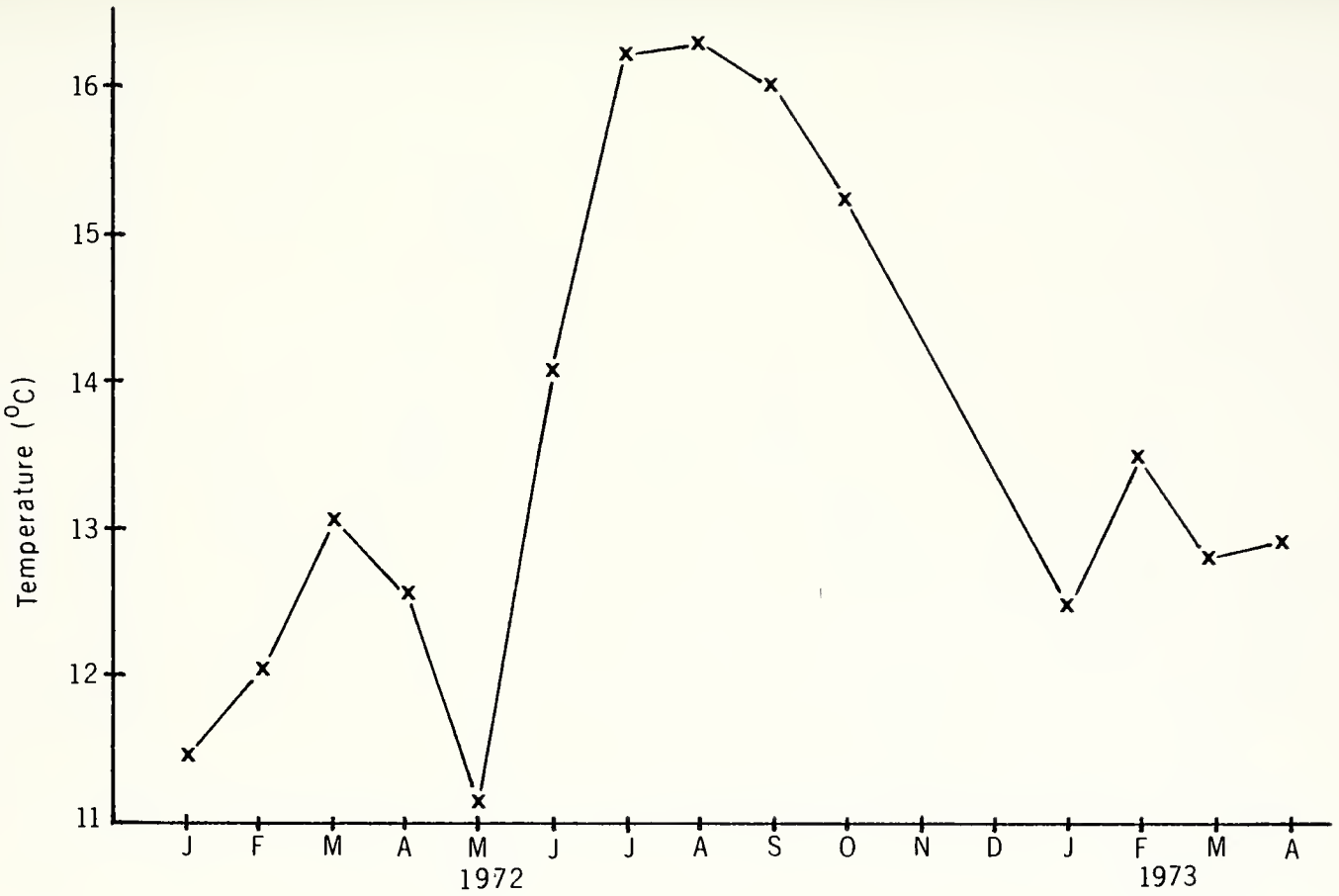

Figure 11. Variation in surface water temperature in Monterey Bay (36° 36.6' north latitude, 121° 53.1' west longitude). Data from Broenkow [23].

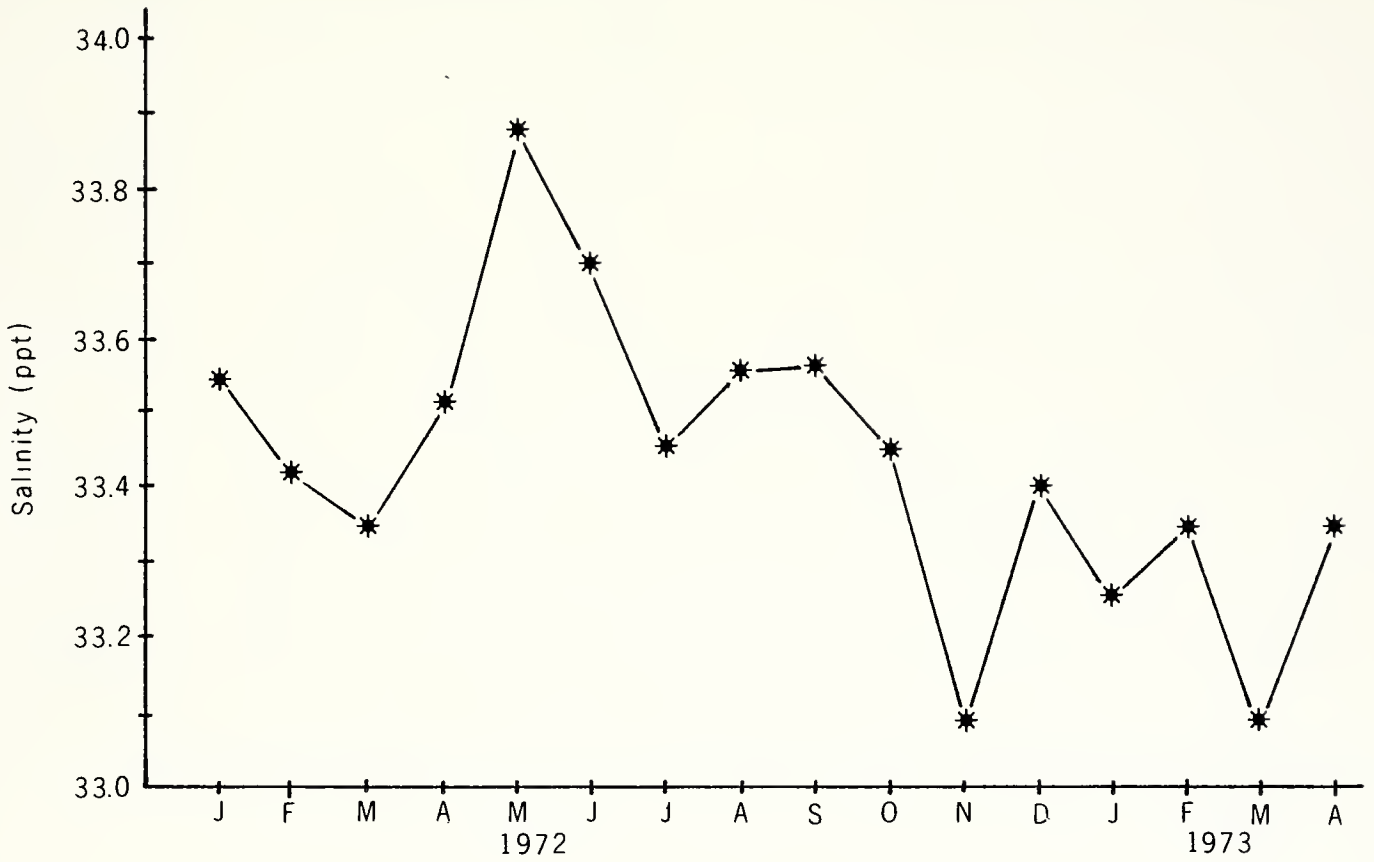

Figure 12. Variation in salinity of the surface water in Monterey Bay (36° 36.6' north latitude, 121° 53.1' west longitude). Data from Broenkow [23].

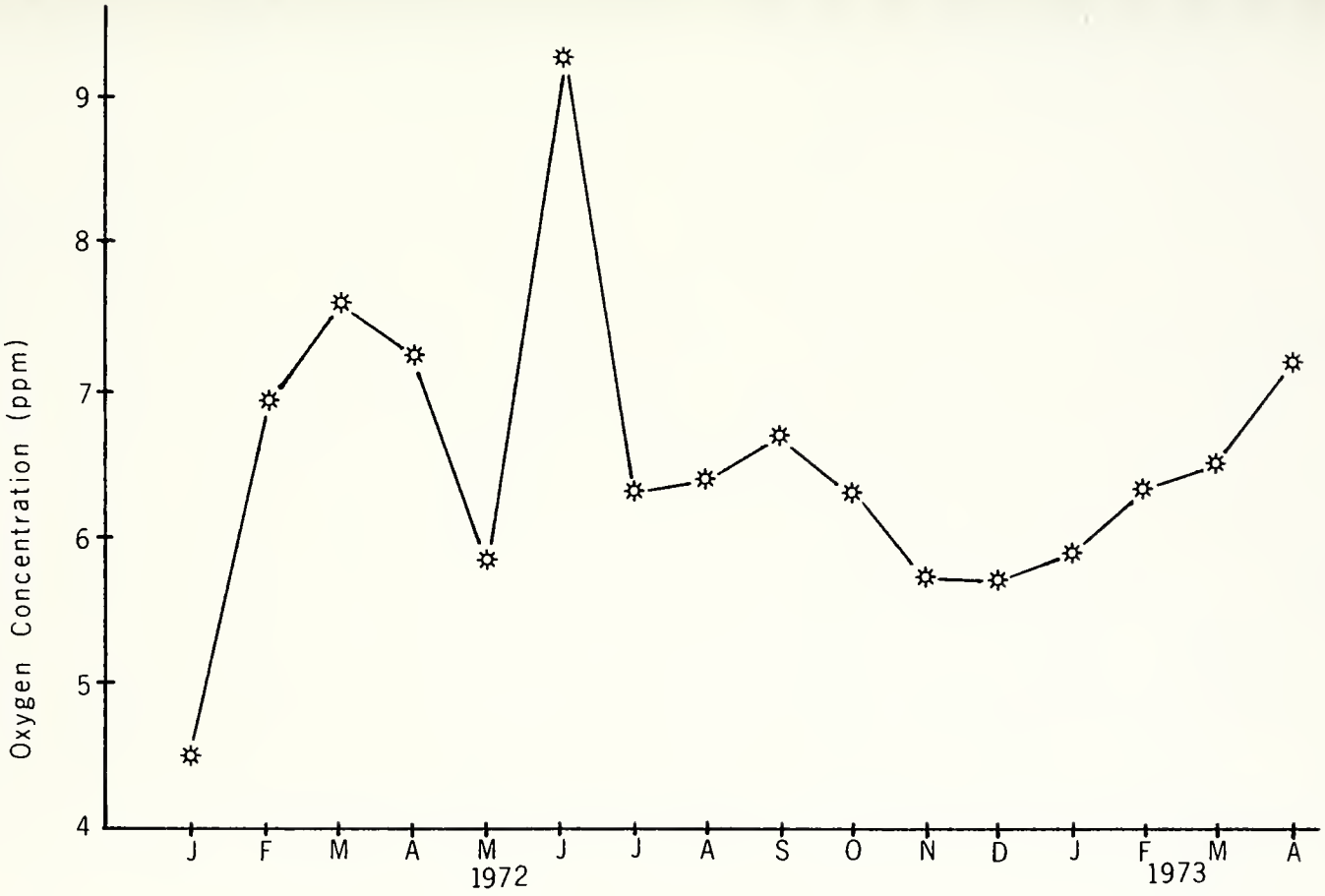

Figure 13. Variation of the dissolved oxygen concentration of the surface water in Monterey Bay (36° 36.6' north latitude, 121° 53.1' west longitude). Data from Broenkow [23].

at velocities greater than 0.5 knots) and tubeworms to name the most prevelant [26]. In stagnant or polluted water, aerobic forms can lower the oxygen content, allowing sulfate reducing bacteria to take control, producing hydrogen sulfide gas and dark colored water [18]. A 1969 National Bureau of Standards Report on "Microbial Corrosion" cites an increase in corrosion rate after one month of six times that before inoculation with a particular strain [27]. Rapid reproduction of certain species of bacteria has been reported by Bott, where a single slime cell 3 μm in diameter increased by an order of magnitude in size in only 4 hours.

Increasing the fluid velocity makes slime attachment more difficult. The slime layer becomes thinner, denser and more tightly adhered to the surface [28]. Figures 14 and 15 show the decrease in fouling rate (increase in fouling resistance) with increased velocity for both 90/10 Cu-Ni and titanium; the Cu-Ni was more resistant to fouling due to its toxicity [29]. Below 1.8 m/sec, the fouling of 90/10 was very sporadic, periodically sluffing off, while at higher velocities it fouled at a fairly steady rate.

Long term tests may similarly be influenced by this fouling. Photographs of 90/10 Cu-Ni by Efird after 14 years showed only light fouling, while other "non-toxic" metals may become encrusted with several pounds per square foot in only one year [15]. Fouling is much more variable from place to place in the oceans than is corrosion.

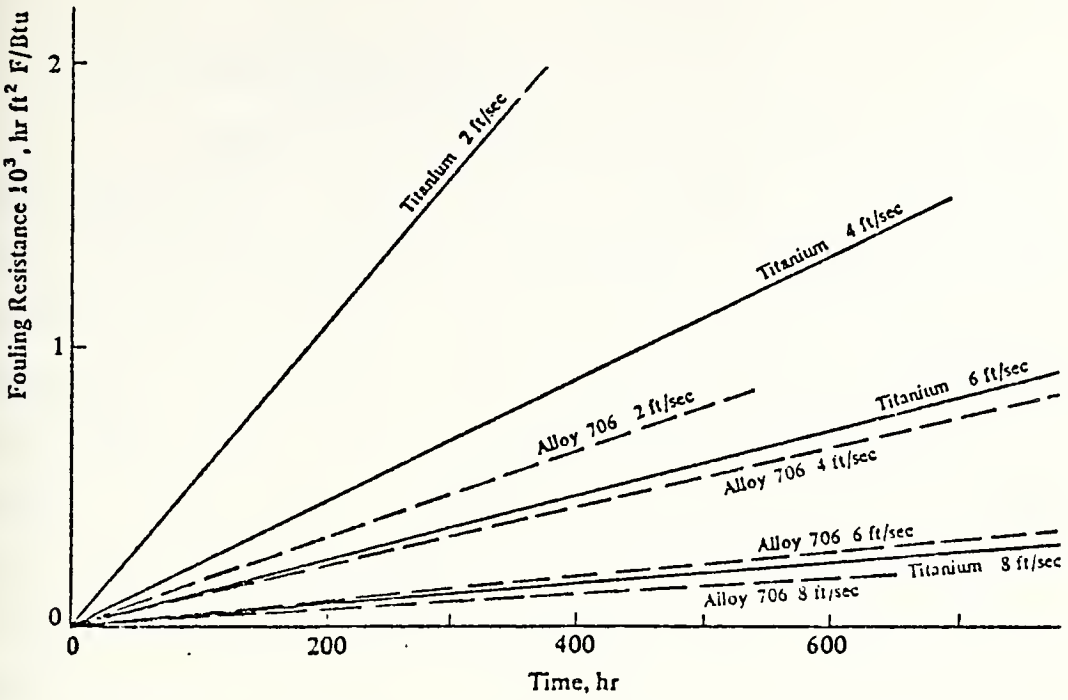

Figure 14. Fouling rates for titanium and 90/10 Cu-Ni (CDA 706). From Ritter [29].

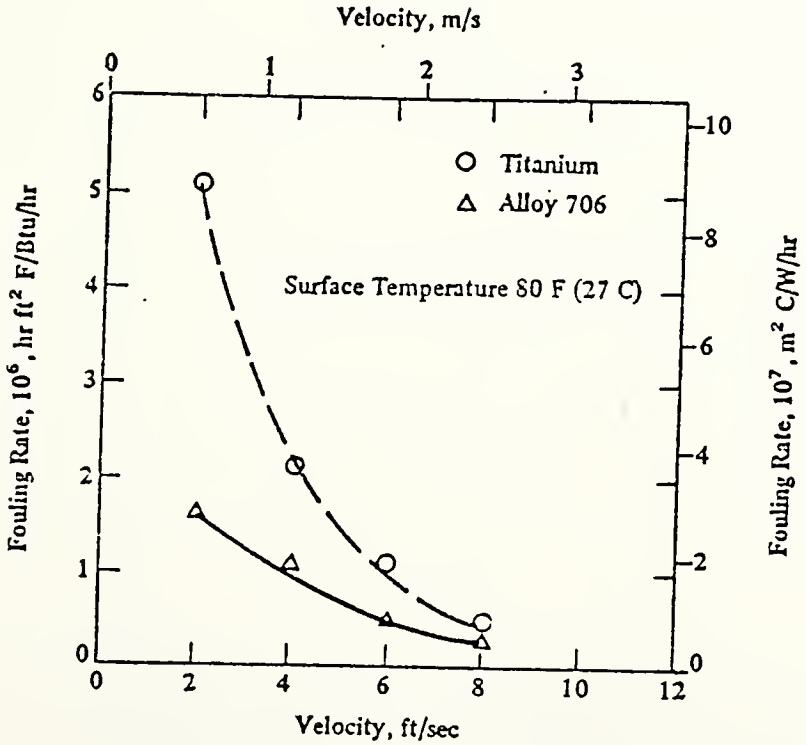

Figure 15. Effect of velocity on fouling rate. From Ritter [29].

b. Dissolved Oxygen

Oxygen is known to be a major controlling variable in corrosion. As it was not controlled in this experiment, its variability must be discussed. Two sources supply oxygen to the sea water. First is the sea/air interface, affected by wind, waves, tide and time of the year (upwelling, for example), where water becomes saturated to varying degrees. Generally, cold water has higher oxygen concentrations than warm water because oxygen saturation values at a given atmospheric partial pressure depend inversely on temperature and salinity, with salinity being the dominant factor [22]. As an example of the variation possible, Scott found surface values of dissolved oxygen within the bay itself during the upwelling period to vary from 6.3 to 8.6 ppt from one location to another (approximately 7.0 nearest our source of water) [30].

A second supply of oxygen is biochemical. During photosynthesis, phytoplankton remove nutrients from the water and release oxygen, while during decomposition nutrients are released and oxygen consumed [21]. This biological production is controlled by solar radiation, upwelling, temperature and depth of the mixed layer, and nutrient supply [22].

Horne has reported that where the concentration of nutrients is high, such as phosphates and nitrates, the oxygen content tends to be low [31]. The three great oceans

of the world tend to have characteristic dissolved oxygen profiles. The Atlantic receives an influx of new, cold, oxygen rich water from both polar regions. In contrast, the Indian Ocean and the northern boundaries of the Pacific are landlocked, their waters being older and relatively depleted in oxygen. There the circulation is poorer and more organic material has been oxidized in them for a longer period of time.

One additional generalization about the oxygen content of the seas is its variability with depth. The surface layer is well mixed with oxygen concentration near saturation and uniform down to the thermocline. Below this layer, a subsurface maximum may occur as a result of oxygen production by photosynthesis. Below this, in situ processes such as oxidation of organic matter tend to reduce the oxygen content. Yet deeper, it again increases due to the influx of young, dense, cold, oxygen rich water that has sunk down from the polar regions [31].

This discussion serves to point out not only the variability possible between different waters of the world, but even between water in the same location during different seasons or different years.

The saturation solubility of oxygen in sea water can be calculated from the equation given by Truesdale, a cubic function of temperature and a linear function of salinity. However, even easier is the use of his reduced formula:

$$C_s' = a - bS$$

where C_s' is the oxygen solubility in ppm, S is the salinity in ppt, and a and b are found from his tables using the temperature (zero to 40°C), at 0.1° intervals [32]. The trend is for a decrease in solubility with increasing salt concentration. The dissolved oxygen content in this experiment was determined using a Hach Model OX-2P Dissolved Oxygen Test Kit. It is based on the Winkler titration method and accurate to 0.2 ppm. Values encountered ranged from 5.2 to 6.8 ppm, while the corresponding saturation levels were 7.9 and 6.6 ppm.

The effect of oxygen on corrosion rate is many-faceted. It can act to depolarize cathodic areas, oxidize metal ions in the electrolyte to a higher valence or form a protective film. Since corrosion is an electrochemical process, it can be divided into an oxidation and reduction reaction. The rate of corrosion is determined by the "slower step." For copper alloys in sea water (alkaline), the reduction reaction is:

$$O_2 + 2H_2O + 4e^- \longrightarrow 4OH^-$$

Reinhart found only a slight increase in corrosion rate as oxygen was increased from 0.4 to 5.75 ppm [33]. Recently MacDonald and Syrett [34] have extended this range up to 26.3 ppm; although this concentration is more than double the value that would be found in natural waters, the dramatic

increase in corrosion rate highlights not only the importance of oxygen itself, but also of any other variable that increases the quantity of dissolved oxygen that reaches the metal surface. MacDonald and Syrett hypothesize that the increase in corrosion rate at high oxygen content is due to a positive shift of the corrosion potential beyond a critical value, where a different reaction mechanism becomes possible, greatly enhancing film breakdown for certain copper alloys [35]. This occurs despite the microscopic observation that a thicker film is formed in the more highly oxygenated water. They found that a high oxygen levels the reaction rate is under anodic control, where the corrosion rate is determined by ionic or electronic transport through the surface film. At very low oxygen contents, cathodic control would dominate, with the corrosion rate determined by the transport of oxygen to the surface.

c. Temperature, Salinity, Conductivity, pH

Temperature also has an effect on corrosion. While in general, corrosion kinetics tend to increase with temperature, this effect is counteracted by the decreasing solubility of oxygen in water at higher temperatures. Also as temperature increases, the diffusion coefficient of oxygen increases, which tends to increase corrosion rate, but this change is tempered by the concurrent increase in the thickness of the diffusion boundary layer which acts to decrease corrosion rate. Also, an increase in temperature can increase the rate of marine fouling.

Temperatures within the laboratory itself occassionally ranged from 8 to 20°C in a 12 hour period. However, ordinarily only a 5°C variation was experienced, which led to a fluctuation of up to 3°C in the flow loop sea water temperature. The original sea water temperature was also raised by the heating effect of the pump, reaching a steady state condition of 6 to 8°C above room temperature. Recirculating the water for 6 to 8 hours prior to a test run reduced the temperature rise during a run from 10 to only 2°C. Peterson and Gehring have recently tested a new flow channel where the temperature variation was even more significant, 21.6 to 41.0°C [36].

Salinity, expressed in ppt, is the percentage of solid material present, and is roughly a measure of the total salt content. It is usually determined by measuring the electrical conductivity of the sample, and then converting with appropriate tables from Cox [24]. The specific conductance of sea water varies almost linearly with temperature and electrolyte concentration, i.e. salinity. At a salinity of 33 to 34 ppt, it is 0.035, 0.040 and 0.045 mho/cm for 10, 15 and 20°C respectively [31]. Conductivity in this experiment ranged from 0.0308 to 0.0371 mho/cm.

In natural sea water, pH is controlled primarily by the amount of dissolved CO_2 in the water [31]. Photosynthetic activity and solar radiation are controlling. For surface water, equilibrium with the atmosphere usually assures a

high pH. Normal values for sea water are 7.5 to 8.4, slightly alkaline. Interactions of CO_2, ammonia and hydrogen sulfide (formed on the death and subsequent decay of fouling organisms) can also produce local perturbations in pH. It can thus vary seasonally and daily. During this study the range was from 7.68 to 7.92, measured with a 4403 Electromark Digital Analyzer accurate to 0.01. Porte has shown that even at temperatures as high as 40°C, the corrosion rate is independent of pH for the range 5 to 8, increasing slightly for pH less than 4 and decreasing slightly for a pH above 10 [9].

III. EXPERIMENTAL PROCEDURE

A. POTENTIODYNAMIC POLARIZATION PLOTS

As a metal corrodes, it assumes a particular potential. This potential can be measured directly, but the corrosion current cannot. The corrosion current is equal to the sum total of all the current that is flowing between the local anodes and cathodes on the metal surface. It can be measured indirectly using a potentiostat, by controlling the potential of the corroding metal and measuring the cell current. The resultant curve is a polarization plot. The potentiostat can drive the potential from the least noble potential desired through the equilibrium corrosion potential E_{corr} to the most noble potential desired. The upper and lower portions of the curve correspond to the anodic and cathodic reactions respectively. The slopes of the linear portions of these two arms are the so-called Tafel slopes. The intersection point of the two Tafel lines gives the equilibrium corrosion potential (E_{corr}) and the corrosion current (I_{corr}) for that particular period in time. The plot is made at a relatively slow scan rate of 1 mV/sec, so the corrosion current found is really an average over the 15 minutes required to run the plot.

B. HOT FILM ANEMOMETRY

In order to characterize the flow situation within the test cell, measurements were made with a hot film anemometer

mounted as shown in Figure 16. The detecting element of the probe is a very fine metal film on a glass substrate 0.025 mm (0.001 in) in diameter and 0.5 mm (0.020 in) long. The film is heated by an electric current, but the flowing water tends to cool the film, lowering its electrical resistance. Therefore, the current needed to maintain the film at a constant temperature can be related to the fluid velocity (in a linear manner with proper circuitry). The film itself is coated with a thin layer of quartz to protect it from abrasion by suspended particles, and the joints and supports of the probe are insulated. Figure 17 shows an unused probe on the right and a probe used for less than one hour on the left. While the fouling was easily removed by ultrasonic cleaning, it did alter the calibration, tended to give suspicious results and led to premature failure. Provision of an additional filter, in the flow loop itself, solved the fouling problem, which had existed even when fresh tap water was used.

In this study, a miniature probe was used. The small frontal area of the probe shaft, 1.5 mm (0.06 in) minimized the increased local velocity that results when any protruberence reduces the local flow channel cross sectional area. Hinze has shown that a small sensing wire is needed for low velocities and/or small eddy measurements [19]. However, for measurements close to the wall, even this small obstacle to flow is significant. Fluid flows between it and the wall,

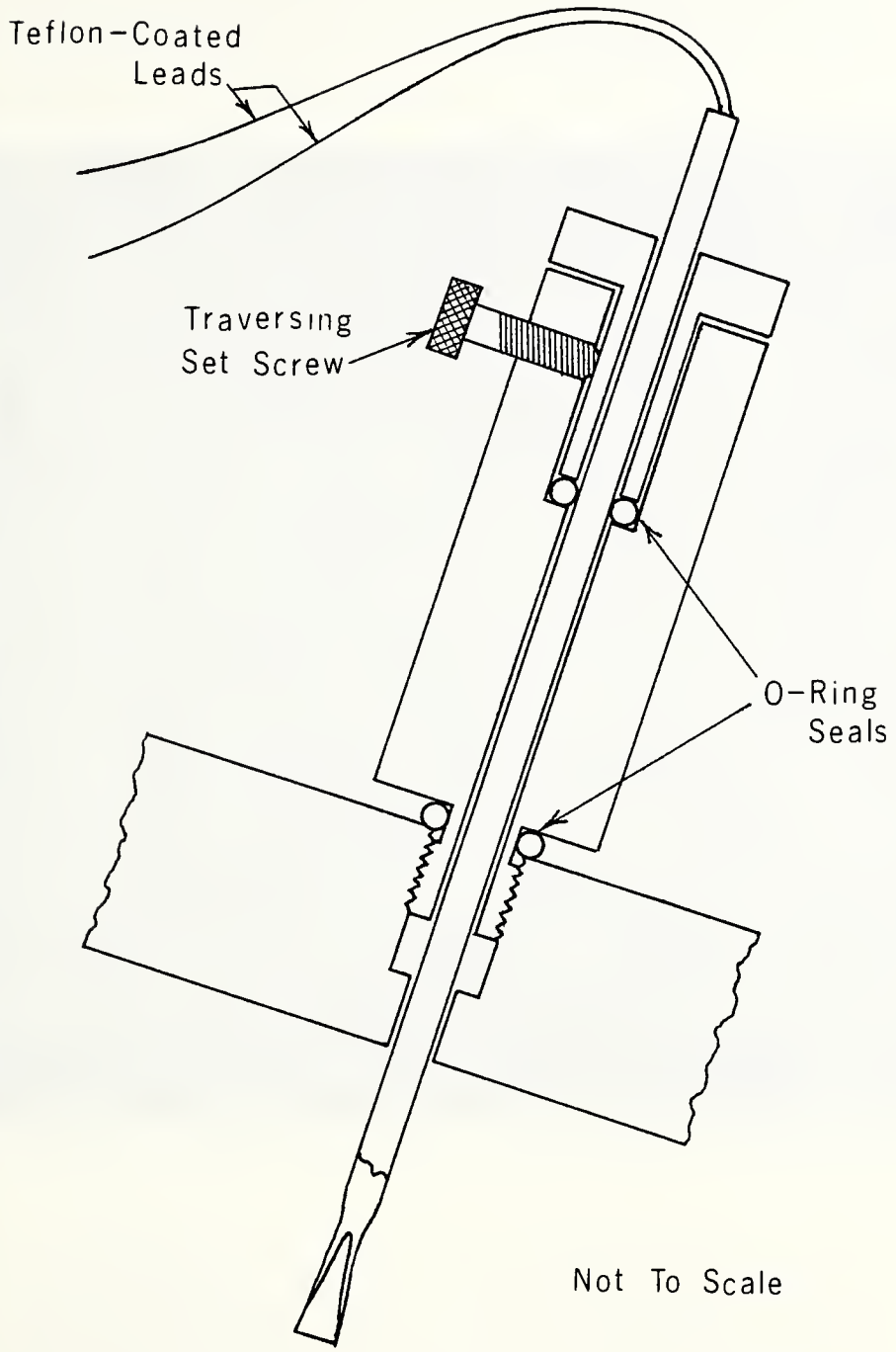

Figure 16. Plexiglas block (fits into specimen cavity) with anemometer probe and cross section of probe holder.

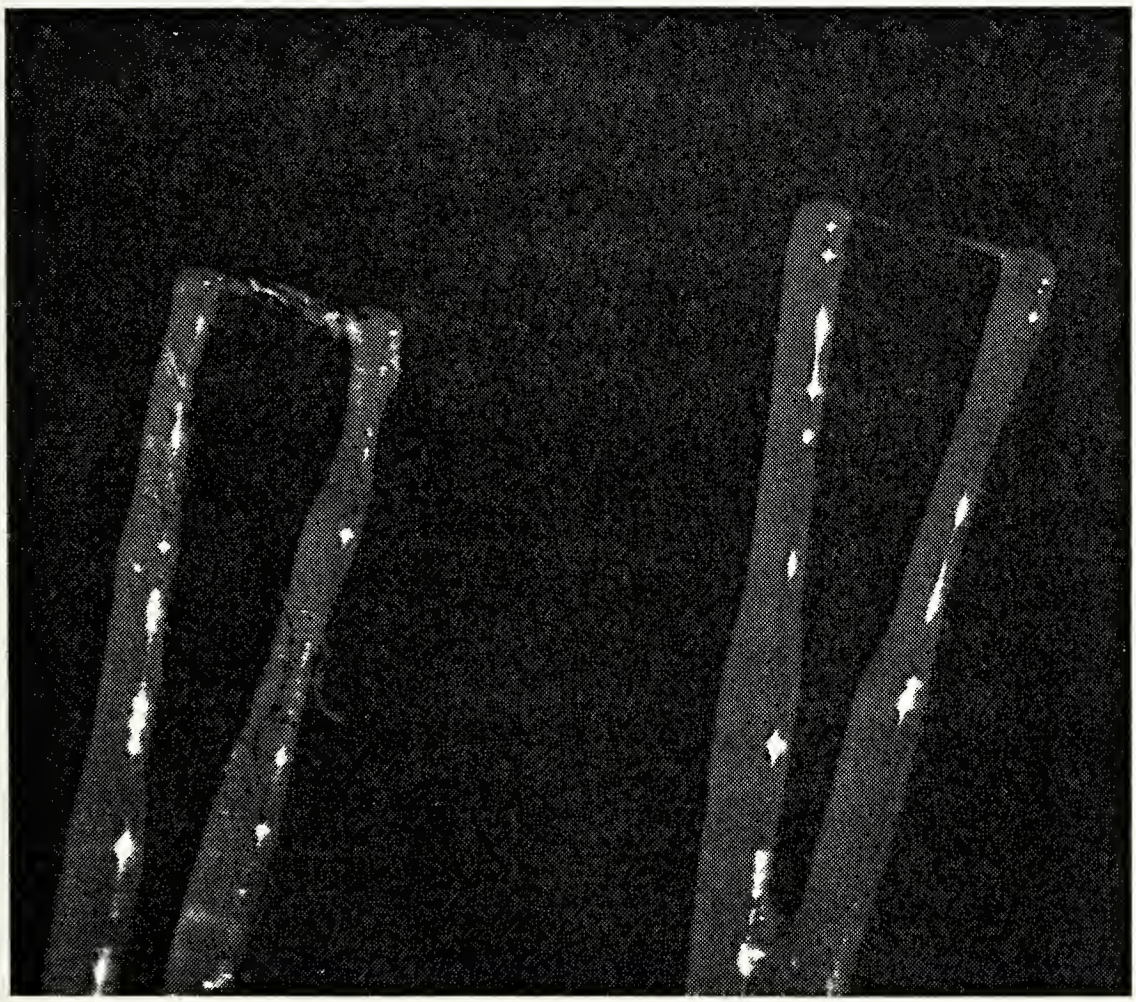

Figure 17. Cylindrical hot film probes. Probe on left used less than one hour in unfiltered fresh water. Probe on right unused (22x).

accelerating and separating. Only with an external device, such as a laser, can undisturbed measurements be made.

When flow characterization measurements were being made, a Plexiglas block was fitted into the specimen cavity on one side, making three sides of the flow channel completely smooth for their entire length. The hot film probe was mounted in the other specimen cavity through a hole in the block. It was mounted near the center to avoid any disturbances caused by the leading edge of the block or by the corners of the channel, and hopefully would give data that represented the typical flow structure over the corroding metal surface.

C. CORROSION TESTING

1. Sample Preparation and Handling

The material used as samples in this study was 90/10 copper-nickel (CDA Alloy 706) hot rolled 5/8 inch plate with soft temper. Chemical composition is given in Table 2, with the mechanical properties given in Table 3. Figure 18 shows the microstructure of a polished specimen, etched with a mixture of 1 part hydrogen peroxide (30 per cent), 19 parts distilled water, and 10 parts ammonium hydroxide (specific gravity 0.90) Figure 18(a) shows the average grain size, which varied with distance from the rolled surface. Figure 18(b) shows certain crystallographic planes within the grains. It is apparent that a great deal of distortion still exists within the metal, a condition

TABLE 2

MIL-C-15726 E Amendment 2 CDA 706

Element	Composition (per cent)
Copper	87.40
Nickel	10.40
Iron	1.50
Manganese	0.49
Zinc	0.13
Tin	0.02
Silicon	0.02
Lead	0.01
Phosphorous	0.013
Sulphur	0.001

Chemical composition of 90/10 Cu-Ni.

TABLE 3

Yield Strength	.1068 MN/m^2 (24.0 ksi)
Tensile Strength	.2358 MN/m^2 (53.0 ksi)
Elongation	40 per cent
Hardness	Rockwell B-25
Density	8.93 g/cm^3

Mechanical properties of 90/10 Cu-Ni.

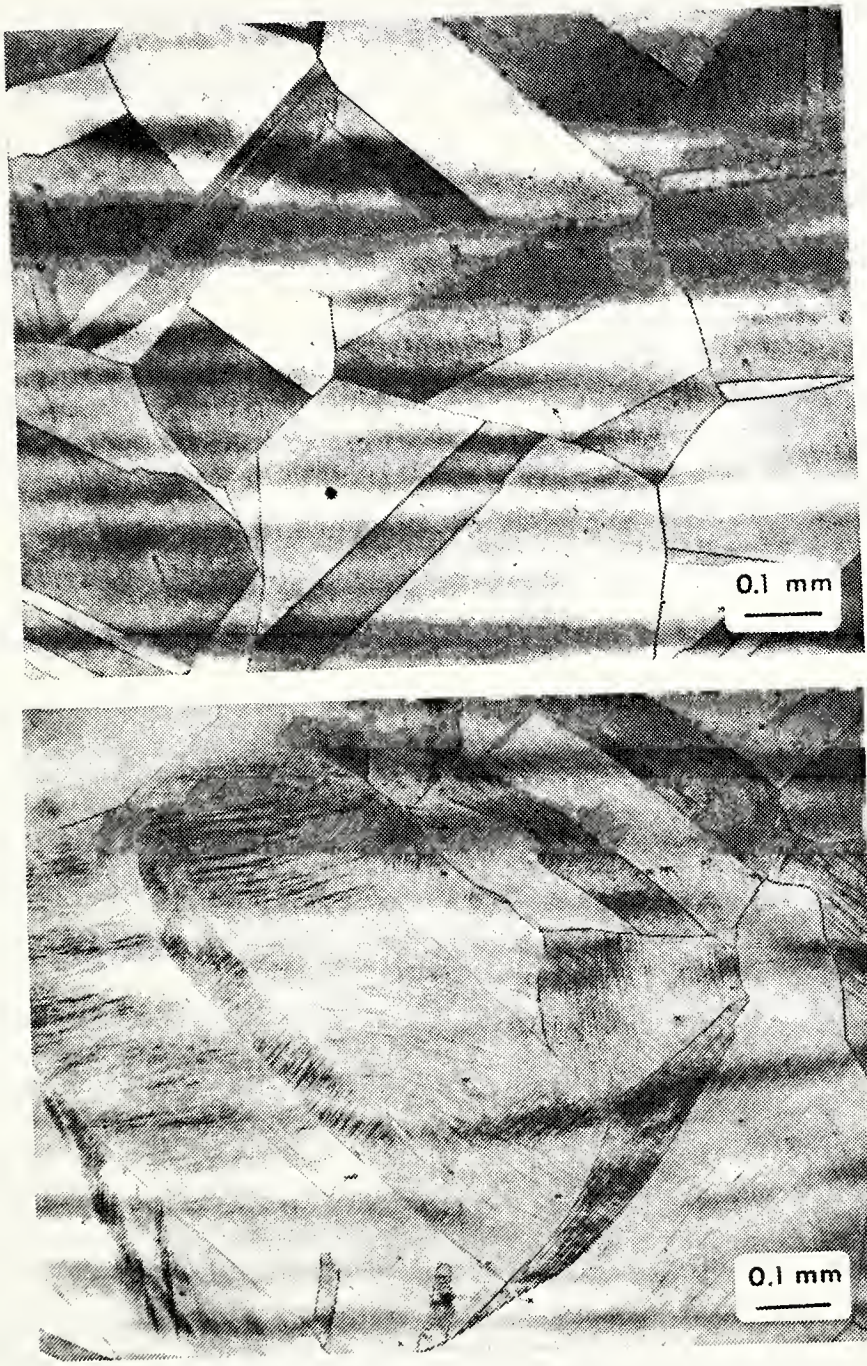

(a)

(b)

Figure 18. Microstructure of annealed 90/10 Cu-Ni, polished and etched. (a) Average grain size. (100X) (b) Crystallographic planes within grains. (100X)

that would increase the corrosion rate. The horizontal shadows in both photographs are termed structural streaks, revealed by the etchant as a result of structural heterogeneities within the plate.

Samples for polarization plots done in a beaker were 0.953 cm (0.375 in) high by 0.953 cm (0.375 in) diameter right circular cylinders with an exposed surface area of 6.467 cm^2 (1.002 in^2). A 3-48 hole 2 mm deep was used to attach the sample to the electrode holder. Samples for the flow channel were machined so a transverse face was exposed. Samples were polished with 3/0 grade emery paper. The first four sets of samples were run with polishing lines parallel to the flow to minimize erosion by accentuated turbulence, and get accurate weight loss data. Subsequent samples were run with polishing lines perpendicular to the flow, to allow differentiation between streamwise corrosion features that result from preferential dissolution of the lines (stress concentration sites, or oxygen deficiency at their bases), and those features caused by the flow itself. The samples were then wiped clean with Kim-Wipes, degreased with ethyl alcohol, and air dried. The dried samples to be used for weight loss determinations were weighed on a Sartorius-Werke A6 balance to an accuracy of 0.1 milligrams.

Generally, two samples were run simultaneously on opposite sides of the flow channel. One was used for weight loss and the other for SEM study. The SEM sample was cut

into three pieces 2.5 by 1.4 cm (0.98 by 0.55 in), any one of which would fit easily onto a large SEM stub of diameter 3.15 cm (1.24 in). Usually, only the cut section containing the leading edge was used, as it contained the general morphology present in the other sections. This also allowed observation of crevice corrosion or leading edge flow effects, if present.

After the tests, specimens for weight loss were cleaned by dipping for five minutes in a mixture of one part HCl (specific gravity 1.18), 5 parts sulfuric acid (specific gravity 1.84) and 4 parts distilled water, as recommended in the ASTM Standard G1-72(37). This was followed by light scrubbing in distilled water with a fine bristle toothbrush, rinsing in ethyl alcohol and air drying. The effect of this cleaning solution in removing metal was tested on a channel specimen and found to be negligible within the accuracy of the scale used. After exposure, the specimens were weighed to the same accuracy of plus or minus one mg. The corrosion rate was calculated from the weight loss by the formula:

$$\text{Corrosion rate} = \frac{\text{constant X weight loss}}{\text{area X time X metal density}}$$

with weight loss in grams, area in cm^2, time in hours and density in g/cm^3. To obtain the corrosion rate in mpy, the constant is 3.45×10^6, while 8.76×10^7 will yield the value in μmpy.

2. Polarization Resistance Measurements

The rate at which a metal corrodes can vary with time; often the variation is significant. Monitoring this change can give useful information concerning which corrosion mechanisms are operating and the structure of the protective film. The instantaneous corrosion rate and corrosion current can be found from the polarization resistance, i.e. the resistance of the metal surface to a change in applied potential and equals:

$$R_p = \frac{\Delta E \text{ (applied)}}{\Delta i \text{ (measured)}}$$

where Δi is the change in current per unit surface area of the specimen. The potential of the specimen (working electrode) as compared to the reference electrode is varied by passing a suitable current between the working and the counter electrode.

The corrosion current is related to R_p by the Stern-Geary formula [38]:

$$i_{corr} = \frac{\beta_a \beta_c}{2.303 R_p (\beta_a + \beta_c)}$$

The sensitivity of this formula to the Tafel slopes can be seen from the factor $\beta_a \beta_c/(\beta_a + \beta_c)$. For $\beta_a = \beta_c =$ 0.12 Volts/decade, the factor is 0.06, while for $\beta_a = \beta_c =$ 0.60, the factor is 0.3, which is higher by a factor of 5. The corrosion rate in mpy is then calculated from Faraday's Law by the formula:

$$mpy = 0.13 \frac{\text{Equivalent weight}}{\text{Density}} i_{corr}$$

Macdonald, Syrett and Wing have obtained good correlation between polarization resistance measurements and weight loss by calculating the equivalent weight using a composition-averaged atomic weight ($\bar{M}$) and change in oxidation state ($\bar{n}$) [34]:

$$\bar{M} = X_{Cu}M_{Cu} + X_{Ni}M_{Ni}$$

$$\bar{n} = 1X_{Cu} + 2X_{Ni}$$

The mole fractions X_{Cu} and X_{Ni} are calculated from the chemical composition data given in weight per cent. Oxidation states for the copper and nickel are assumed to be +1 and +2 respectively, although others may also be operative.

In the present experiments, the test cell was instrumented to conduct these measurements during several corrosion runs. A Princeton Applied Research Model 173 Potentiostat with a Model 175 Programmer supplying the required input and monitoring was used, with a Hewlett Packard Model 7040A X-Y Recorder for output. To disturb the metal surface as little as possible, an imposed voltage of only $\pm$ 12 mV was applied. Because this "tickling" may affect the subsequent corrosion rate as well as measure the instantaneous rate, the possibility of it affecting the weight loss measurements was avoided by using one specimen for polarization resistance (and SEM analysis in the as-corroded condition), and a separate one

for weight loss (and SEM analysis of the clean surface). Measurements were made at varying intervals throughout the run, with more measurements in the early stages, when corrosion rate was higher. A relatively slow scan rate (0.5 mV/sec) was used to assure accurate results.

Macdonald has recently shown that a sizable error in corrosion rate determination can result from even a scan rate only ten times this value, as well as a sizable hysteresis loop [34]. The scan was done first in the anodic direction and then the cathodic direction, forming a counterclockwise hysteresis loop. It should be noted that these plots were made with the potential on the ordinate and the current on the abscissa; with the axes reversed, the loop would be clockwise. The maximum hysteresis observed was 3.5 μA after 3 minutes. By 10 minutes, it dropped to 0.5 μA and after 15 minutes was not detectable. Using a forward and reverse sweep also gave two curves that could be averaged to get a better value of Δ I. As Walter points out, this curve will be nearly linear only if the Tafel slopes are equal [39]. This was the case in the present study.

To increase the accuracy of results, the effect of IR drop must also be considered. This accounts for the resistance of the electrolyte between the reference and working electrodes. As natural sea water has quite high conductivity, IR drop was neglected in this study. However,

it was found that doubling the exposed surface area (by connecting the potentiostat to both channel specimens simultaneously) did not result in a doubling of ΔI. This may have been due to neglecting an appreciable IR drop, in which case calculated corrosion rates would be too low.

One additional aspect of polarization resistance measurements that has thus far lacked attention is the determination of exposed surface area. In calculating mpy, the original "flat" surface area is customarily used. However, most surfaces actually have more metal exposed than this would indicate, due to surface flaws, undulations and machining marks. Even a 3/0 grade emery finish gives an rms roughness of approximately 10 microinches. The surface roughness often becomes exaggerated as corrosion proceeds. For a metal surface that is 50 per cent covered with hemispherical pits 2 μm in diameter, the surface area exposed to the corrosive liquid is actually 17 per cent greater than a perfectly flat surface. The corrosion rate calculated, by either polarization resistance measurements or weight loss, using the smaller area may then be too high by perhaps half that value: 8.5 per cent. If the corrosion is in the form of hemispherical troughs, as in the present study, the increase in surface area rises to 29 per cent.

IV. RESULTS AND DISCUSSION

A. LEADING EDGE ATTACK

Some investigators, such as Syrett [10] and Ross [40], have reported preferential dissolution of the leading edge of specimens, and attributed this to the establishment of the diffusion mass transfer (or oxygen concentration) boundary layer. Cornet has also mentioned this entrance effect, where the so-called oxygen tension and the copper ion concentration are changing [11]. To check this affect, split samples were placed end-to-end and run at three different velocities in the flow channel. These specimens were made from full-size 90/10 Cu-Ni coupons cut in half, making a total of 4 metal specimens, two on each side of the flow channel. Thus, for 2 of the 4 specimens, the leading edge was preceded by Plexiglas, while the other 2 further downstream were preceded by metal. Results of these tests are shown in Table 4. In all cases except one, the trailing section actually had a greater weight loss than the leading section, differing by a maximum of only 5.2 per cent. The corrosion rate was consistently higher for specimens from one side of the flow channel with a maximum of 18.5 per cent difference. The slight difference in exposed area of the specimens on the opposing sides was taken into account by measuring the specimen length and the channel width on both sides. The reason then must be a flow phenomenon, though the nearest upstream pipe bend is 1 m away, and

TABLE 4

Velocity (m/sec)	Channel Side	Corrosion Rate (mpy) Leading Specimen	Trailing Specimen	Difference (mpy)	(per cent)
4.0	1	6.40	6.74	0.34	6.2
4.0	2	5.33	5.48	0.15	2.8
6.0	1	14.96	14.99	0.03	0.2
6.0	2	13.61	13.35	0.26	1.9
7.8	1	18.31	18.51	0.20	1.1
7.8	2	16.79	16.82	0.03	0.2

Split specimen direct weight loss data taken at various fluid velocities (48 hour tests).

the nearest nonuniformity inside the flow channel is 51 cm away. Microscopic examination showed no preferential attack whatsoever at either leading edge in 48 hours.

Three possible explanations exist besides the diffusion boundary layer concept for why other investigators may have found this preferential attack. First is the problem of uneven mating surfaces. The experiments of Locke have shown that even for a metal tightly bonded in an epoxy mold and subsequently sanded smooth, the metal being harder stays slightly raised above the epoxy [41]. This results in preferential attack at the interface, due to the establishment of the metal corner as a local anode. His tests were done in beakers with stagnant artificial sea water. In a flow situation, the effect of a metal surface sticking out in the flow path would be obviously amplified by the induced turbulence and erosion "tearing" at the leading edge.

The opposite case of an indented or recessed metal surface could easily occur in an arrangement such as that described in this paper. A particle of dirt between the sample and the channel spacers, or an exposed surface slightly rounded at the edge by sanding on a soft table would result in a stream of cavitation bubbles emanating from the leading edge. This was noticed in trial runs, but avoided in all reported runs by careful sample polishing, cleanliness in the sample cavity, and external clamping of the specimens against the channel spacers.

The third difficulty may involve a crevice at the leading edge, yielding cavitation, increased turbulence and crevice corrosion (deficiency of oxygen resulting in accelerated corrosion). This was avoided by machining the specimens slightly oversize and then hand sanding with 3/0 grade emery paper to fit tightly. Microscopic examination revealed a square leading edge as opposed to the slightly rounded edge caused by the milling operation. All of these defects would go unnoticed in an arrangement where viewing of the flow was not possible either because the sample itself was moving or because the apparatus was not transparent. After removal of the specimen, an explanation of the cause of any preferential corrosion would be highly speculative.

These results challenge the design notion that insertion of an entry length of test material is required. It may, in fact, damage the experiment, if it involves recirculation of a fixed volume of electrolyte, by multiplying the metal ion concentration. Additionally, a corrodable entry length may change the flow conditions with time as pitting or surface roughness developes.

Further, in regard to the mass transfer boundary layer, the T-7C-5 Task Group of the National Association of Corrosion Engineers (NACE), in a 1977 review of high velocity sea water corrosion, used the following equation for the boundary layer thickness when the hydrodynamic boundary layer also starts at the same location [42]:

$$\delta_m = \frac{\delta_h}{Sc^{1/3}}$$

where Sc is the Schmidt number equal to ν/D_{O_2}. A larger Schmidt number (approximately 1100 in our case) would give a thinner layer, with a higher concentration gradient. When the formula for the hydrodynamic boundary layer thickness is inserted, this yields

$$\delta_m = \frac{.380\ \nu^{1/5}\ X^{4/5}}{\bar{u}^{1/5}\ Sc^{1/3}}$$

However, this shows that it does not stabilize rapidly at all, but increases in proportion to $X^{4/5}$. A "dummy section" ahead of the test section, would still result in δ_m increasing across the specimen. As Leumer has pointed out from a review of the literature on mass transfer, use of this formula in turbulent flow is inappropriate [43]. In laminar flow, while the formula applies, it shows that use of an entry length would not prevent a concentration gradient across the specimen; the layer thickness does not stabilize.

B. POLARIZATION BEHAVIOR

Figures 19 and 20 show the standard potentiodynamic polarization curves obtained for CDA Alloy 706 (right circular cylinder specimen in a standard corrosion cell flask) in synthetic and natural sea water respectively. Comparison of the two plots shows:

(1) The equilibrium potential is 0.005 volts more negative (cathodic) in natural sea water due to the larger cathodic Tafel slope.

(2) The corrosion current (after ten minutes immersion) is 36.5 μA in synthetic sea water, 54 μA in natural sea water, a 39 per cent difference.

Figure 21 shows a plot that was also done in natural sea water, with stirring from a magnetic agitator. However, this plot was performed in the portable Plexiglas flow channel cell, isolated from the rest of the system by rubber stoppers. This test arrangement was considerably different:

(1) Rectangular sample with an exposed surface area of 7.5 cm^2 (1.16 in^2) vice a right circular cylinder with an area of 6.47 cm^2 (1.00 in^2).

(2) Ag/AgCl reference electrode located 47.6 cm (18.75 in) from the sample with agitation only near the sample itself, vice 5.0 cm (2.0 in) away with agitation around all electrodes.

(3) Platinum (counter) electrode was positioned 1.0 cm from the sample (working electrode), vice a carbon electrode 5.0 cm (2.0 in) away.

The plots are shifted slightly along the current axis due to the different exposed areas of the two types of samples. Comparison of the corrosion current density ($\mu A/cm^2$) shows them to be quite similar -- 8.34 in the standard cell versus 8.40 in the channel, using a cathodic Tafel slope of 0.4 volts per decade. The equilibrium potentials of specimens in the flask and flow channel are -0.23 and -0.24 volts

respectively, and the overall shapes of the curves are likewise very similar. Thus, this flow channel electrode arrangement has been proven to give accurate results, in terms of it reproducing the data in a carefully controlled laboratory test following ASTM Standard G5-72 [44].

Figure 22 is another polarization plot performed in the flow channel approximately one month later. The shapes of the two curves are quite different, although only three known variables had changed:

(1) A carbon counter electrode positioned 39.4 cm (15.5 in) downstream from the specimen was used in place of the platinum electrode positioned directly across the channel. However, similar plots were also run at this time with the platinum electrode and the same anomaly observed.

(2) The sea water temperature was 16.5 vice 14.5°C.

(3) The test was performed with a flow velocity provided by the pump of 6 m/sec, vice the low speed gravity flow. However, tests at the same period with even an isolated test cell produced curves similar to Figure 22. Peterson and Gehring have recently experienced a similar change with tests of low carbon steel [36]. As in their situation, the discrepancy cannot be explained by a variation in oxygen content.

Plots as in Figure 22 were obtained for varying velocities with the following shift toward more negative (more noble) corrosion potentials (after 10 minutes immersion):

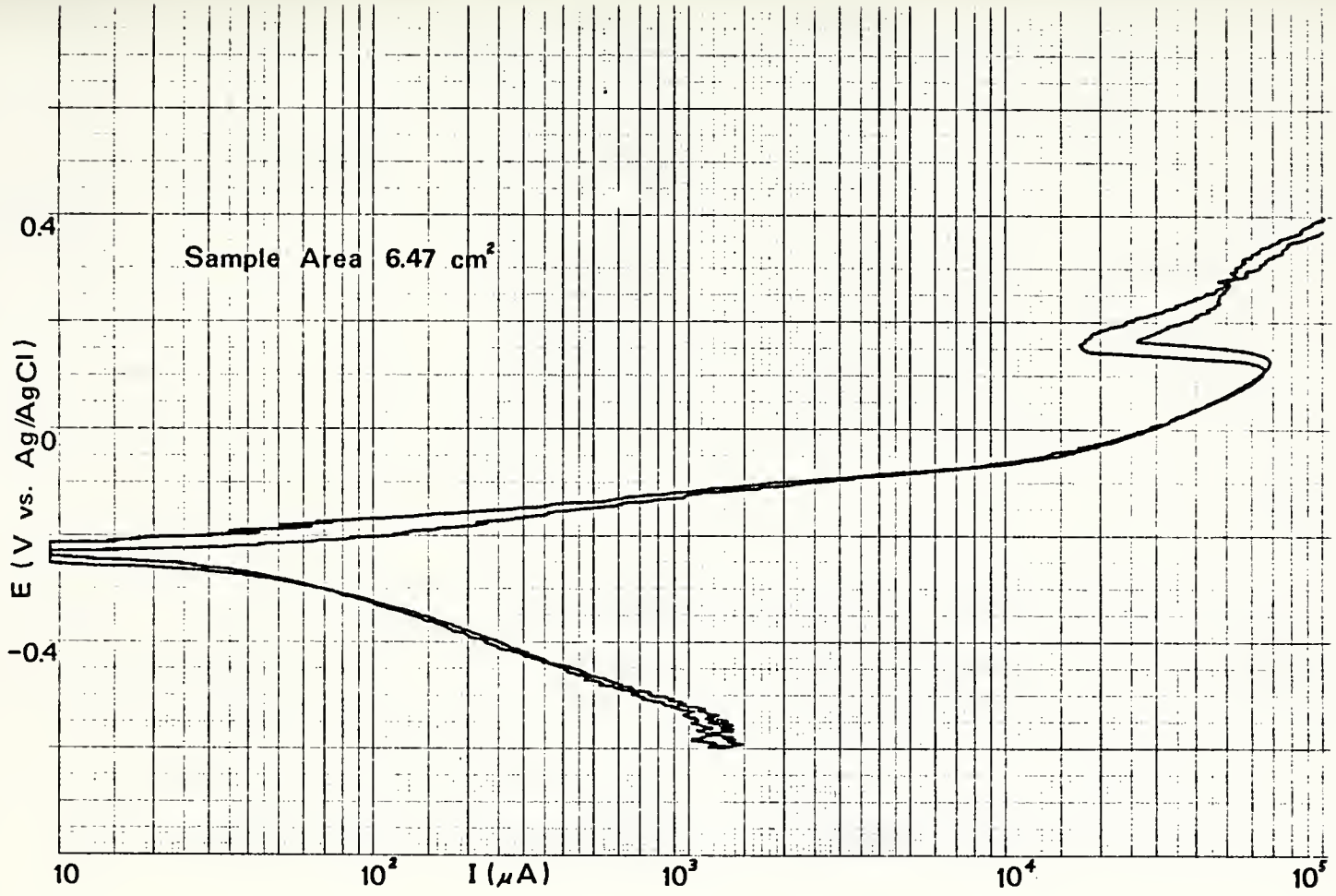

Figure 19. Polarization plot obtained in a standard corrosion cell for 90/10 Cu-Ni in synthetic sea water at 20°C.

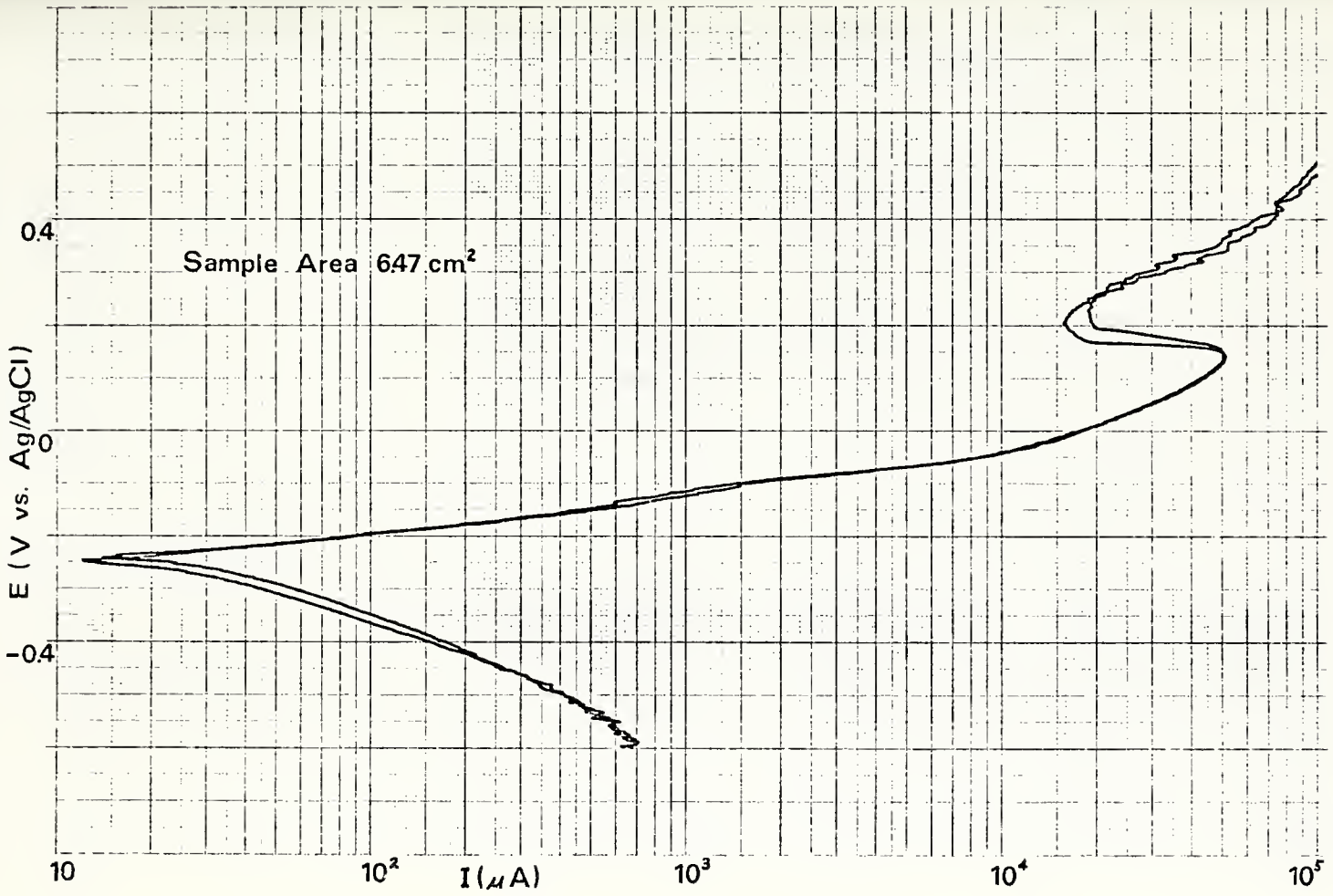

Figure 20. Polarization plot obtained in a standard corrosion cell for 90/10 Cu-Ni in natural sea water at 15.5°C.

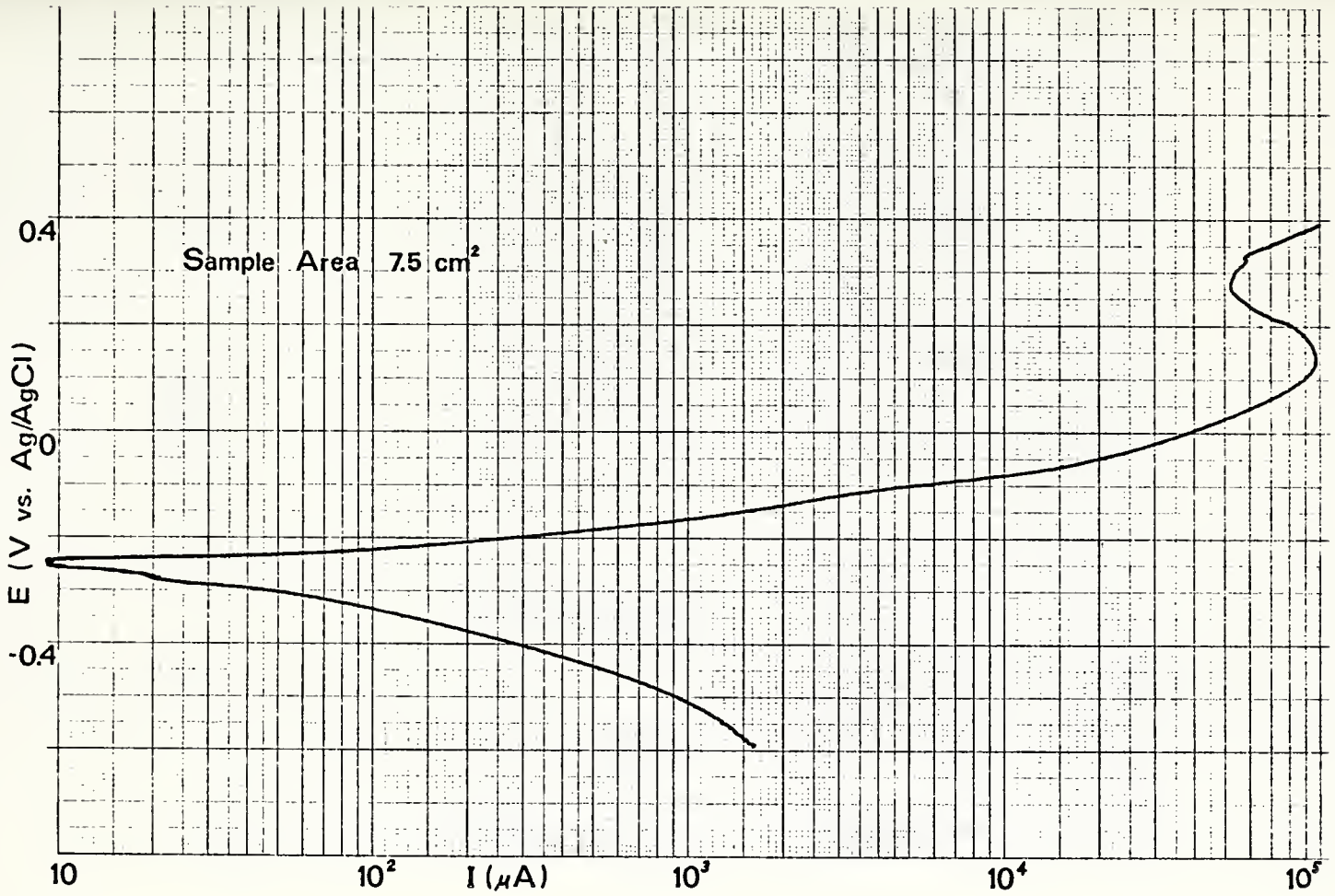

Figure 21. Polarization plot obtained in flow channel for 90/10 Cu-Ni in natural sea water at 14.5°C, gravity flow of 0.5 m/sec.

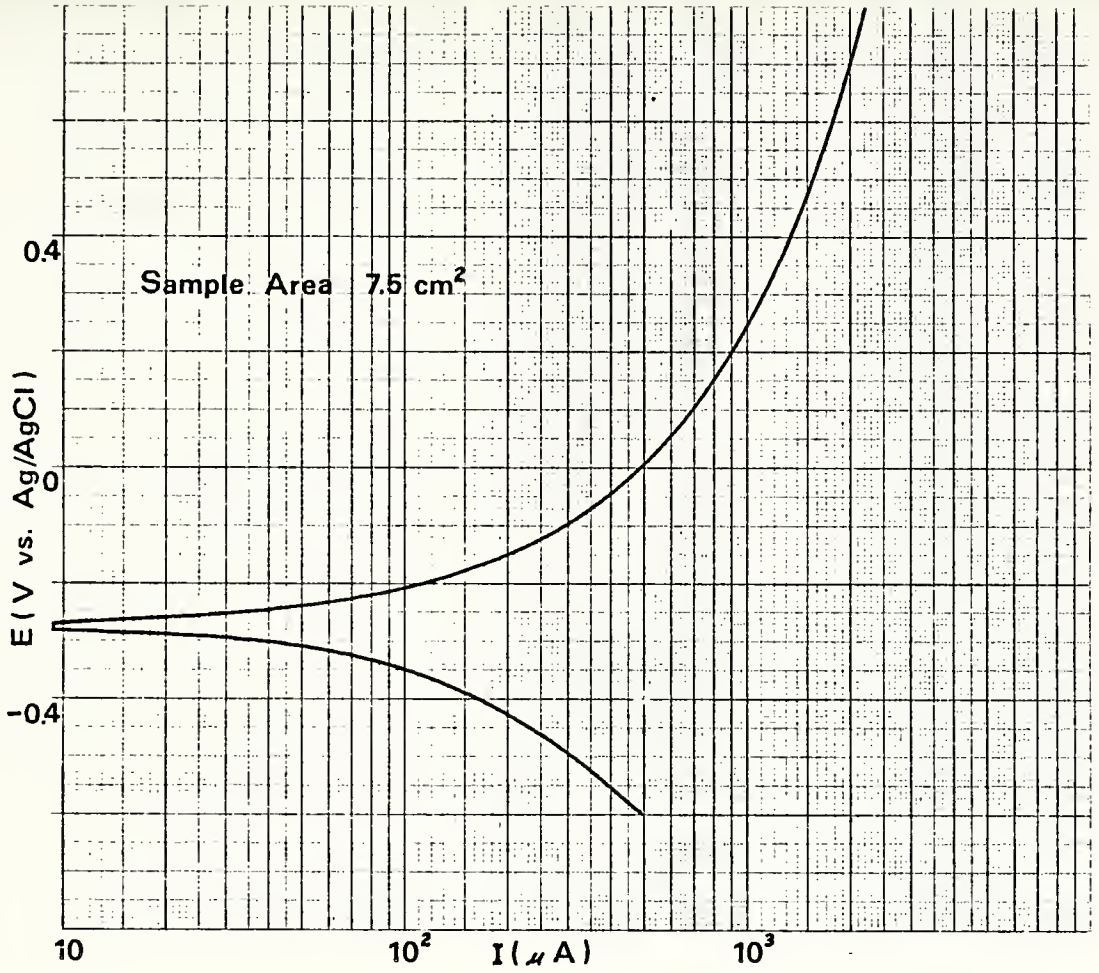

Figure 22. Polarization obtained in flow channel for 90/10 Cu-Ni in natural sea water at 16.5°C, pump flow of 6 m/sec.

Velocity (m/sec)	E_{corr} (Volts vs. Ag/AgCl)
2.0	-0.265
4.0	-0.270
6.0	-0.273
7.8	-0.276

Additionally, the slope of the anodic portion of the curve increased slightly with increased velocity, showing an increase in the corrosion current (I_{corr}). The switch-back shown in Figures 19, 20, and 21, at a potential of about 0.15 volts, corresponds to a change in corrosion mechanism: the formation of black film, probably cuprous oxide (CuO). This oxide layer was observed while making all 3 of these plots, but not during construction of Figure 22.

C. EFFECT OF VELOCITY ON CORROSION RATE

Velocity effects vary from alloy to alloy depending mostly on their respective film formation characteristics. While some alloys form very tenacious protective films, others form easily perturbed film and still others none at all. Copper alloys typically form films that withstand attack remarkably well at low velocities; a slight increase in corrosion rate with velocity is usually seen, due to enhanced oxygen transport. However, as velocity increases, a point is eventually reached where the film breaks down and typically begins to be locally removed. Danek lists this so-called

breakaway velocity as 4.5 m/sec (15 ft/sec), for 90/10 Cu-Ni [5], while Syrett showed it to also be a function of the test system geometry [10]. It is undoubtedly a function of both average velocity and geometry, but more fundamentally a function of the flow structure very near the metal surface. At very high velocities, another regime may be encountered where a film cannot form and corrosion rate stabilizes, but this is well above the range of interest of the present study and of present day technological applications.

Due to lack of a fundamental model, corrosion rates in this study are simply plotted versus average velocity, as is typical in "velocity-effects" studies. In comparing corrosion rate results from various sources, the means of estimating the average velocity which is cited must be kept in mind. Usually, in tube flow experiments the average flow velocity is calculated from the quantity of water moving through the tube divided by the cross sectional area of the tube; this gives a velocity that is less than the centerline velocity, although the difference decreases with increased flow rate. On the other hand, systems that employ a rotating or revolving electrode use the relative free stream velocity which, stirring effects neglected, gives a velocity higher than the average.

The corrosion rates at varying velocities from the present study are shown in Table 5 and Figure 23. Direct weight loss measurements were converted to mpy for all runs. For

TABLE 5

VELOCITY (m/sec)	VELOCITY (ft/sec)	Channel	CORROSION RATE: Calculated by Direct Weight Loss (mpy)		CORROSION RATE: Calculated from Polarization Resistance Measurements (mpy)
4.0	13.1	Open	6.37	6.32	---
			6.71	5.47	
4.0	13.1	Mesh	6.21	6.04	---
4.0	13.1	Open	6.95	6.34	---
4.0	13.1	Mesh	6.74	6.56	---
6.0	19.7	Open	14.96	13.61	4.63
7.8	25.6	Open	13.73		4.88
7.8	25.6	Open	18.31	16.79	---
			18.51	16.82	

Corrosion rates of 90/10 Cu-Ni as calculated directly from weight loss data and from polarization resistance data (48 hour tests).

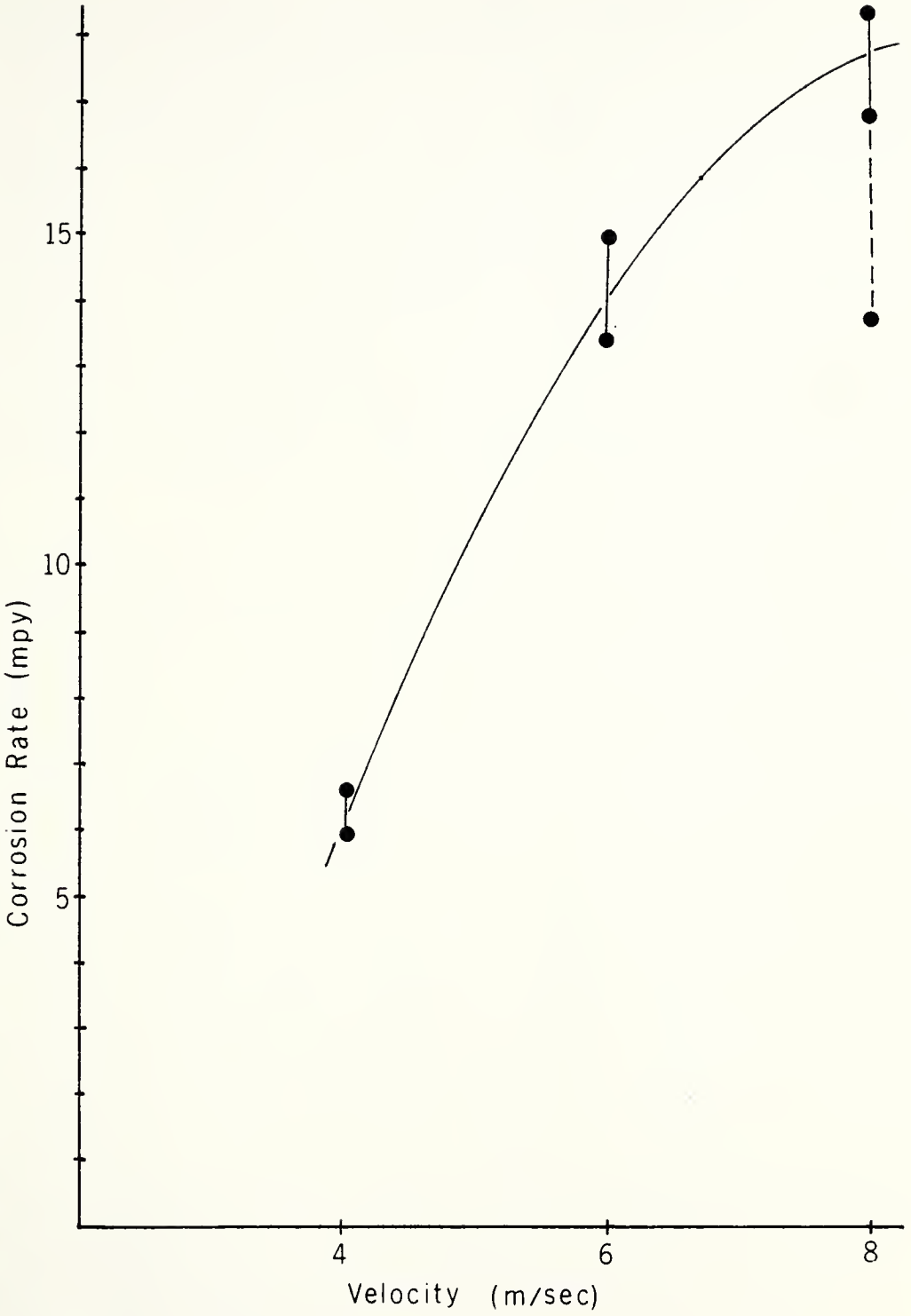

Figure 23. Experimental results of flow channel tests on 90/10 Cu-Ni, 48 hours in natural sea water.

comparison of calculated corrosion rates, polarization resistance data was also taken for 2 of the runs, and converted to mpy. By integrating the area under the curve of polarization resistance versus time, an average corrosion rate was calculated, for comparison with the direct weight loss determinations. In these two methods, the following errors and uncertainties are present:

(1) Flow adjustment, as read from the rotometer.

(2) Varying temperature, salinity, pH, dissolved oxygen content.

(3) Measurement of exposed surface area of the specimens.

(4) Electrical and hydrodynamic noise in the polarization resistance plots.

(5) Weighing of specimens during use of the analytical balance or due to incomplete removal of corrosion products.

(6) Correction for IR drop was not included.

The calculations of corrosion rate (mpy) from polarization resistance measurements (Table 5) were based on Tafel slopes, β_a and β_c, of 0.12 volts per decade, considered an average for many metal/electrolyte systems. Due to the shapes of the polarization curves in Figures 21 and 22, actual Tafel slopes would be impossible to measure accurately. The curve in Figure 21 shows slopes of approximately 0.08, although for the cathodic portion this estimation is extremely arbitrary. Use of these values would yield calculated corrosion rates 33 per cent lower than those found using 0.12.

At the other extreme, Figure 22 shows no linear portion; a slope of 0.6 (or even higher) could be selected. Using 0.6 would increase the calculated corrosion rates 400 per cent above the 0.12 based values. Even 0.2 would yield a 67 per cent increase. Thus, unless accurate Tafel slopes are known, polarization resistance data is most useful in observing trends, i.e. relative changes in corrosion rate (with time and/or velocity), as opposed to measuring absolute values.

All of the corrosion rates calculated in Table 5 from direct weight loss measurements are higher than those found by other investigators (Figure 1) especially at 6 and 7.8 m/sec. Since tests in the present study were only of 48 hour duration (vice times of up to months in other studies), and since the corrosion rate decreases with time, these higher initial values are to be expected.

These corrosion rates have been compared to those found by Leumer using a circling foil apparatus and synthetic sea water [43]. Natural sea water is a more aggressive environment, as shown by the higher value of I_{corr} for natural sea water (Figures 19 and 20). In spite of this fact, the corrosion rates in the flow channel averaged approximately 20 per cent lower than those for the circling foil at 4 m/sec. This suggests that some additional factor of corrosion was experienced on the circling foil, such as due to erosion by entrained bubbles, or due to higher turbulence intensity.

At 6 m/sec, the situation was reversed, with the flow channel giving corrosion rates roughly 50 per cent higher than the foil. While the explanation for this reversal is not known, it does support the conviction that better modeling of the corrosion process is required.

Only one of the possible inlet meshes was used in the present study, with the mesh oriented at a 45 degree angle to the channel walls, and spacing between filaments of 2.36 mm. Reference to Table 5 shows that, at least for a fairly low velocity (4 m/sec), insertion of a mesh at the test cell entrance had no effect on the corrosion rate (as calculated by weight loss). Either the change in turbulence near the metal surface had no effect on corrosion, or the change in turbulent structure introduced by the mesh disappeared by the time the flow reached the sample; the latter is believed to be the case.

Figure 24 indicates the dramatic effect of temperature on corrosion rate. After the first few hours, as the protective film develops, the corrosion rate would be expected to decrease. However, in the case shown in Figure 24, the temperature rise dominates the corrosion rate, causing it to increase over 60 per cent. That the two variables follow so closely is certainly interesting, but the data is too limited to be conclusive. Syrett has summarized the literature on the effect of temperature [10]. Various investigators have found the corrosion rate to increase, decrease or be unaffected

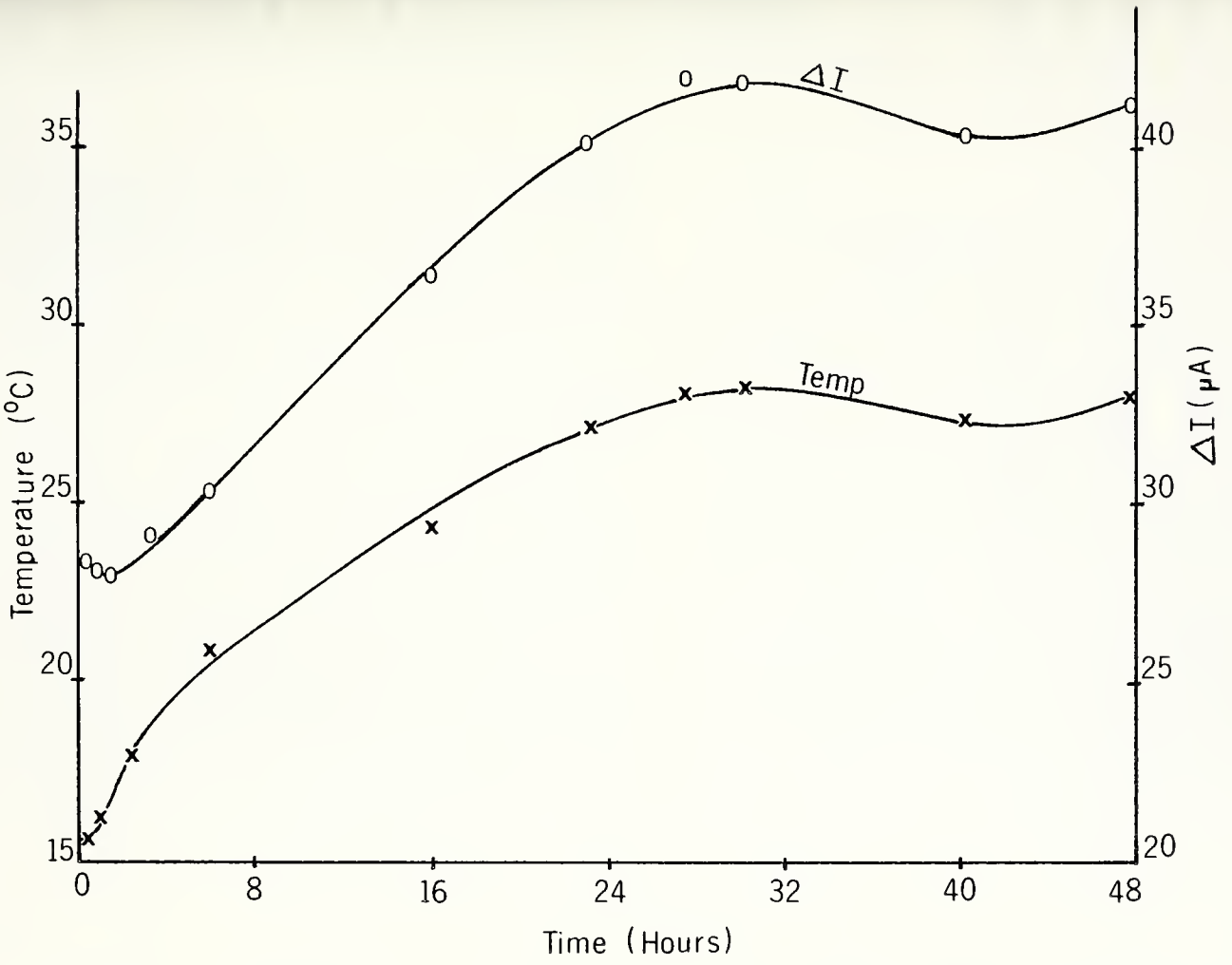

Figure 24. Variation of temperature and corrosion rate during test at 6 m/sec. Sample area = 7.5 cm^2, ΔE = 0.020 Volts.

by an increase in temperature. Syrett attributes this variation to varying dissolved oxygen solubility and differences in the uniformity and tenacity of the corrosion product film. For the case presented here, the oxygen content only dropped from 6.8 to 5.6 ppm, with the initial drop to 5.8 in the first 24 hours. The interdependence is obviously a complex one.

D. SURFACE MORPHOLOGY

Figures 25(a) and (b) are SEM photomicrographs taken at 1100X and 2300X respectively of the cleaned surface of a specimen which had been corroded for 48 hours at 7.8 m/sec (25.6 ft/sec). Comparison with Figure 18(b) will point out the preferential dissolution along certain crystallographic planes within the base metal grains. The preferentially attacked areas are those which first become covered with corrosion products. As Tait points out, oxygen concentration cells then form and subsequently initiate pits [45]. Pores, ruptures and flaws in the film ensure uneven diffusion of oxygen, allowing oxygen concentration cells to keep these new pits growing.

Metallic copper that is removed from the surface goes either into the corrosion product film (Cu_2O), or into solution as ionic copper (toxic to some marine life), or forms a precipitate in the solution. In tests with 90/10 Cu-Ni in 0.1 per cent NaCl, Popplewell found that for the first 100 hours, more than 80 per cent of the metal lost was used

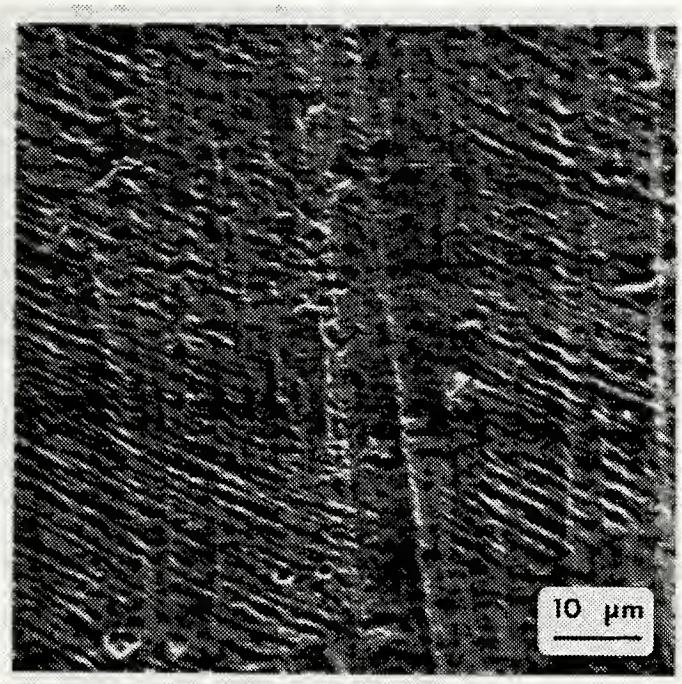

(a)

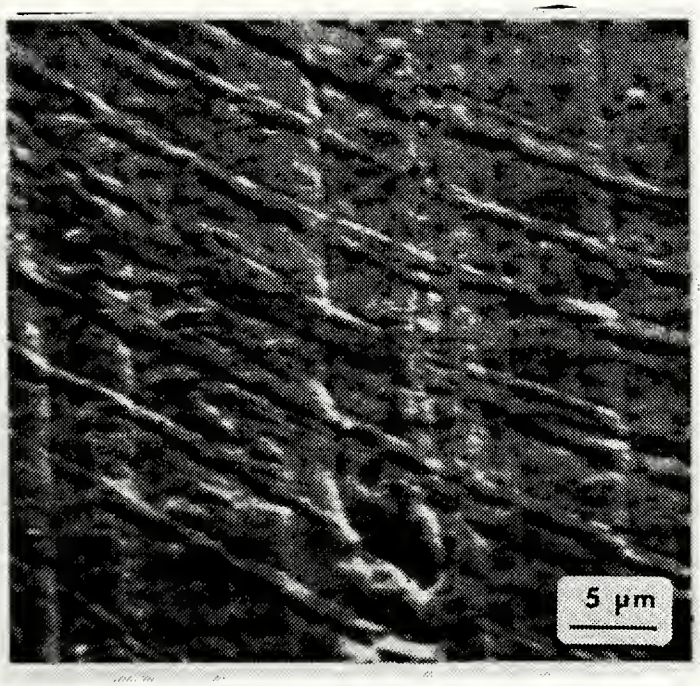

(b)

Figure 25. SEM photomicrographs of cleaned surface of specimen exposed for 48 hours at 7.8 m/sec. Direction of fluid flow is horizontal, polishing lines vertical. (a) 1100X (b) 2300X

to form a protective film. Only after 1000 hours had the film thickness stabilized, with all the metal subsequently lost going into solution [46]. Samples in the present experiment, run at 4 and 6 m/sec (13.1 and 19.7 ft/sec), showed no visible signs of corrosion product buildup after 48 hours time; the corroded surface was essentially featureless with small, random groups of shallow pits. Weighing the specimen before and after post-exposure cleaning showed only a negligible weight change (less than 0.01 mg/cm^2). However, the samples run at 7.8 m/sec formed a "streaky" corrosion product layer on top of trough-like pits, as shown in Figure 26. Of the weight loss during corrosion, 8.9 to 10.8 per cent was found to be in the corrosion product that adhered to the metal surface. While wet, the corrosion product was rust-colored and easily wiped off. When dry, it was tightly adhered, purple to the naked eye and green under the microscope. In order to get a view of the corrosion pits at a further stage of development, but without running a longer test, a specimen was coupled to a platinum electrode of the same exposed surface area located directly across the channel. The resultant uncleaned surface of the specimen exposed in this galvanic couple is shown in Figure 27. The pits are larger than in an uncoupled specimen, as expected, but there is a lack of corrosion product buildup.

The streaks of corrosion products and pitting parallel to the direction of flow indicate a strong dependence on

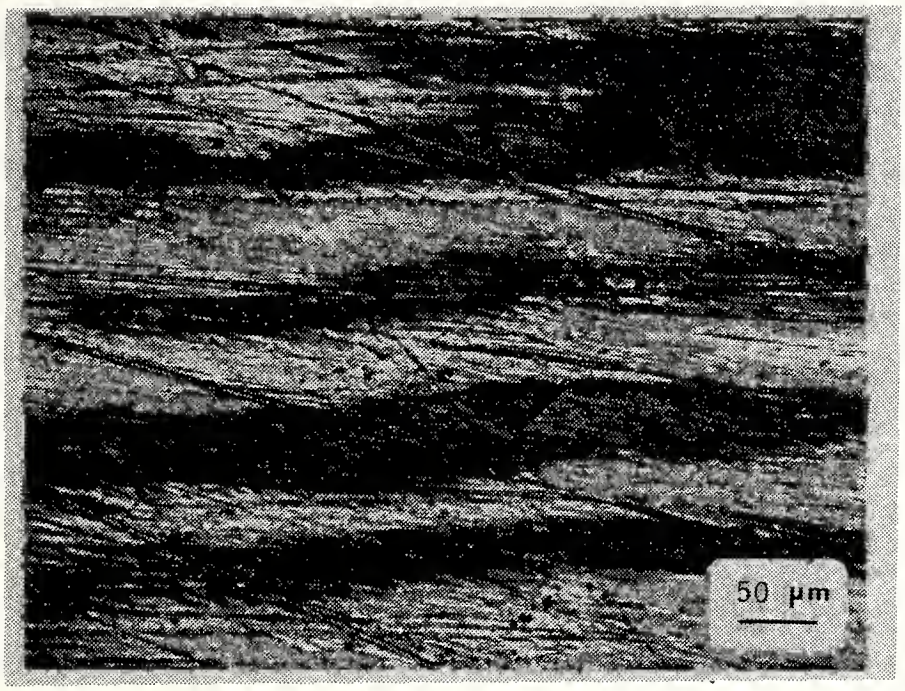

Figure 26. As-exposed surface of specimen exposed for 48 hours at 7.8 m/sec. Flow direction is horizontal, polishing lines vertical. (200X)

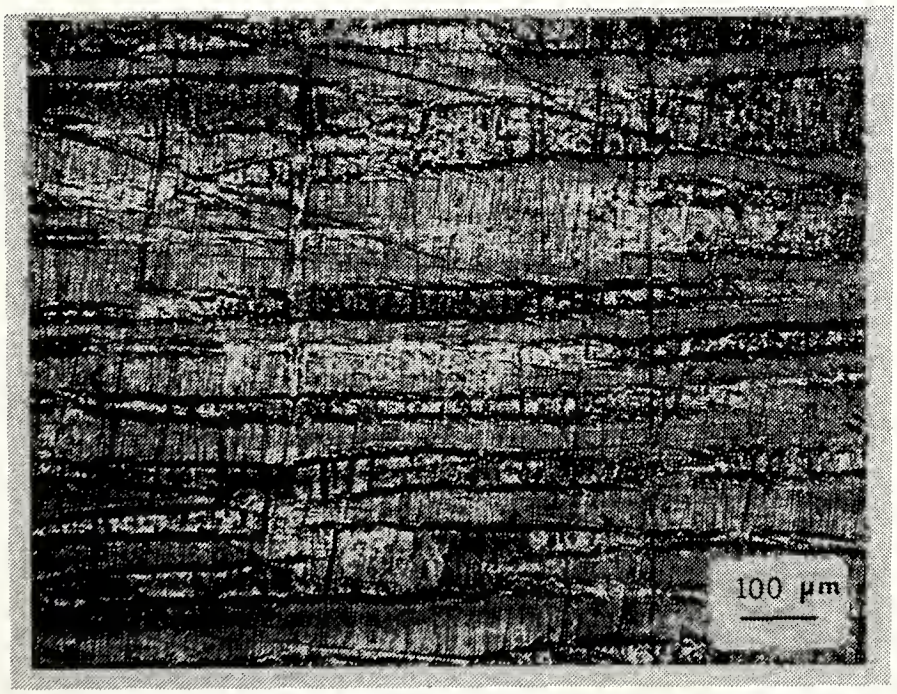

Figure 27. As-exposed surface of specimen exposed for 48 hours at 7.8 m/sec, coupled to a platinum electrode on the opposite side of the channel. Flow direction is horizontal, polishing lines vertical. (100X)

flow phenomena. These streaks are spaced more closely than the structural streaks referred to earlier (Figure 18(a)) and they are more periodic in distribution and more uniform in size. It is doubtful that they are connected directly to the turbulence concept of streaks of fluid lifting off the wall (the process of bursting described later in this paper) as this bursting is a more random phenomenon than the distribution of corrosion attack seems to exhibit. The periodicity and elongation in the line of flow do appear to be strongly influenced by the flow, perhaps in a manner similar to the production of period sand ripples on the ocean floor (also discussed in a later section).

The green color of the corrosion product indicates it to be a copper hydroxychloride [34]. However, potential-pH diagrams which show the thermodynamically stable forms of the metal and its corrosion products, show that conditions in the present experiment fall within the stability range of cuprous oxide. No corrosion product was observed to collect on the in-line filter.

E. STRUCTURE OF TURBULENCE

1. General Concepts

For the practicing engineer, the more of the details of turbulence that can be neglected the better. However, in this section it is necessary to go into some detail to give the reader at least a "gut feeling" of which turbulence parameters may be important to corrosion and why. We will

specifically restrict ourselves to a discussion of the turbulent (vice laminar) flow regime. As Prandtl pointed out in 1934, many, if not most, problems of interest in real life fall into this category [12]. For example:

(1) Flow through a smooth pipe with inside diameter 2.54 cm (1.00 in) will be turbulent (Re_d greater than 2300) for any flow rate over 0.65 liters/min (0.17 gal/min), i.e. average velocity above 0.11 m/sec (0.35 ft/sec).

(2) Flow through a 15.24 cm (6.0 in) smooth pipe will be turbulent above 0.11 liters/min (0.03 gal/min), 0.02 m/sec (0.06 ft/sec).

(3) For a given velocity of 1 m/sec, the maximum pipe diameter that would maintain laminar flow would be 0.24 cm (0.09 in), giving a maximum flow rate of only 0.27 liters/min (0.7 gal/min).

(4) Flow along a ship from a point 1 m from the bow to the stern would be turbulent (Re_x greater than 5×10^5) for all velocities greater than 0.51 m/sec (only 1.01 knots).

(5) For a given velocity of 5.08 m/sec (10 knots), the laminar portion of the flow along the ship would be confined to the first 51 cm (20 in).

Figure 28 shows the two flow regimes as well as flow that cannot clearly classified as either (so-called transition flow).

In corrosion, we are concerned with wall (vice free) turbulence, i.e. turbulence generated and continuously

Figure 28. Pipe flow. (a) Smooth laminar flow. (b) Flow no longer stable, transition flow. (c) Fully turbulent flow. From Streeter and Wylie [47].

affected by friction forces at the wall, as opposed to that produced by interacting flow of fluid layers with different velocities in the absence of walls. In wall turbulence, the small scale structure is much less uniform than it is in free turbulence. The turbulent boundary layer consists of flow in a continuous state of transition. A few generalizations about wall turbulence include:

(1) It is a random phenomenon, but with a quasi-permanancy and quasi-periodicity in time and space (i.e. repeats in time and space, but not periodically at one place in time nor at one time in space).

(2) It is characterized by a strong diffusive nature.

(3) Dissipation of turbulence occurs due to viscous forces, mainly in the region of the smallest eddies, with kinetic energy converted to heat.

(4) It is anisotropic, i.e. the mean velocity shows a gradient associated with the shear stress.

(5) It can be generated only by velocity gradients in the flow.

(6) Streamlines lose their identity.

(7) The laminar sublayer becomes very thin and decreases with increased velocity.

(8) The average velocity approaches the free stream or centerline velocity, with the mean velocity gradient changing rapidly near the wall. This is shown in Figure 29 at intermediate Reynolds numbers. The profile becomes even more "square" with increasing Reynolds numbers.

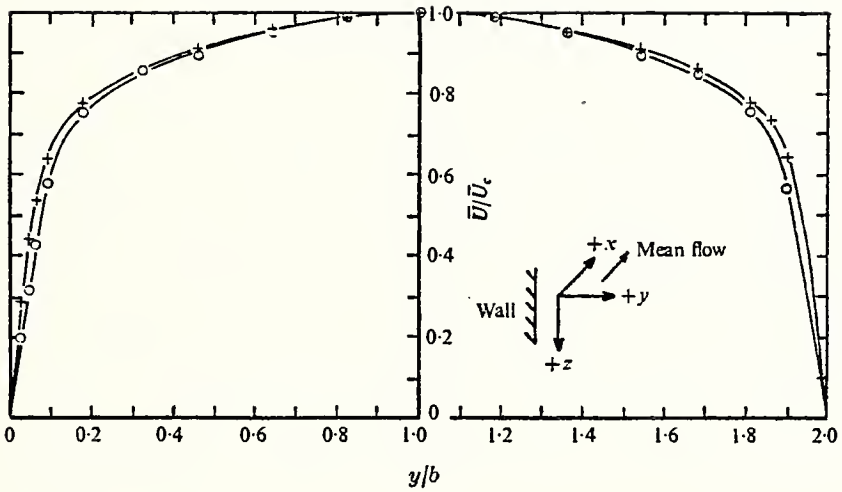

Figure 29. Velocity profile across an open channel with Re_d = 5600 (o) and 8200 (+). From Eckelmann [48].

(9) Turbulence measurements are often normalized with wall parameters. The friction or shear velocity u_f is defined by $(\tau_w/\rho)^{1/2}$, and is computed from the slope of the mean velocity profile near the wall. Distance from the wall is then non-dimensionalized as $y^+ = yu_f/\nu$ and velocity normalized as $u^+ = \bar{u}u_f/\rho$ with dimension of sec^{-1}.

For flat plate or pipe flow, the velocity profile near the wall is given by the universal velocity distribution law:

$$u^+ = \frac{1}{k} \ln y^+ + c$$

Very near the wall, in the viscous region, this reduces to $u^+ = y^+$. Plotted on semi-log paper, Figure 30 shows this relationship. Varying constants have been found by investigators. For example, Wallace [49] found $1/k = 2.5$, while Eckelmann [48] got 2.65. C is a function of both surface roughness and Reynolds number; typical values obtained by the above investigators were 5.5 and 5.9.

Figure 31(a) shows an instantaneous trace of the axial flow velocity. Coupled with Figures 2 and 28, these indicate somewhat the complexity of turbulence. On a macroscale, turbulence is a disordered phenomenon. When repeating velocity patterns are viewed at a fixed point, they are never sufficiently periodic to be clearly identifiable. This irregularity makes it impossible to describe all the details of the motion in terms of space and time coordinates. The approach then is to describe it by laws of probability, indicating mean, average or rms values.

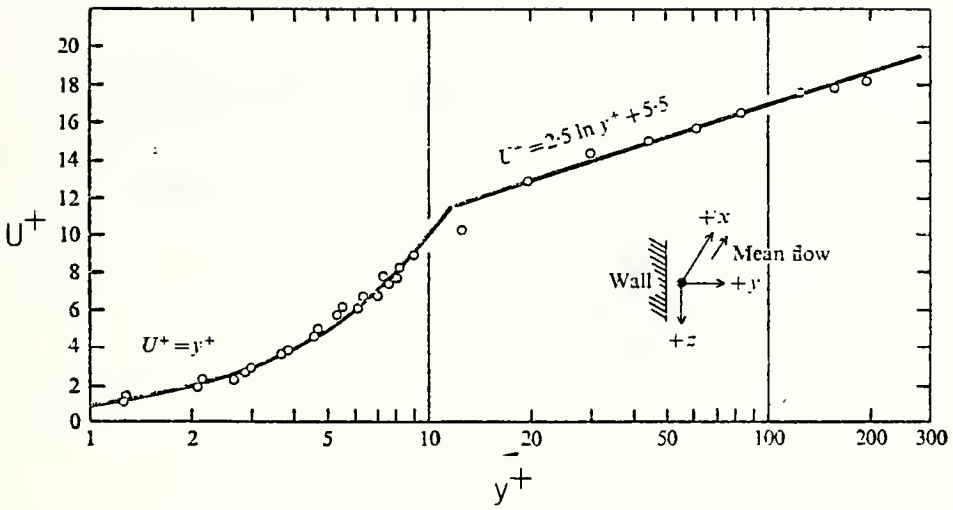

Figure 30. Turbulent velocity distribution at Re_d = 7150. From Wallace [49].

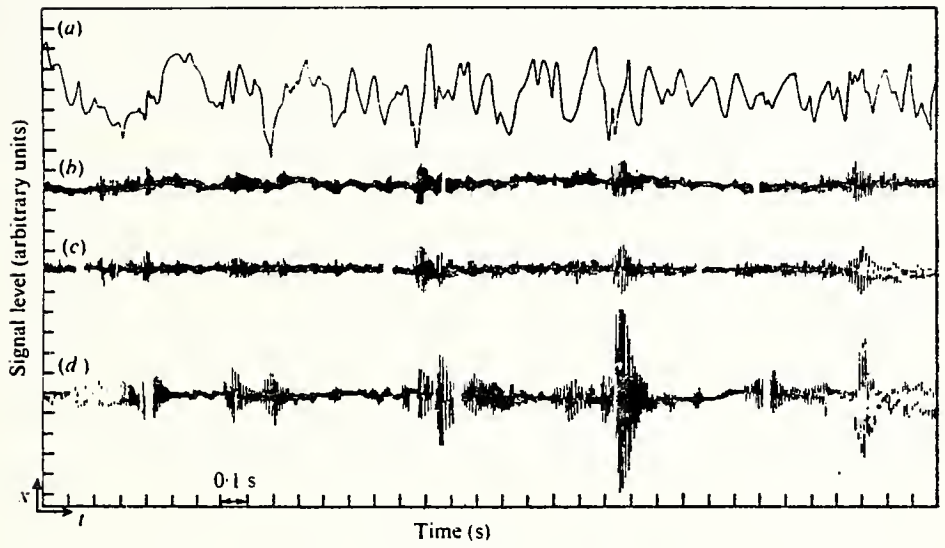

Figure 31. Burst identification. (a) Axial velocity u_1. (b) Signal from spectrum analyzer. (c) Time derivative du_1/dt. (d) Spatial derivative du_1/dr. From Heidrick, Banerjee and Azad [50].

2. Burst/Sweep Phenomenon

The overall turbulence models that have been proposed usually consist of two parts:

(1) An organized component with a quasi-periodic motion of larger eddies, perhaps modeled by wave theory.

(2) A more random type of background turbulence, modeled as small eddies or noise.

The precise mechanism which triggers wall turbulence is not fully understood. What is known is the sequence of events that occur in the turbulent region. The scenario based on visual studies near the wall by Kim, Kline and Reynolds reads somewhat like a movie script [51]. They observed that "streaks" of slow-moving and fast-moving fluid side by side flowed along the wall; randomly, a low speed streak lifted away from the wall, developing into vortices which migrated from the wall, and then broke up into more chaotic motion; these periods of intense activity interspersed with relatively quiescent periods have been termed "bursts" and "sweeps."

For a surface phenomenon like corrosion, this model of streaks lifting away from the wall, disintegrating and smashing back into the wall has obvious implications. Where the corrosion rate is controlled by the buildup of a protective film, a more rapid replenishment of oxygen convected directly to the surface would build up the film faster and perhaps make it thicker. Either event, the movement of fluid away from the surface or its return could interupt the protective film, exposing fresh metal.

Offen views this phenomenon of low velocity fluid erupting into the high velocity region as akin to separation caused by a temporary local adverse pressure gradient [52]. This pressure oscillation would be caused by the arrival of a sweep (circulatory motion) as it passes over a newly forming streak. This correlates with Wallace's observations that sweeps precede bursts, followed by new sweeps further downstream [49]. The fluid returning to the wall spreads out sideways and is quickly retarded by the strong viscous forces near the wall. Thus the streak-lifting seems to be triggered by large scale disturbances already present in the flow; as Naraynanam has pointed out, this is not entirely a wall phenomenon at all [53].

Alternatively, Michalke explained bursting as a result of a locally unstable laminar shear layer which had lifted up and rolled into two counter-rotating vortices that roll around each other and coalesce [54]. Figure 32 shows a computer analysis by Acton of such a mechanism [55]. In this pairing, a vortex from a previous burst upstream would pass over a vortex associated with a wall streak, with portions of it moving toward the wall to provide fluid for the next streak. As these vortices would not usually be vertically aligned, complex motions would result.

Figure 31(a) shows how the axial velocity u_1 may vary with time. Only by passing the unprocessed signal through a spectrum analyzer, Figure 31(b), or by taking the time

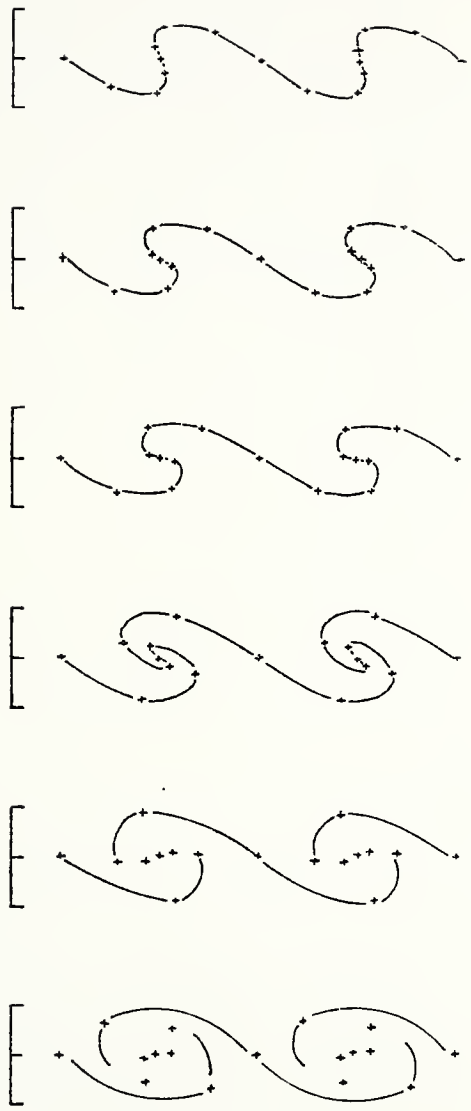

Figure 32. Development of a vortex sheet at varying instants in time. From Acton [55].

derivative of the signal before filtering, Figure 31(c), or by using the filtered spatial derivative of the velocity, Figure 31(d), do bursts become apparent.

Bark has hypothesized that the large scale eddies are excited by the small scale ones through the bursting mechanism. Periodically, these large eddies would create conditions suitable for initiation of new bursts [56]. Landahl conversely proposed that bursting was due to the focusing and trapping of small secondary instability waves on the large scale eddies [57].

Whatever the mechanism, Bremhorst has shown that the erupted low momentum fluid diffuses through much of the boundary layer, so that this is not at all a totally localized event [58]. Sabot observed the bursts to originate across most of the boundary layer, and then travel across the flow approximately equal to their streamwise extent [59]; he found that the ejected vortex filaments may persist across the entire boundary layer, this being an important basic mechanism responsible for turbulent transport controlling heat, mass and momentum transfer. Sabot proposed that the large scale bursting is also responsible for transport of shear stress, with the fine scale structure possibly imbedded in the bursts, forming the high frequency part.

A burst then is characterized by the outward ejection of low speed fluid in the form of small jets with high frequency energy, where the fluctuating streamwise velocity u_1' is low

or decreasing. A sweep exhibits the inward rush of fluid toward the wall, when u_1' is high and increasing. Deceleration seems to promote turbulence, while acceleration has a damping effect. Most of the production of turbulence occurs during these bursts. However, in a fully turbulent region, they may be obscured by background turbulence. Increased Reynolds number corresponds to increased burst rate, and therefore increased energy production. The corrotion rate also, in general, increases with velocity, perhaps closely tied to the increased burst rate. This burst rate would determine how often parcels of fresh oxygen were delivered right to the doorstep of the corroding local anode.

A similar mechanism has also been observed in fully developed pipe flow by Corino and Brodkey [60]. Their analysis pointed to several stages:

(1) Local deceleration of a large portion of the flow near the wall.

(2) This slower fluid forced to accelerate slightly above the wall by faster moving fluid.

(3) The resultant strong shear layer near the wall leading to a small parcel of low velocity fluid being rapidly ejected outward.

(4) Followed by a sweeping motion of high speed fluid from upstream toward the wall.

Together, these events (bursts and sweeps) produce a stress considerably greater than the total Reynolds stress (shear stress due to inertial forces). Wallace has shown localized regions where dissipation is several orders of magnitude greater than the average at the wall [49]. Eckelmann has found instantaneous values of Reynolds stress with peaks 30 times the mean value in the viscous sublayer itself [48]. Hinze found instantaneous values of shear stress 60 times the local value just prior to and during a burst [19]. The vortices can contribute to the shear stress only when they suffer significant deformation in cross section or lateral movement, which occurs most strongly during coalescence [61]. As the width of the eddies increases, so does the shear stress [62].

If wall shear stress is to be considered to have an effect on corrosion, it is these fluctuation peaks that are most important. Using pressure drop measurements, Macdonald [34] has calculated the average wall shear stress at 1.62 m/sec (5.3 ft/sec) to be 0.00154 pounds force per square inch. Using the Moody diagram for pipe roughness, at 6 m/sec in the square flow channel of the present study, the calculated values for τ_w range from 0.014 for smooth pipe to 0.048 for a relative roughness (peaks divided by pipe diameter) of .05. With fluctuations of two orders of magnitude in the shear stress, it would indeed seem possible that τ_w strongly affects corrosion product buildup and even film removal. Shear stress considerations are different in pipe flow and external flow, since the velocity gradients perpendicular to the wall vary.

The wall region in pipe flow is often called the constant stress layer, due to small deviations in τ_w. In fact, one definition of the entrance length is that point at which the wall friction factor reaches a constant value. The maximum values of turbulence intensity near the wall mainly govern wall pressure fluctuations (p_w'), which are in turn directly related to the wall shear stress [19]:

$$\tau_w = p_w'/2.56$$

3. Large and Fine Scale Turbulence

Turbulence is a superposition of eddies of various sizes and energies; there are no distinct separate vortices. The kinetic energy contained by these various sized eddies is determined by their vorticity or intensity of velocity fluctuations. An energy spectrum shows how the energy is distributed according to the various frequencies. In general, eddy size decreases as the wall is approached, but is size-limited by the fluid viscosity. Increased velocity decreases the lower size limit, while the upper limit is determined mainly by the test apparatus size.

An inherent problem in the characterization of flow situations with widely varying eddy sizes is one of scaling. Ideally, by including certain factors in the empirical results, one should be able to apply them to any possible flow situation. But considering the marked differences between the flow within a small test apparatus and along the side of

a ship (where vortices may be several meters wide), it is not surprising that this is indeed not the case. However, controlled small-scale testing is still of great value. Parameters that are important in small-scale tests will also be important in service situations, although not to the same degree. Knowledge of how these parameters affect corrosion is of great value, and small-scale testing can establish trends and reduce the requirement for full scale testing.

The energy spectrum shown in Figure 33 indicates the range of eddy size (inverse of wavenumber or frequency) and their corresponding energies. Frequencies in a single flow field may vary from 1 to 10,000 cycles per second. The eddies that contain the most energy are neither the largest nor the smallest. However, the larger, more permanent ones may still contain 20 per cent of the total energy. As eddy size decreases, dissipation by viscous forces increases, up to a maximum for a certain sized eddy [19]. Bremhorst has shown that the dominant role in momentum transfer near the wall is played by only a limited frequency band [58]. In pipe flow, he has delineated two momentum transfer processes:

(1) A net positive transfer in the high frequency range.

(2) A net negative tranfer that returns low momentum fluid to the wall at the lower end of the spectrum.

Difficulties arise in the use or analysis of energy spectrums. Davies has pointed out that a trace is not like a fingerprint for turbulence; it doesn't represent even a

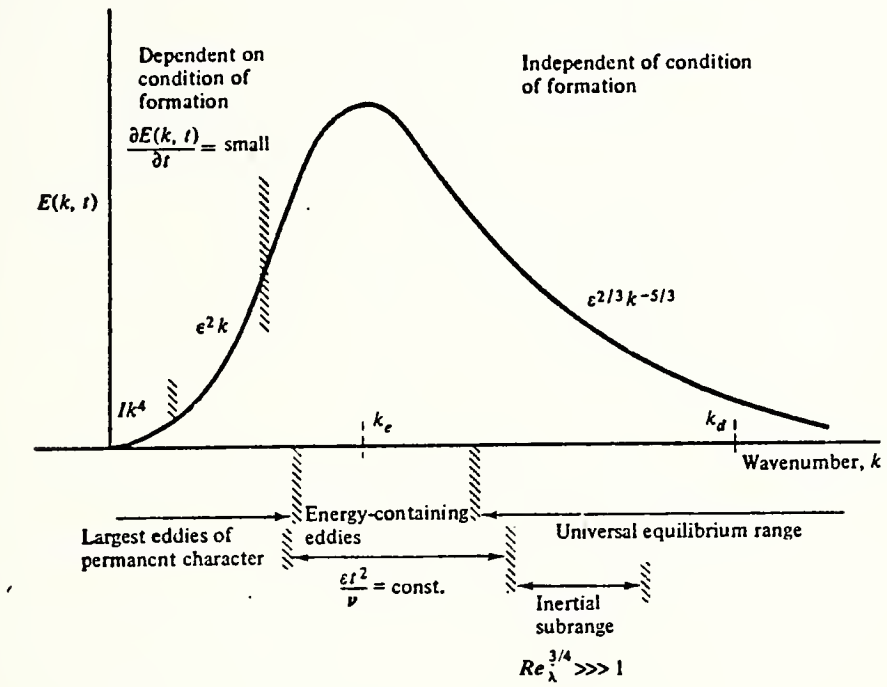

Figure 33. Energy spectrum in turbulent flow. From Hinze [19].

blurry one [61]. Even in one specific region, a wide spectrum will be present, not a single peak corresponding to the preferred eddy size at that location. Due to averaging that is done, even the existence of a particular frequency does not necessarily imply the existence of a corresponding identifiable coherent structure in the flow. Finally, even an array of organized structures of similar scales may produce a broad spectrum.

The various sized eddies may move at different velocities, and be inclined to the wall, some from 5 to 15° [19]. Mean shear acts to amplify preferred eddy structures while others decay.

Large eddies interact with smaller ones, affecting them in several ways:

(1) Deformation of the smaller by shear flow of the larger; Moore has found the elliptical deformation of vortices due to the irrotational straining field of nearest neighbors [63].

(2) Entrainment of the small eddies by the flow velocity caused by the bigger eddies, particularly for eddies of widely differing size.

(3) Transfer of energy from the larger to the smaller (accounted for by viscosity), resulting in a cascade process for breakdown of eddies.

The structural features of large eddies include:

(1) Pairs of contra-rotating streamwise vortices.

(2) Attached eddies elongated and flattened in the streamwise direction, with centers spaced spanwise approximately $y_3^+ = 80$ and perpendicular tothe wall $y_2^+ = 50$ [19]. Naraynan has found the width of the fine scale region to be a function of Re_λ , either sheetlike vorticity regions with thickness η , or filament-like with diameter η and spacing λ [53].

These large eddies can be considered the debris of initially unstable flow [55]. They are known to play an important role in shear layer growth, turbulent mixing, noise production, and turbulent transport of momentum, heat or mass [61]. Wygnanski and Champagne demonstrated that they possessed an ordered structure in pipe flow and grew very slowly if at all [64]. Hinze stated that the diffusive action of turbulence was mainly determined by the larger eddies [19]. Near the wall, Lee [65] found the large eddies to be greatly elongated, with lateral dimensions on the order of $\lambda^+/2$, whereas those in the core have been found by Hinze [19] to be elongated with diameters up to half the pipe radius.

Smaller eddies decay faster than large ones. They have a larger velocity gradient and a larger viscous shear stress counteracting the eddying motion [19]. In flow of this strong viscous nature, molecular effects dominate. Ueda demonstrated that both the fine and large scale structures in the laminar sublayer are influenced by the inrush phase of high axial momentum fluid into the low momemtum fluid [66].

Lindgren found that fine turbulence generated at the entry decayed with flow downstream, until a point was reached where a coarser equilibrium structure existed [67]. Mulhearn observed that the initial structure developed by the generating device, such as a grid, was strongly anisotropic. However, downstream the structure became remarkably similar, differing only in the length scales, dependent on the particular shear generating device [68]. Thus the details of the initial conditions, i.e. tripping wire, grid, or surface roughness become of minor importance, except in scale determination.

Even vortices of comparable size cannot coexist for long. As they are convected downstream, they must either disappear or amalgamate [63]. Annihilation of neighboring vortices occurs as they tend to rotate about one another. Roberts and Christian found this to occur when the distance between centers reached a value less than 1.7 times the diameter [69]. More found the value to be 2.8, at which distance mutual distortion caused the weaker neighbor to disintegrate [63]. Its vorticity ingested by its neighbors caused vortices to grow linearly in spacing and scale with downstream distance. This ingestion of irrotational fluid would require turbulent mixing and diffusion, and result in a statistically smooth linearly growing mixing layer [55].

Hinze has found that the irregularity and randomness of real turbulent motion are the main, if not sole, determinants of the transport and diffusion of turbulence [19].

Davies has emphasized the intermittency produced by large structures [61], while Ueda emphasized that the intermittency of the fine scale structure increased with Re_λ [66].

This intermittency is,however, largely absent in fully developed pipe flow, making the burst period nearly constant. The repetitive ordered structures do strongly interact with each other, coalescing as they move with the flow. These interactions strongly influence, if not control, many of the observable effects of turbulence, such as enhanced transport process.

Hinze [19] has shown that turbulence in the high wave-number range, i. e. smaller eddies, can only be determined by internal parameters, namely:

(1) Viscosity ν which determines the rate of dissipation.

(2) Energy flux ϵ , which equals the rate of energy dissipation per unit mass.

Thus, whereas turbulence in the core is affected by ν and the curvature of the velocity profile at that point, the basic parameters in the wall region are ν and u_f.

Studies of dissolution patterns on a soluble surface, like plaster-of-Paris, give additional clues to the effect of hydrodynamics on corrosion [70]. Just as with sand ripples on the ocean floor, as water flows over the surface, periodic troughs or flutes develop. Any mass transfer boundary layer that may exist over the sample surface is insufficient in

itself to initiate such a periodic pattern. The flow itself, as detailed in Figure 34, acts to initiate and propogate the contours. Once the surface irregularity is established, the peaks act as sites for flow separation, where mass transfer rates are low. Flow reattaches downstream where mass transfer rates are high. Coupled with the recirculation region between, troughs are formed and subsequently spread downstream. For Reynolds numbers much greater than that needed for flute stability, pot-holes developed in the slopes of profiles, where flow is reattaching. The characteristic dimensions of the resultant dissolution patterns were found to depend on the shear stress, fluid viscosity and velocity, and diffusivity. The analysis is complicated by the fact that the dissolution - rate velocity perpendicular to the wall is an unknown function of general turbulent flow.

Experiments by Rudd with drag reducing polymers further point out the effect of fluid variables on flow properties like shear stress. Adding the polymer causes earlier transition to turbulence, thickens and stabilizes the viscous sublayer (at the same value of Reynolds number), but has little effect on turbulence intensity. Spanwise velocity fluctuations are supressed, accompanied by increased eddy size at the wall. Only 10 to 100 ppm can decrease the friction factor by 80 per cent [71].

Pipe flow would certainly seem to be different from that along a flat plate. Indeed, the pressure gradient

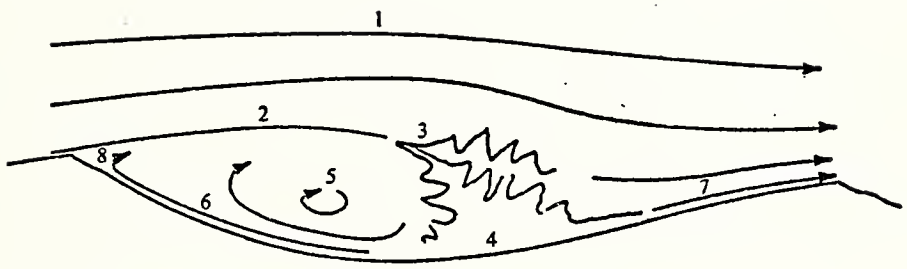

Figure 34. Hydrodynamic regions for flow over one flute. (1) Main turbulent flow. (2) Laminar free shear layer. (3) Transition to turbulence and entrainment. (4) Reattachment. (5) Irregular recirculating flow. (6) Lee-slope boundary layer. (7) Streamward-slope boundary layer. (8) Lee-slope boundary-layer separation with small eddies. From Blumberg [70].

within the pipe would cause the flow to differ significantly. Unlike in external flow, the pressure gradient term in the Navier-Stokes equation is non-zero. This prevents direct comparison of the two flow situations.

In a non-circular duct, secondary motion from the center towards the corners of only 1 per cent the axial velocity can become significant. The velocity profile is bulged outward near the corners, as Figure 35 shows. Melling showed that these secondary vortices were generated by gradients of Reynolds stresses across the duct cross section [72]. Landolt investigated the significance of these secondary motions on high rate metal dissolution during electrochemical machining. His results using a rectangular duct were consistent with those in a circular duct, despite the fact that the current distribution in the former was inhomogeneous [74]. This lends support to the use of a non-circular duct for corrosion studies, particularly useful when microscopic examination of the metal surface is desired. However, if these secondary motions have a negligible effect on dissolution rate, this would seem to imply that small variations in turbulent structure would be similarly unimportant.

Velocity and/or turbulence affects the anodic behavior of a metal in two ways:

(1) Removal of corrosion products.

(2) Changes in concentration of chemical species at the metal surface.

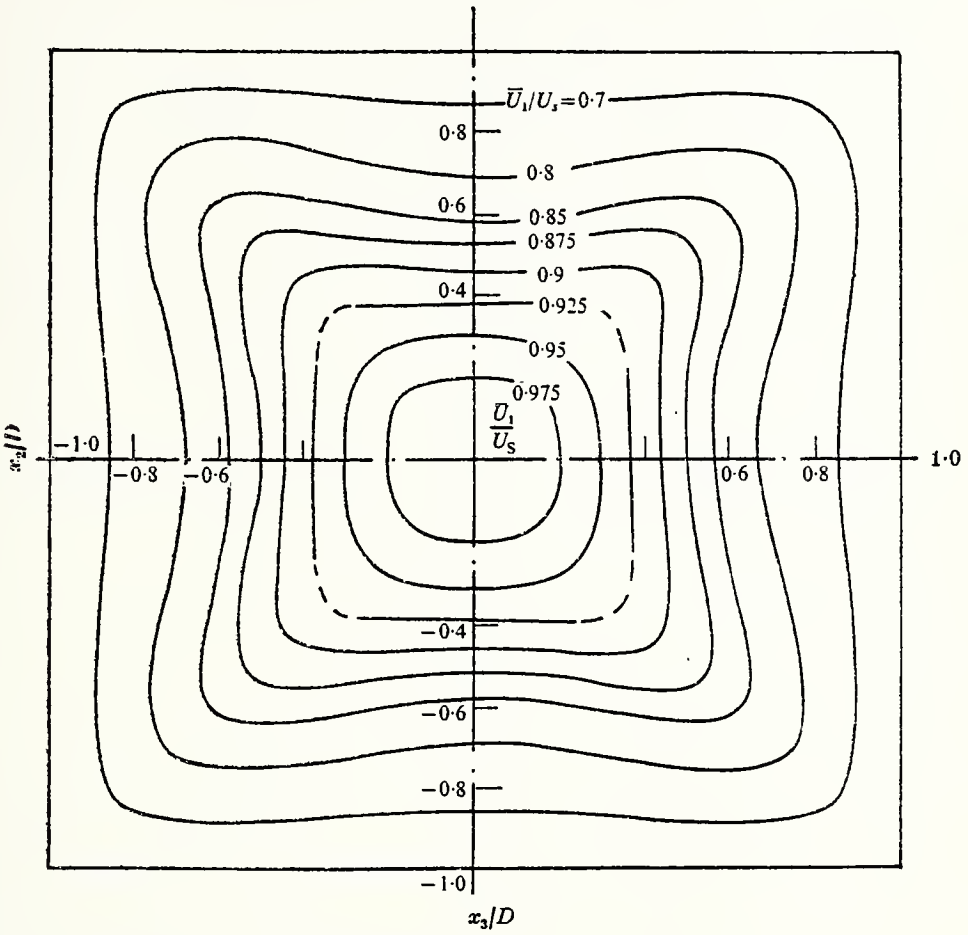

Figure 35. Distortion of mean velocity contours in a non-circular duct. From Fraunhofer and Pickup [73].

The manner in which oxygen is brought to the surface, i.e. to the local cathodes, must be considered. It seems obvious intuitively that turbulence parameters either affect the corrosion rate in themselves or affect other variables that do. That the corrosion rate varies between the laminar and turbulent flow regimes in circular ducts has been pointed out by Ross [40]. He found that when the log of corrosion rate was plotted against the log of Re_d (Reynolds number based on diameter) two linear portions stood out. Where Re_d was less than 2000, the corrosion rate was proportional to $(Re_d)^{\frac{1}{2}}$, while for higher values it was simply proportional to Re_d. This shows that a velocity change in the laminar regime will give a smaller change in corrosion rate than an equal velocity change in the turbulent regime. However, this analysis does not delineate whether the increased corrosion rate is due to the increased velocity (inherent in Re_d when the same test apparatus is used), or to some tangible or intangible in the turbulence itself.

To accent the importance of turbulence per se would require experiments on separate test setups where the velocity could be the same, but Reynolds numbers vary. Varying distances from the leading edge of a flat plate would seem appropriate, or varying the cross section in a flow channel. Cornet similarly found the increase in corrosion rate to be more rapid with increasing Reynolds number in the turbulent regime, so long as the rate was controlled by the transport of oxygen to the surface, i.e. diffusion controlled [11].

F. HYDRODYNAMIC CHARACTERIZATION

In the present work, the goal was to compare various turbulence structures or patterns and connect them to corrosion phenomena. Two aspects of the required characterization are the size differences and the violence of the motion. The former involved a time scale and a space scale. The latter is the turbulence intensity, $u_1' = (u_1^2)^{\frac{1}{2}}$ for the axial component, and corresponding quantities for the lateral components.

In real turbulence, both u_1 and the velocity gradient du_1/dt are statistical quantities, so rms values may be used as averages. As the wall is approached, the axial velocity u_1 decreases while its fluctuation u_1' remains nearly constant. This results in an increase in the turbulence intensity u_1'/u_1, as shown in Figure 36. Yet closer to the wall, u_1 continues to decrease, with u_1' now also decreasing due to viscous damping. So the turbulence intensity decreases. A peak then results at some characteristic distance from the wall. This peak region is usually associated with the maximum production and dissipation of turbulent energy. Curves found by various investigators are shown in Figure 36. The peaks are seen to range from approximately $y^+ = 12$ to 17, with maximum values of u^+ ranging from 2.6 to 3.0. This is surprisingly constant over quite a range of Reynolds numbers from 5600 to 35,500. The results of several investigators on the limiting value of turbulence intensity at $y+ = 0$ range

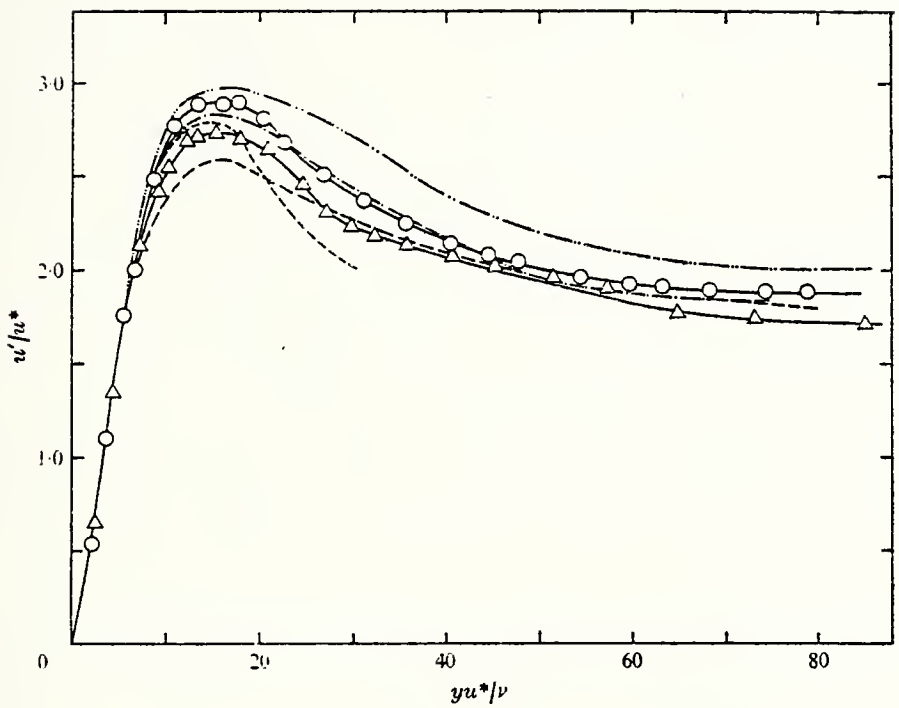

Figure 36. Distributions of turbulence intensity found by various researchers. From Ueda [66].

from 0.24 (Eckelmann) to 0.4 (Hinze), with Laufer obtaining 0.3 and Mitchell and Hanratty 0.32. While the use of anemometer probes is based on a basic law of steady state heat transfer, it must be noted that real turbulence is anything but steady. Perry has reported that differences of 25 per cent in rms turbulence levels is not uncommon in the literature [75].

The radial component of the fluctuating velocity gradient cannot be ignored, certainly when considering mass transport to the wall. Indeed, the fluctuations in the direction of mean flow have little effect on mass transfer. Sirkar and Hanratty showed that these strong transverse velocities extend right up to the wall and primarily govern the fluctuating concentration field [76]. Hinze has found that these perturbations in velocity that propogate towards the wall do so at the friction velocity u_f. With the sensing wire perpendicular to the flow, both the axial velocity component u_1 and that perpendicular to the wall u_2 are being measured.

Although the turbulence intensity is defined as $u'/\bar{u}$, the rms voltmeter reading (e') from the hot film probe does not give u' directly. It can be calculated if a particular empirical relationship is assumed between heat transfer and velocity. Using the relationship:

$$Nu = 0.4Pr^{1/5} + 0.6Pr^{1/3}Re_d^{1/2}$$

gives:

$$\frac{u_1'}{\bar{u}} = \frac{4\ e\ e'}{e^2 - e_o^2}$$

where e_o^2 is the point at which the curve of $u_1^{1/2}$ (determined from the rotometer) versus e^2 (the voltmeter readout) crosses the e^2 axis.

A typical curve is shown in Figure 37. Readings were taken both as the velocity was increased and again while it was decreased. Separate runs were made at five distances from the wall. The resultant values of e_o^2 were all obtained as shown in Figure 37. It should be noted that the open channel gave values less than the channel with a mesh at the entrance for the two positions closest to the wall (0.23 and 0.54 mm), equal values at 1.09 mm and greater for the two positions farthest from the wall (3.0 and 1.8 mm). In general, the turbulence intensity values decreased with increased velocity. At a particular velocity, the intensity increased as the wall was approached, as shown in Table 6 for 6 m/sec (19.7 ft/sec). The values did not peak as expected even though the wall was approached to within 0.23 mm. This was believed due to the disturbance caused by what (at that small a standoff from the wall) was a relatively large obstacle: the probe.

Another quantity in the turbulent flow that can be derived from the hot film anemometer output is the so-called

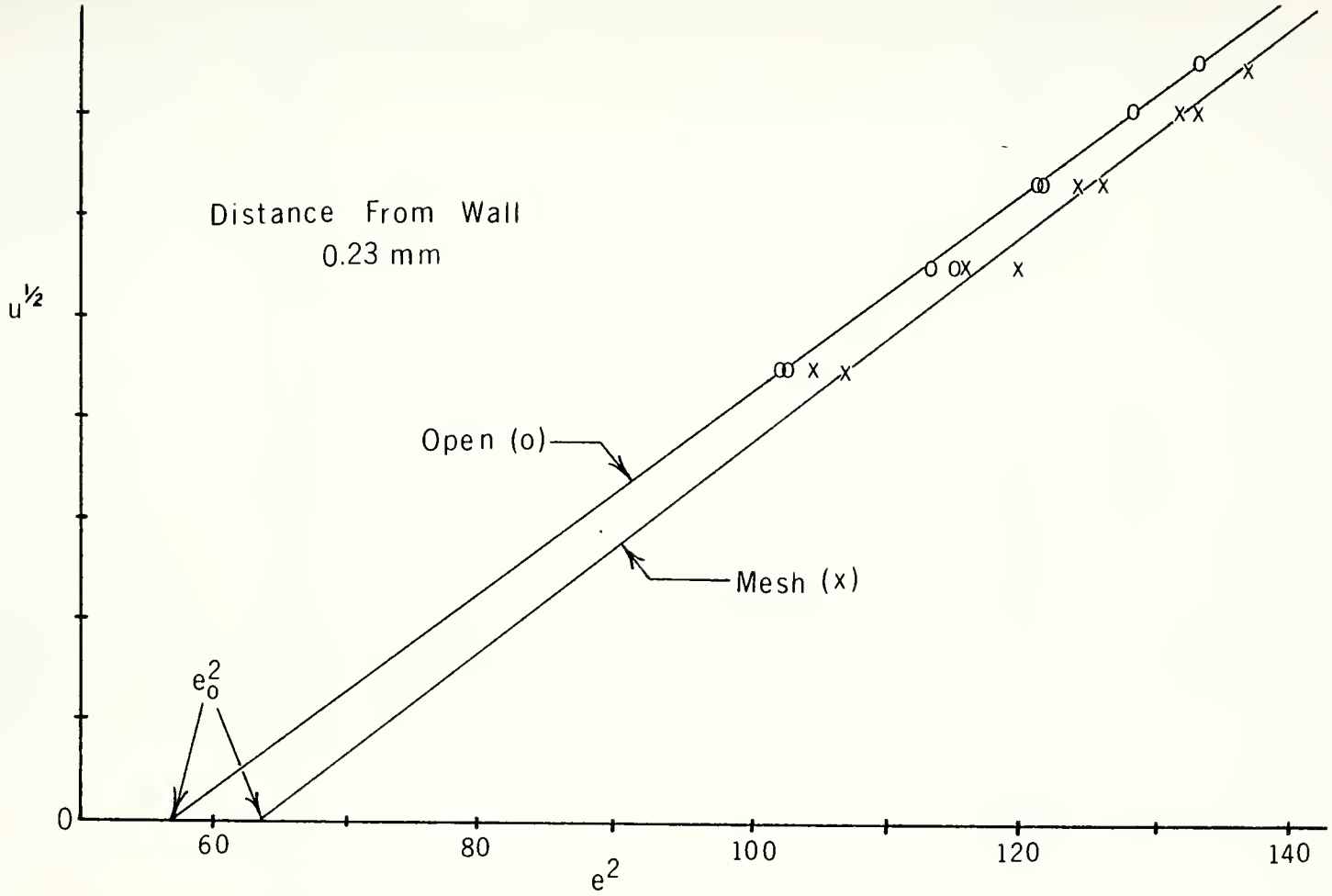

Figure 37. Determination of e_o^2 for use in calculating turbulence intensity.

TABLE 6

Distance from Wall (mm)	Turbulence Intensity Open Channel		Inlet Mesh	
3.0	.030	.033	.030	.038
1.8	.037	.038	.039	.040
1.1	.047	.047	.047	.048
0.54	.047	.045	.051	.052
0.23	.050	.048	.054	.051

Values of turbulence intensity at an average flow velocity of 6 m/sec in an open flow channel and with an inlet mesh.

microscale of turbulence (λ) which is related to the size of the smallest eddies in the turbulent field, those eddies that become dissipated due to viscosity effects. The signal is processed through a differentiator with a time constant τ and read out on an rms voltmeter. This value (r) in units of velocity is then used in the expression:

$$\lambda = \frac{\bar{u}_1 \tau u_1'}{r} = \frac{\bar{u}_1^2 \tau}{r} \frac{u_1'}{\bar{u}_1}$$

As with the turbulence intensity, the mesh did have an effect on r. Except for the position closest to the wall, the mesh readings were consistently higher than those taken in the open channel. This would decrease the value of λ , exactly the effect expected. The character of any fluid dynamic process like turbulence is directly determined by the ratio between inertial and viscous forces. Therefore, a Reynolds number of turbulence can be formed using this microscale as the characteristic length and $\bar{u}$ or u' as the velocity term.

G. MASS TRANSFER

Heat and mass transfer are analagous processes. In any boundary layer dominated process, it has been experimentally determined that $Nu \propto Sc^{1/3}$. The Sherwood number (Sh) is the mass transfer equivalent of the Nusselt number. Plotting $Sh/Sc^{1/3}$ versus Re_d gave Tvarusko approximately

linear results with horizontal cylinders over a wide range of Re_d up to 4×10^5 [77]. He found an increase in the ratio of only 15 per cent as a result of increasing the turbulence intensity from 0.15 to 1.0, and this much change occurring only at the highest Reynolds numbers. Sirkar has shown that at high Schmidt numbers, the mass transfer is actually controlled by this fluctuating velocity field [76]. The exponent of the Schmidt number may vary, depending on the relative importance given to the transfer of mass by momentum or diffusion. Leumer has summarized the dimensionless mass transfer correlations most prevelant in the literature [43]. The thickness of the mass transfer boundary layer (δ_m) stabilizes very rapidly with distance along a wall. In the present flow channel, for velocities of 4 to 8 m/sec, it is on the order of 20μm thick, based on the relationship given by Wranglen [78].

The variation in boundary layer thickness does correlate well with certain parameters that have a known effect upon corrosion. A thinner boundary layer has a steeper concentration gradient. However, to assume that this always results in increased corrosion would be mistaken. Its thickness can be altered in two different ways:

(1) Increasing the velocity, i.e. Reynolds number, decreases δ_m and does increase the corrosion rate.

(2) Increasing the diffusion coefficient D_{O_2} (by an increase in temperature for example, which also decreases ν)

decreases the Schmidt number (ν/D_{O_2}) and therefore increases the boundary layer thickness. But since $\delta_m \propto Sc^{-1/3}$, D_{O_2} increases at a faster rate than δ_m. The mass flux is proportional to D_{O_2} / δ_m, so the net effect is an increase in corrosion rate.

Recapitulating, in (1) above, a decrease in δ_m leads to an increase in corrosion rate, while in (2) an increase in δ_m leads to an increase in corrosion rate.

V. SUMMARY

As a result of this research, the following conclusions concerning 90/10 Cu-Ni have been reached:

(1) A flow channel, as opposed to other test setups, has the important advantages of allowing the specimens to be easily instrumented for electrochemical monitoring, ensuring fully developed turbulent flow across the specimen, and permitting continuous viewing of the specimen surface.

(2) When crevices or steps perpendicular to the flow are avoided, test runs for 48 hours show no preferential dissolution at the leading edge that might be due to the establishment of the mass transfer boundary layer.

(3) There is a strong dependence of the corrosion rate of 90/10 Cu-Ni on temperature, attributed mainly to increased reaction kinetics and the increase in the diffusion coefficient of oxygen.

(4) The corrosion rate of 90/10 Cu-Ni increases non-linearly with velocity, ranging from 6.5 mpy at 4 m/sec to 13 mpy at 7.8 m/sec. (All the corrosion rates are expected to be on the high side, due to averaging over the relatively short duration of 48 hours, when the corrosion rate is expected to be higher than steady state.)

(5) The turbulence intensity was investigated using hot film anemometry. It increased as the wall was approached down to a minimum distance of 0.23 mm. At that minimum distance tested, the values ranged from .046 to .085, roughly

doubling as the flow velocity was decreased from 7 m/sec to 2.5 m/sec. Introducing a mesh at the channel entrance (51 hydraulic diameters away from the specimen) increased the turbulence intensity roughly 2 per cent, but at the only velocity tested (4 m/sec) had no effect on corrosion rate.

(6) Empirical scaling factors are necessary to relate the variable effects of hydrodynamic parameters on corrosion for widely varying flow situations. These are difficult to develop experimentally, but careful modeling of the relationship in a small test facility can at least establish the trends in a service situation.

(7) Fluctuating local peaks in wall shear stress may be orders of magnitude greater than the average shear stress calculated from macroscopic hydrodynamic conditions. This fluctuating stress may affect corrosion in several ways, such as altering the form and distribution of anodic films, limiting the buildup of corrosion products and removing existing accumulations of corrosion products.

(8) The concentration of electrochemical products (metal ions) and reactants (oxygen) at the metal/electrolyte interface is controlled by molecular diffusive, natural convective and eddy diffusive (forced convective) modes of mass transport. The model for corrosion in a flow field must particularly include the effect of eddy diffusivity, which can often be the major component of mass transport. When considering

eddy diffusivity, the details of the flow structure, in terms of the eddy size distribution in the turbulent flow field, must be taken into account, as this is a real physical difference in various flow situations. The model by which this feature is accounted for might incorporate the effects of mixing in dimensionless groups like the Sherwood and Schmidt numbers, or might adapt experimentally measurable parameters that characterize the turbulence, such as turbulence intensity and microscale.

LIST OF REFERENCES

1. LaQue, Francis L., "Corrosion Testing," paper presented before the 54th annual meeting of ASTM, Philadelphia Proceedings, Vol. 51, 1951.

2. Lee, G. L., American Foundrymen's Society, Vol. 65, 1957, p. 570.

3. Niederberger, R. B., "Condensor Tube Materials for Sea Water Services," Copper Development Association extract 1546, November 1965.

4. Stewart, W. C. and LaQue, F. L., "Corrosion Resisting Characteristics of Iron Modified 90:10 Cupro Nickel Alloy," Corrosion, Vol. 8, 1952, p. 259.

5. Danek, G. J., Jr., "The Effect of Sea-Water Velocity on the Corrosion Behavior of Metals," Naval Engineers Journal, October 1966, p. 763-769.

6. Anderson, D. B. and Efird, K. D., "Cu-Ni Resists Recirculated Sea Water," Power, February 1974.

7. Ferrara, Robert J. and Gudas, John P., "Corrosion Behavior of Copper-Base Alloys with Respect to Sea-water Velocity," Proceedings of the Third Int'l Congress on Marine Corrosion and Fouling, October 1972, p. 285-298.

8. "Cathodic Protection of Surface Effect Ships at High Speeds," Final Report by Bell Aerosystems Co. and Ocean City Research Corp., September 1972.

9. Porte, Howard A., "The Effect of Environment on the Corrosion of Metals in Sea Water - A Literature Survey," NCEL Technical Note N-907, July 1967.

10. Syrett, Barry C., "Erosion-Corrosion of Copper-Nickel Alloys in Sea Water and Other Aqueous Environments - A Literature Review," Corrosion, Vol. 32, No. 6, June 1976, p. 242-252.

11. Cornet, I., Barrington, E. A., and Behrsing, G. U., "Effects of Reynolds Number on Corrosion of Copper by Sulfuric Acid," Journal of the Electrochemical Society, October 1961, p. 947-953.

12. Prandtl, L. and Tietdjens, O. G., Applied Hydro - and Aeromechanics, McGraw Hill Book Company, Inc., N.Y., 1934.

13. Ross, Ralph W., Jr., and Anderson, David B., "Hot Sea Water Corrosion of Copper-Base Alloys," Materials Performance, September 1975, p. 27-32.

14. Cornet, I., "Velocity Effects in Corrosion," NACE Corrosion 77 Educational Lecture, March 1977, p. 1-3.

15. Efird, K. D. and Anderson, D. B., "Sea Water Corrosion of 90-10 and 70-30 Cu-Ni: 14 Year Exposures," Materials Performance, Vol. 14, No. 11, November 1975, p. 37-40.

16. Hack, H. P., Miller, B. E. and Davis, D. A., "Impressed Current Cathodic Protection for Surface Effect Ships," NSR&D Report 4200, July 1974.

17. Ross, T. K., Wood, G. C. and Mahmud, I., "The Anodic Behavior of Iron-Carbon Alloys in Moving Acid Media," Journal of the Electrochemical Society, Vol. 113, No. 4, p. 334-345.

18. Smith, Carroll A., "Velocity Effects on the Corrosion Rates of Metals in Natural Sea Water," Paper E presented at the SNAME Southeast Section Symposium on Undersea Technology in Panama City, Florida on May 10, 1968.

19. Hinze, J. O., Turbulence, 1975, McGraw Hill.

20. Kester, D. R., Duedall, I. W., Conners, D. N. and Pytokowicz, R. M., "Preparation of Artificial Seawaters," Limnology and Oceanography, Vol. 12, December 1967, p. 176-178.

21. Smethie, W. M., Jr., "Some Aspects of the Temperature, Oxygen and Nutrient Distributions in Monterey Bay, California," Moss Landing Marine Laboratories Technical Publication 73-1, 1973.

22. Traganza, Eugene D., Clayton, John R., Jr., Payne, James R. and Risebrough, Robert W., "Chemical Oceanography of the Coastal Zone of Central and Northern California," Report to Bureau of Land Management by Winzler and Kelly Consulting Engineers, Contract #AA550-CT6-5E, August 1977, Vol. 1.

23. Broenkow, William W. and Benz, Sandra R., "Oceanographic Observations in Monterey Bay, California - January 1972 to April 1973," Moss Landing Marine Laboratories Technical Publication 73-3, 1973.

24. Cox, R. A., Culkin, F., and Riley, J. P., "The Electrical Conductivity/Chlorinity Relationship in Natural Sea Water," Deep Sea Research, Vol. 14, 1967, p. 203-220.

25. "Saline Water Conversion Programs - Gives Harbor Is. Salt Water Conditions," Bulletin of the Sea Horse Institute, Vol. 4, No. 1, May 1963, p. 3-4.

26. Characklis, W. G., "Attached Microbial Growth - I. Attachment and Growth," Water Research, Vol. 7, 1973, p. 1113-1127.

27. Iverson, Warren P. and Calvert, Joan, "Microbial Corrosion," Nat'l Bureau of Standards Report, Summary for May 1, 1968 to April 30, 1969, Contract NAONR 14-67.

28. Bott, T. R. and Pinheiro, M.M.P.S., "Biological Fouling - Velocity and Temperature Effects," Paper No. 76-CSME/CSChE-25 presented at the 16th National Heat Transfer Conference, St. Louis, August 8-11, 1976.

29. Ritter, R. B. and Suitor, J. W., "Fouling Research on Copper and Its Alloys - Seawater Studies," Progress Report of Heat Transfer Research Ince., April 1976 for period January 1974 - February 1976.

30. Scott, D. A., AMBAG Oceanographic Survey, Oceanographic Services Inc., OSI #168-2, Santa Barbara, California, 1973.

31. Horne, R. A., Marine Chemistry, Wiley, 1969.

32. Truesdale, G. A., Downing, A. L. and Lowden, G. F., "The Solubility of Oxygen in Pure Water and Sea - Water," Journal of Applied Chemistry, Vol. 5, February 1955, p. 53-62.

33. Reinhart, Fred M. and Jenkins, James F., "The Relationship Between the Concentration of Oxygen in Seawater and the Corrosion of Metals," Proceedings of the 3rd Int'l Congress on Marine Corrosion and Fouling, October 1972, p. 562-577.

34. Macdonald, D.D., Syrett, B. C. and Wing, S. S., "A Study to Determine the Mechanisms of Corrosion of Copper-Nickel Alloys in Sulfide-Polluted Seawater," Annual Report of 1 February 1978 to ONR on Contract #N00014-77-C-0046.

35. Macdonald, D.D., Syrett, B. C., "Methods for Measuring Corrosion Rates of Copper-Nickel Alloys in Flowing Sea Water," Preprint of paper to be presented at Corrosion 78 Conference, Houston, March 6-10, 1978.

36. Peterson, M. H. and Gehring, G. A., Jr., "Corrosion Behavior of AISI C-1018 Low Carbon Steel in High Velocity Sea Water," Paper presented at Corrosion 78 Conference, Houston, March 6-10, 1978.

37. "Preparing, Cleaning, and Evaluating Corrosion Test Specimens," 1976 ASTM Annual Book of Standards, Part 10, ASTM Standard GI-72.

38. Stern, M. and Geary, A. L., Journal of the Electrochemical Society, Vol. 104, 1957, p. 56.

39. Walter, G. W., "Problems Arising in Determination of Corrosion late from Linear Polarization Measurements," Corrosion Science, Vol. 17, 1977, p. 983.

40. Ross, T. K. and Jones, D. H., "Corrosion Inhibition in Moving Media," Journal of Applied Chemistry, Vol. 12, July 1962, p. 314-319.

41. Locke, J., Effect of Galvanic Coupling, Potential, and Temper Condition on the Mode and Distribution of Corrosion Attack of an Aluminum Alloy in Seawater, MSME Mechanical Engineer Thesis, Naval Postgraduate School, Sept. 1978.

42. "Review of High Velocity Sea Water Corrosion T-7C-5 Task Group Report," Paper #101 presented at NACE International Corrosion Forum, March 1977, p. 1-16.

43. Leumer, G., Effect of Hydrodynamic Variables on Corrosion: Study of 90/10 Cu-Ni in a Circling Foil with Synthetic Seawater, MSME Mechanical Engineer Thesis, Naval Postgraduate School, March 1978.

44. "Standard Reference Method for Making Potentiostatic and Potentiodynamic Anodic Polarization Measurements," 1976 ASTM Annual Book of Standards, Part 10 ASTM Standard G5-72.

45. Tait, W. S., "Effect of Physical Parameters on the Pitting Corrosion of Mild Steel in Low Total Dissolved Solids, Oxygen Bearing Water," Paper presented at Corrosion 78 Conference, Houston, March 6-10, 1978.

46. Popplewell, J. M., "Marine Corrosion of Copper Alloys: An Overview," Paper presented at Corrosion 78 Conference, Houston, March 6-10, 1978.

47. Streeter, Victor L. and Wylie, E. Benjamin, Fluid Mechanics, McGraw-Hill, Inc., 1966.

48. Eckelmann, Helmut, "The Structure of the Viscous Sublayer and the Adjacent Wall Region in a Turbulent Channel Flow," Journal of Fluid Mechanics, Vol. 65, Part 3, 1974, p. 439-459.

49. Wallace, James M., Eckelmann, Helmut and Broodkey, Robert S., "The Wall Region in Turbulent Shear Flow," Journal of Fluid Mechanics, Vol. 54, Part 1, 1972, p. 39-48.

50. Heidrick, T. R., Banerjee, S. and Azad, R. S., "Experiments on the Structure of Turbulence in Fully Developed Pipe Flow: Interpretation of the Measurement by a Wave Model," Journal of Fluid Mechanics, Vol. 81, Part 1, 1977, p. 137-154.

51. Kim, H. T., Kline, S. J. and Reynolds, W. C., "The Production of Turbulence Near a Smooth Wall in a Turbulent Boundary Layer," Journal of Fluid Mechanics, Vol. 50, Part 1, 1971, p. 133-160.

52. Offen, G. R. and Kline, S. J., "A Proposed Model of the Bursting Process in Turbulent Boundary Layers," Journal of Fluid Mechanics, Vol. 70, Part 2, 1975, p. 209-228.

53. Naraynanam, M.A. Badri, Rajagopalan, S. and Narasimha, R., "Experiments on the Fine Sturcture of Turbulence," Journal of Fluid Mechanics, Vol. 80, Part 2, 1977, p. 237-257.

54. Michalke, A., "The Instability of Free Shear Layers: A Survey of the State of the Art," DLR Mitt., No. 70-74, 1970.

55. Acton, E., "The Modeling of Large Eddies in a Two-Dimensional Shear Layer," Journal of Fluid Mechanics, Vol. 76, Part 2, 1976, p. 561-592.

56. Bark, Fritz H., "On the Wave Structure of the Wall Region of a Turbulent Boundary Layer," Journal of Fluid Mechanics, Vol. 70, Part 2, 1975, p. 229-250.

57. Landahl, M. T., Journal of Applied Mathematics, 1975.

58. Bremhorst, K. and Walker, T. B., "Spectral Measurements of Turbulent Momentum Transfer in Fully Developed Pipe Flow," Journal of Fluid Mechanics, Vol. 6, Part 1, 1973, p. 173-186.

59. Sabot, Jean and Comte-Bellot, Genevieve, "Intermittency of Coherent Structures in the Core Region of Fully Developed Pipe Flow," Journal of Fluid Mechanics, Vol. 74, Part 4, 1976, p. 767-796.

60. Corino, E. R. and Broodkey, R. S., Journal of Fluid Mechanics, Vol. 37, 1969, p.1.

61. Davies, P.O.A.L. and Yule, A. J., "Coherent Structures in Turbulence," Journal of Fluid Mechanics, Vol. 69, Part 3, 1975, p. 513-537.

62. Fortuna, Gilead and Hanratty, Thomas J., "The Influence of Drag-Reducing Polymers on Turbulence in the Viscous Sublayer," Journal of Fluid Mechanics, Vol. 53, Part 3, 1972, p. 575-586.

63. Moore, D. W. and Saffman, P. G., "The Density of Organized Vortices in a Turbulent Mixing Layer," Journal of Fluid Mechanics, Vol. 69, Part 3, 1975, p. 465-473.

64. Wygnanski, I. J. and Champagne, F. H., "On Transition in a Pipe, Part 1. The Origin of Puffs and Slugs and the Flow in a Turbulent Slug," Journal of Fluid Mechanics, Vol. 59, 1973, p. 281-335.

65. Lee, Myron, K. I., Eckelman, Larry D. and Hanratty, Thomas J., "Identification of Turbulent Wall Eddies Through the Phase Relation of the Components of the Fluctuating Velocity Gradient," Journal of Fluid Mechanics, Vol. 66, Part 1, 1974, p. 17-33.

66. Ueda, H. and Hinze, J. O., "Fine-Structure Turbulence in the Wall Region of a Turbulent Boundary Layer," Journal of Fluid Mechanics, Vol. 67, Part 1, 1975, p. 125-143.

67. Lindgren, E. R., Archiv for Fysik, Vol. 24, 1963, p. 269.

68. Mulhearn, P. J. and Luxton, R. E., "The Development of Turbulence Structure in a Uniform Shear Flow," Journal of Fluid Mechanics, Vol. 68, Part 3, 1975, p. 577-590.

69. Roberts, K. V. and Christiansen, J. P., "Topics in Computational Fluid Mechanics," Comp. Phys. Comm. (Supplement), Vol. 3, 1972, p. 14.

70. Blumberg, Paul N. and Curl, Rane L., "Experimental and Theoretical Studies of Dissolution Roughness," Journal of Fluid Mechanics, Vol. 65, Part 4, 1974, p. 735-751

71. Rudd, M. J., "Velocity Measurements Made with a Laser Dopplermeter on the Turbulent Pipe Flow of a Dilute Polymer Solution," Journal of Fluid Mechanics, Vol. 51, Part 4, 1972, p. 673-685.

72. Melling, A. and Whitelaw, J. H., "Turbulent Flow in a Rectangular Duct," Journal of Fluid Mechanics, Vol. 78, Part 2, 1976, p. 289-315.

73. Fraunhofer, J. A. von & Pickup, G. A., "The Examination of Corrosion Products and Processes, Part 2 - A Plain Man's Guide to Potentiostats," Anti-Corrosion Methods and Materials, Vol. 14, No. 5, May 1967, p. 17-21.

74. Landolt, D., Muller, R. H., & Tobias, C. W., "Anode Potentials in High-Rate Dissolution of Copper," Journal of the Electrochemical Society, Vol. 118, No. 1, January 1971, p. 40-46.

75. Perry, A. E. and Abell, C. J., "Scaling Laws for Pipe-Flow Turbulence," Journal of Fluid Mechanics, Vol. 67, Part 2, 1975, p. 257-271.

76. Sirkar, Kamalesh K. and Hanratty, Thomas J., "The Limiting Behavior of the Tubulent Transverse Velocity Component Close to a Wall," Journal of Fluid Mechanics, Vol. 44, Part 3, 1970, p. 605-614.

77. Tyarusko, Aladar, "Mass Transfer on Horizontal Wires in the Presence of Free and Combined Forced and Free Convection," Journal of the Electrochemical Society, April 1976, p. 489-494.

78. Wranglen, G. and Nilsson, O., "Mass Transfer Under Forced Laminar and Turbulent Convection at Horizontal Plane Plate Electrodes," Electrochemical Acta, Vol. 7, 1962, p. 121-137.

INITIAL DISTRIBUTION LIST

		No. Copies
1.	Defense Documentation Center Cameron Station Alexandria, Virginia 22314	2
2.	Library, Code 0142 Naval Postgraduate School Monterey, California 93940	2
3.	Department Chairman, Code 69 Department of Mechanical Engineering Naval Postgraduate School Monterey, California 93940	2
4.	Professor A. J. Perkins, Code 69Ps Department of Mechanical Engineering Naval Postgraduate School Monterey, California 93940	6
5.	Professor T. Houlihan, Code 69Hm Department of Mechanical Engineering Naval Postgraduate School Monterey, California 93940	1
6.	LT Robert P. Schack, USN Supervisor of Shipbuilding, Conversion and Repair Groton, Connecticut 06340	3

Thesis
S2448
c.1

Schack
Effects of hydrodynamic variables on corrosion.

175359